

# **DETECTING NANO- AND MICRO-SIZED PROTEIN CRYSTALS VIA NONLINEAR OPTICAL IMAGING METHODS**

## **DISSERTATION**

zur Erlangung des Doktorgrades der Naturwissenschaften (*Dr. rer. nat.*)  
an der Fakultät für Mathematik, Informatik und Naturwissenschaften  
der Universität Hamburg, Fachbereich Chemie

vorgelegt von  
**Qingdi Cheng**

Hamburg, 2021



Die vorliegende Arbeit wurde im Zeitraum von Dezember 2016 bis März 2020 in der Arbeitsgruppe von Prof. Dr. C. Betzel im Laboratorium für Strukturbiologie von Infektion und Entzündung am Institut für Biochemie und Molekularbiologie des Fachbereichs Chemie der Universität Hamburg durchgeführt.

1. Gutachter: Prof. Christian Betzel
2. Gutachter: Prof. Franz X. Kärtner

Datum der Disputation: 21.05.2021



## Publications

**Qing-di Cheng**<sup>‡</sup>, Hsiang-Yu Chung<sup>‡</sup>, Robin Schubert, Shih-Hsuan Chia, Sven Falke, Célestin Nzanzu Mudogo, Franz X. Kärtner\*, Guoqing Chang\*, and Christian Betzel\*. Protein-crystal detection with a compact multimodal multiphoton microscope. *Communications Biology*, **3**, 569 (2020). (‡ These authors contributed equally to this work).

Mengying Wang, Sven Falke, Robin Schubert, Kristina Lorenzen, **Qing-di Cheng**, Christian Exner, Hévila Brognaro, Celestin Nzanzu Mudogo, Christian Betzel\*. Pulsed electric fields induce modulation of protein liquid-liquid phase separation. *Soft Matter*, **16**, 8547-8553 (2020).

Sven Falke, Hévila Brognaro, Célestin Nzanzu Mudogo, Mengying Wang, **Qing-di Cheng**, Christian Betzel\*. Dynamic formation and internal order of liquid dense protein clusters beyond crystallography. *Acta Crystallographica Section A: Foundations and Advances*, **75**, e68 (2019).

Hsiang-Yu Chung\*, **Qing-di Cheng**, Robin Schubert, Markus Perbandt, Christian Betzel, Rüdiger Greinert, Franz X. Kärtner, and Guoqing Chang. Multimodal multiphoton microscopy driven by a fiber-based two-color ultrafast source. *Conference: Bio-Optics: Design and Application*, paper DT1B.2 (2019).



# Table of contents

Publications .....	i
List of abbreviations .....	vii
Zusammenfassung.....	1
Abstract.....	5
1 Introduction .....	9
1.1 Three-dimensional (3D) structure determination of proteins.....	9
1.2 Early history of protein crystallography .....	9
1.3 Background (Development of solving protein structure) .....	12
1.3.1 Conventional protein single-crystal X-ray crystallography .....	13
1.3.2 New approach to solving protein structure from tiny crystal....	15
1.3.3 Time-resolved crystallography.....	19
1.4 Linear optical imaging methods for detecting and identifying protein crystal .....	20
1.4.1 Conventional optical microscopy .....	20
1.4.2 Transmission electron microscopy .....	22
1.4.3 Dynamic light scattering (DLS) and depolarized dynamic light scattering (DDLS).....	24
1.4.4 X-ray powder diffraction.....	26
1.5 Theory (Nonlinear optical imaging methods) .....	27
1.5.1 Multiphoton fluorescence imaging.....	27
1.5.2 High harmonic generation imaging.....	31
1.6 Second-order nonlinear imaging of chiral crystals (SONICC) for detecting small protein crystal .....	34

1.7 Objectives of this study .....	39
2 Materials and methods .....	41
2.1 Proteins, chemicals, and reagents .....	41
2.2 Instruments and consumables.....	43
2.3 Crystal preparation.....	45
2.3.1 <i>In vitro</i> protein crystal preparation.....	45
2.3.2 <i>In vivo</i> protein crystal preparation .....	47
2.3.3 Salt crystal preparation .....	48
2.4 DLS and DDLS measurements .....	48
2.5 TEM imaging .....	49
2.6 X-ray powder diffraction .....	49
2.7 Sample preparation in different sample containers .....	50
2.7.1 Conventional sample container .....	50
2.7.2 Polydimethylsiloxan (PDMS) microfluidic chip.....	51
2.7.3 The 96-well 2-drop MRC crystallization plate (MRC-2 plate) ..	56
2.8 THG/SHG imaging .....	57
2.9 Angular-dependent SHG polarization intensity.....	57
2.10 Imaging protein crystal applying the Formulatrix SONICC and the MPM imaging systems .....	58
2.11 Imaging of salt crystal applying the MPM imaging system .....	60
3. Design and construction of the MPM system.....	61
3.1 Design and construction .....	61
3.1.1 Nonlinear optical imaging methods selection .....	61
3.1.2 Selection of laser sources.....	65

3.1.3 Construction .....	67
3.2 Poor reproducibility of <i>in vitro</i> protein crystallization results.....	73
3.3 THG/SHG imaging .....	74
3.4 Angular-dependent SHG polarization intensity.....	78
3.5 SHG detection of salt crystals .....	81
3.6 Protein crystal detection with THG, SHG, and three-photon UV imaging.....	84
3.7 Summary and discussions.....	85
3.7.1 Poor reproducibility of <i>in vitro</i> protein crystallization.....	85
3.7.2 Sample container selection.....	87
3.7.3 Angular dependence of SHG intensity from the protein crystal .....	88
3.7.4 SHG signals from centrosymmetric crystals .....	89
4. <i>In vitro</i> and <i>in vivo</i> protein crystal detection .....	91
4.1 Complementary methods for detecting protein crystal .....	91
4.1.1 DLS and DDLS experiments .....	91
4.1.2 TEM imaging experiments.....	93
4.1.3 X-ray protein powder diffraction experiments .....	98
4.2 Imaging the <i>in vitro</i> protein crystals applying the Formulatrix SONICC and the MPM imaging systems .....	98
4.3 Imaging the <i>in vivo</i> protein crystals applying the MPM imaging system .....	102
4.4 Summary and discussions.....	107
4.4.1 Complementary methods.....	108
4.4.2 Imaging methods of the SONICC and MPM systems .....	109

4.4.3 Parameters of the SONICC and MPM systems.....	112
4.4.4 <i>In vitro</i> protein crystal and <i>in vivo</i> protein crystal detection...	116
5 Conclusion and outlook.....	119
6 References .....	123
Appendix.....	145
List of chemicals.....	145
GHS Hazard Statements .....	147
GHS Precautionary Statements .....	149
List of figures .....	151
List of tables .....	155
Acknowledgement.....	157
Eidesstattliche Versicherung: .....	159

## List of abbreviations

---

1PEF	One-photon excitation fluorescence
2PEF	Two-photon excitation fluorescence
3D	Three-dimensional
3PEF	Three-photon excitation fluorescence
BPF	Bandpass filter
CFEL	Center for Free-Electron Laser science
CO <sub>2</sub>	Carbon dioxide
CPA	Chirped-pulse amplification
Cryo-EM	Cryogenic electron microscopy
DESY	Deutsches Elektronen-Synchrotron
DDLS	Depolarized dynamic light scattering
DLS	Dynamic light scattering
DM	Dichroic mirror
DMEM	Dulbecco's modified eagle medium
DSF	Dispersion-shifted fiber
EDFL	Erbium-doped fibre laser
FBS	Fetal Bovine Serum
FEL	Free-electron laser
FFT	Fast Fourier transform
fs	Femtosecond
g	Gravitational constant
GFP	Green fluorescent protein
h	Hour
HEK 293	Human embryonic kidney 293

---

---

HG	Harmonic generation
HGM	Harmonic generation microscopy
HWP	Half-wave plate
IMPDH	Isoleucine-5'-monophosphate dehydrogenase
K	Kelvin
KDP	Potassium dihydrogen phosphate
l	Liter
LBO	Lithium Triborate
LCLS	Linac Coherent Light Source
LLPS	Liquid-liquid phase separation
m	Meter
M	Molar
MgO:PPLN	Magnesium-doped periodically poled lithium niobate
min	Minute
mm	Millimeter
MPEF	Multi-photon excitation fluorescence
MPM	Multi-photon microscopy
ms	Millisecond
NA	Numerical aperture
Nd	Neodymium-doped
nm	Nanometer
NMR	Nuclear magnetic resonance spectroscopy
ns	Nanosecond
O <sub>2</sub>	Oxygen gas

---

---

PAK4	P21 serine /threonine kinase 4
PAK4-GFP	PAK4 in complex with green fluorescent protein
PAK4-inka	PAK4 in complex with its inhibitor Inka1
PEG	Polyethylene glycol
PBS	Polarization beam splitter
PDB	Protein Data Bank
PDMS	Polydimethylsiloxane
PEI	Polyethyleneimine
PFA	Paraformaldehyde
Phe	Phenylalanine
PMT	Photomultiplier tube
rpm	Rounds per minute
s	Second
SESS	Self-phase modulation enabled spectral selection
<i>Sf9</i>	Spodoptera frugiperda 9 cells
SFX	Serial femtosecond X-ray crystallography
SHG	Second-harmonic generation
SONICC	Second order nonlinear optical imaging of chiral crystals
SSX	Serial synchrotron X-ray crystallography
SPM	Self-phase modulation
THG	Third-harmonic generation
Trp	Tryptophan
Tyr	Tyrosine
UV	Ultraviolet

---

---

UV-TPEF	Ultraviolet two-photon excited fluorescence
XFEL	X-ray free-electron laser
YAG	Yttrium aluminum garnet
Yb	Ytterbium
$\mu$	Micro
$\sigma$	Sigma

---

# Zusammenfassung

Biologische Makromoleküle wie Proteine und Nukleinsäuren bestehen aus verknüpften Monomeren und spielen eine wichtige Rolle in biologischen Funktionen, basierend auf ihrer dreidimensionalen Struktur. Proteine sind zusammengesetzt aus einer oder mehreren Polypeptidketten mit verschiedenen Aminosäureresten. Diese Polypeptidketten falten sich in eine 3D Struktur um ein funktionelles Protein zu erzeugen. Das Wissen über die 3D Struktur von Proteinen kann verwendet werden um ihre Protein-Ligand Prozesse und Interaktionen zu analysieren. Des Weiteren, kann das Wissen über die 3D Struktur von Proteinen als Basis von strukturbasierter Zielauswahl Arzneimittelforschung und -entwicklung dienen. Da es nicht möglich ist die 3D Struktur von Proteinen unter hochentwickelten Lichtmikroskopen zu sehen, werden andere Methoden verwendet um diese zu bestimmen. Röntgenkristallographie kann verwendet werden, um die 3D Struktur von Proteinen zu lösen, da diese Kristalle bilden können. Nahezu 90% der Proteinstrukturen, welche in der „Protein Data Bank“ hinterlegt sind, wurden durch Röntgenkristallographie gelöst. Resultierend, ist die Röntgenkristallographie die fundamentale Methode für die Charakterisierung der atomaren Struktur von Proteinen.

Bemerkenswerterweise ist die älteste Anwendung der Röntgenkristallographie die Einkristall-Röntgenbeugung. Die größte Herausforderung, zur Verwendung dieser Methode, ist das Erhalten eines gut geordneten Kristalls in einer passenden Größe zur Sammlung kristallographischer Daten. Der Anspruch nach größeren und gut geordneten Proteinkristallen führte Probleme mit sich, für die Proteine welche nicht in größere Dimensionen wachsen können.

Mit der Entwicklung von Synchrotronstrahlung, wurde, dank der Brillianz des durch sie erreichten Strahls, die notwendige Kristallgröße für konventionelle Röntgenkristallographie gesenkt. Ein freier Elektronen Laser verwendet einen viel helleren Strahl, welcher die, für die Sammlung von Röntgenbeugungsdaten benötigten Dimensionen der Proteinkristalle nochmals reduziert. Konsequenter Weise werden heute Proteinkristalle in Micro- und Nano-Größenordnung bevorzugt. Diese Präferenz kleiner Kristalle führt zu einer großen Nachfrage zur

Entwicklung neuer Instrumente und Methoden zur Detektion, Identifikation und Analyse von Proteinkristallen in Micro- und Nano-Größenordnung. Aktuelle Methoden zur Detektion von Proteinkristallen in Micro- und Nano-Größenordnung beinhalten größtenteils Hellfeld-Bildgebung, Ultraviolett-Fluoreszenz-Bildgebung, Frequenzverdoppelungs-Bildgebung und Pulverdiffraktion. Jedoch hat jede dieser Methoden ihre eigenen Grenzen. Daher wird eine fortgeschrittene und zuverlässige bildgebende Methode benötigt.

Diese Arbeit beschreibt die in-Haus Entwicklung eines multi-modalen multiphoton Instruments, welches sich aus folgenden drei bildgebenden Methoden zusammensetzt. Frequenzverdreifung, Frequenzverdoppelung und Drei-Photonen angeregte ultraviolett Fluoreszenz. Zur Analyse der Machbarkeit und Detektionssensitivität des multimodalen MPM Systems wurden verschiedene Protein- und Salzkristalle mit unterschiedlichen Symmetrien präpariert. Der kombinierte Effekt von THG, SHG und 3PEUVF Bildgebung ist präzise, da das System fähig ist Proteinkristalle in Mikro- und Nano-Göße zu identifizieren und zwischen Protein-, Salzkristallen und amorphen Aggregaten zu unterscheiden.

Während des Testprozesses wurde eine detaillierte Studie der winkelabhängigen SHG Polarisationsantwort durchgeführt. Die Resultate demonstrieren, dass die SHG Polarisationsantwort des Kristalls sehr sensitiv zur Orientation des Kristallgitters ist. Resultierend daraus geht hervor, dass die SHG Polarisation ihr Potential zur Proteinkristall-Detektion und Charakterisierung erweitern kann.

Um die Unterschiede zwischen kommerziellen Systemen und dem MPM System zu vergleichen, wurden die *in vitro* Nanokristallproben simultan mit dynamischer Lichtstreuung, depolarisierter dynamischer Lichtstreuung, Transmissionselektronenmikroskopie und Pulver-Röntgenbeugung getestet.

Die experimentellen Ergebnisse zeigen, dass die nichtlineare Bildgebung von Chiralkristallen zweiter Ordnung und das MPM Bildgebungsinstrument nichtinvasive Detektionsmethoden mit einer hohen Detektionssensitivität darstellen um *in vitro* und *in vivo* Nanokristalle zu detektieren. Proteinkristalle mit Größen im Nano- und Sub-Mikro-Bereich lassen sich effizient durch das MPM System detektieren.

Das MPM System reduziert, durch seine hohe Signalsensitivität, das Risiko falsch-positive und falsch-negative Ergebnisse in der Detektion von *in vitro* Proteinkristallen zu erhalten. Weiterhin bietet das MPM Bildgebungssystem die Möglichkeit *in vivo* Kristalle zu detektieren. Selbst schwache SHG Signale von zentralsymmetrischen Kristallen können mit dem MPM System beobachtet werden.



## Abstract

Biological macromolecules, such as proteins and nucleic acids, are composed of linked monomers and play an important role in biological functions based on their three-dimensional (3D) structures. Proteins are composed of one or more polypeptide chains of different amino acid residues. These polypeptide chains fold into a 3D structure to constitute a functional protein. The 3D structure information of proteins can be applied to analyze protein-ligand processes and interactions. Furthermore, the 3D structure information of proteins can serve as the basis for structure-based target selection for drug discovery research. As it is not possible for protein 3D structures to be seen even under the most advanced light microscope, other methods are employed to determine their 3D structures. Since proteins can form crystals, X-ray crystallography can be used to solve the 3D structures of these proteins. In the deposited protein data bank (PDB), nearly 90% of protein structures are solved through X-ray crystallography. As a result, X-ray crystallography is the fundamental method for characterizing the atomic structure of proteins.

Notably, the primary and oldest method of X-ray crystallography is single-crystal X-ray diffraction. The major challenge of using this method is obtaining well-ordered crystals with a suitable size for crystallographic data collection. The demand for larger and well-ordered protein crystals has introduced difficulties for those proteins which cannot grow to larger dimensions.

With the development of synchrotron radiation, the brilliant beams achieved through synchrotron radiation have decreased the necessary protein crystal size for conventional X-ray diffraction crystallography. A free-electron laser (FEL) uses a much brighter beam, which decreases the dimensions of protein crystals that are required for diffraction data collection. Consequently, today micro-sized and nano-sized protein crystals are preferred. This preference for small crystals creates a strong demand to develop and establish new methods and instrumentation to identify, detect and analyze protein nano- and micro-crystals.

Current methods to detect micro-sized and nano-sized protein crystals mainly include bright-field imaging, ultraviolet fluorescence (UV) imaging, second harmonic generation (SHG) imaging and X-ray powder diffraction. However, each of these imaging methods has its own limitations. Because of this, a reliable and advanced imaging method is required.

The present work describes an in-house developed multi-modalities multiphoton instrument that is composed of three imaging methods, which are third-harmonic generation (THG), second-harmonic generation (SHG) and three-photon excited ultraviolet fluorescence (3PEUVF). To analyze the feasibility and detection sensitivity of the multimodal MPM system, different protein crystals and salt crystals were prepared with different symmetries. The combined effect of THG, SHG and 3PEUVF imaging is precise, as the system is able to identify nano- or micro-sized protein crystals and can distinguish between protein crystals, salt crystals and amorphous aggregates.

During the testing process, a detailed study of the angular-dependent SHG polarization response was conducted. The results demonstrated that the SHG polarization response of the crystal is highly sensitive to the lattice orientation of crystals. As a result, SHG polarization can extend its potential for protein crystal detection and characterization.

To better compare the differences between commercial imaging instruments and MPM system instruments, the *in vitro* nanocrystal samples were simultaneously tested with dynamic light scattering (DLS), depolarized dynamic light scattering (DDLS), transmission electron microscopy (TEM) and X-ray powder diffraction. For second-order nonlinear optical imaging of chiral crystals (SONICC) and MPM imaging instrument, the experimental results illustrate that the MPM imaging instrument processes a non-invasive detection method and high detection sensitivity to detect *in vitro* and *in vivo* protein nanocrystals. Notably, the nano-sized or sub-micro-sized protein crystals can be detected efficiently through the MPM system. For *in vitro* protein crystals, the MPM system reduces the risk of obtaining false-negative and false-positive results in crystal detection through providing a higher signal sensitivity. Moreover, the MPM imaging system offers the possibility for *in*

*vivo* crystals to be detected. Furthermore, weak SHG signals from centrosymmetric crystals are also observed with the MPM system.



# 1 Introduction

## 1.1 Three-dimensional (3D) structure determination of proteins

As one of the most important biological macromolecules, proteins perform biological reactions to maintain life activities. Proteins' functions are determined by their 3D structures which consist of amino acids residues that are linked together (Bittrich *et al.*, 2018). Thus, according to the protein 3D structure, the specificity of active sites and binding sites depends on the precise 3D conformation. Nonetheless, any change to a protein at a structural level that is related to functions may cause the loss of its original functions. Hence, understanding the 3D structure of protein helps in unravelling the mechanism of interactions with substrates or other ligands, so as to provide valuable information in various industrial or biotechnological purposes, such as structure-based drug discovery and drug design that lead to the invention of new medical therapies (Persson *et al.*, 2019).

Currently, there are three main techniques for solving protein structures: X-ray crystallography, cryogenic electron microscopy (Cryo-EM), and nuclear magnetic resonance (NMR). Each of these techniques has its advantages and disadvantages. Among them, almost 90% of protein structures deposited in the PDB are solved by X-ray crystallography (Helliwell, 2017). Thus, X-ray crystallography is still the most prevalent method for protein structure determination.

## 1.2 Early history of protein crystallography

Protein crystallization has been developed for more than 150 years and protein crystals occur *in vitro* and *in vivo*. In 1840, the first protein crystal was discovered in earthworm blood by Friedrich Ludwig Hünefeld who also accidentally observed small plate-like crystals in desiccated human blood samples. In 1864, Felix Hoppe-Seyler named these crystals 'haemoglobin' (McPherson, 1991). Since then, more and more *in vitro* protein crystals had been discovered and yielded by using different crystallization methods

(microbatch, vapor diffusion, etc). However, during the next two decades, *in vitro* crystallization had been deemed as a method for purifying proteins from impure mixtures (Liu *et al.*, 2020). Different from *in vitro* protein crystals, *in vivo* protein crystals were formed in the living cells. Dating back to the 1850s, *in vivo* protein crystals were first reported as Charcot-Leyden crystals (CLCs), which were found in the sputum of asthma patients (Su 2018). Then several other examples (protein crystals in human cataracts and anemia) were discovered (Doye & Poon 2006; Pande *et al.*, 2001). Notably, the *in vivo* protein crystals are associated with different cellular functions and changes (Pande *et al.*, 2001; Banerjee *et al.*, 2016; Müntz, 1998). For example, some *in vivo* protein crystals occur as storage proteins in seeds, and some *in vivo* protein crystals are related to pathogenic reasons, such as asthma and cataract (Su, 2018; Allen, 2019; Pande *et al.*, 2001; Hejtmancik, 2008). However, researchers were not aware of the relationship between protein crystals and structures at that time.

A fundamental change in protein crystallization occurred with the discovery of X-rays in 1895 by Wilhelm Conrad Röntgen (Röntgen, 1896). His discovery contributed to the ground-breaking experiment by Laue and his co-workers who recorded diffraction data on a photographic plate by shining a beam of X-rays through a copper sulphate crystal (Friedrich *et al.*, 1913). In 1913, British physicists Bragg and his son established Bragg's law based on their discovery of intense peaks of reflected X-rays produced by crystals at certain specific wavelengths and incident angles. They found that the diffraction phenomenon could be treated mathematically (Bragg, W. H. 1913; Bragg, W. L. 1913; Bragg, W. H. & Bragg, W. L. 1913). Lawrence Bragg explained this result by modelling the crystal as a set of aligned parallel planes separated by a constant parameter  $d$ . Supposing that a monochromatic wave (any type) enters a set of aligned lattice planes, the plane spacing is  $d$  and the incident angle is  $\theta$ . As shown in Fig. 1-1, the wave travels along AC', while the unreflected wave continues to travel along AB and the path after being reflected by the lattice point B is BC. Notably, there is a path difference between AC' and BC. When the difference in the travel path is equal to integer

multiples of the wavelength, constructive interference will occur (Bragg, W. H. 1913; Bragg, W. H. & Bragg, W. L. 1913).

The general relationship between the wavelength of the incident X-rays, the angle of incidence, and the spacing between the crystal lattice planes of atoms is known as Bragg's Law, expressed as:

$$n\lambda = 2d \sin \theta \quad (1-1)$$

They put forward the basic conditions of X-ray crystal diffraction in an extremely concise way to explain the interference pattern of X-rays scattered by crystals.

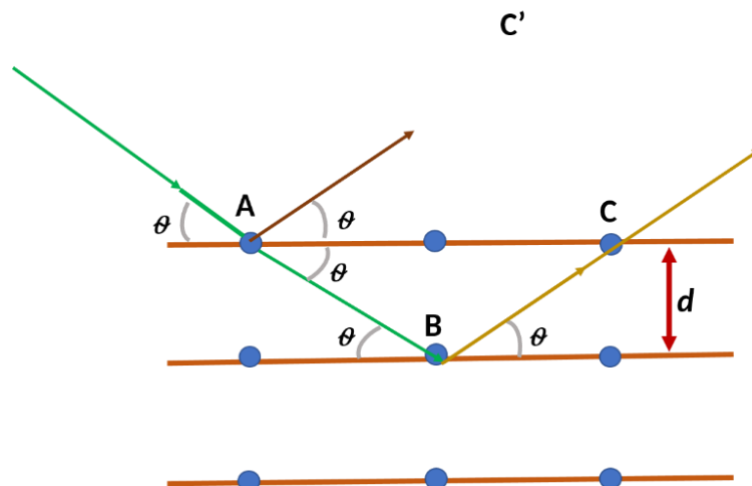


**Fig. 1-1 Schematic representation of Bragg's law conditions.**

In principle, multi-order Bragg diffraction patterns will appear and measurable diffraction intensities will be obtained if Bragg's law is obeyed. These patterns originate from spatial structures with different orientations and different grating constants. As a result, scientists used this principle to determine the crystal structure patterns and lattice constants by analyzing the diffraction spectrum of X-rays of a given wavelength through the crystal. In 1914, the earliest structure solved at the atomic level was the structure of NaCl crystal (McPherson, 1991). In 1937, Max Perutz performed the first experiment to find

out whether the structure of haemoglobin could be determined by X-ray diffraction (Perutz *et al.*, 1960). However, the “phase-loss” problem must be taken into consideration due to the huge number of atoms contained in proteins (the diffraction effects of crystal include the amplitude and the “lost phase” in the measurement). In 1953, Perutz succeeded in incorporating heavy atoms (mercury) into definite positions in the haemoglobin molecule, providing a solution to the phase problem in protein X-ray structure determination (Green *et al.*, 1954). After that, this method was utilized to determine a direct image of the haemoglobin molecule, and the first protein from which a crystal structure could be determined was sperm whale myoglobin in 1958 upon the application of X-ray diffraction (Kendrew *et al.*, 1958) (the early history of X-ray diffraction is shown in Fig.1-2).

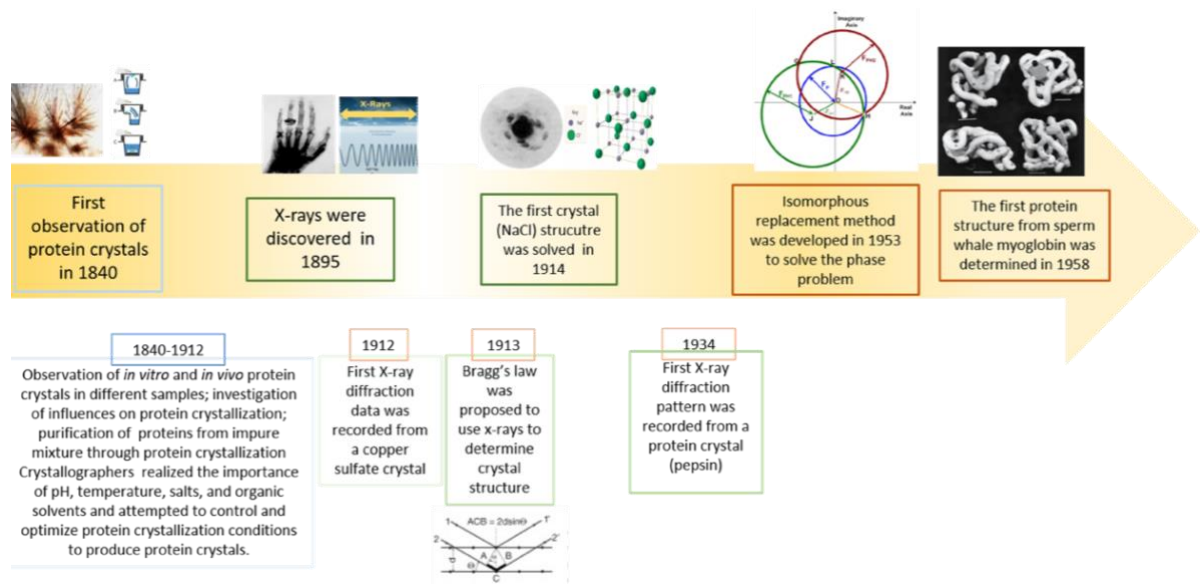


**Fig. 1-2 Early history of protein crystallography.**

### 1.3 Background (Development of solving protein structure)

After the first protein crystal structure was determined through single-crystal X-ray diffraction, there has been a rapid development of protein crystallographic studies. For conventional protein single-crystal X-ray crystallography, crystallographers tried to optimize crystallization conditions to produce larger and well-ordered protein crystals. However, the preference for

large and well-ordered protein crystals is gradually changing with the appearance of advanced X-ray sources and data collection strategies. The progress of protein structures determination strongly relies on the development of light sources and data-collection methods. In section 1.3.1-1.3.2, the development of protein crystallography regarding different sources and data-collection methods are described.

### **1.3.1 Conventional protein single-crystal X-ray crystallography**

In the early times after the discovery of X-rays in 1895, sealed tubes were used to emit X-rays to perform single-crystal X-ray diffraction (Coolidge, 1913). However, X-ray beams generated by those early sealed tube sources was insufficient to obtain acceptable diffraction data from protein crystals. Therefore, the set-up of sealed tubes was gradually replaced by rotating-anode machines, which could deliver more intense X-ray beams in high-speed rotation, to generate more powerful X-rays for recording good diffraction data from protein crystals (Arndt 1990; 2003).

Currently, increasing compact diffractometers based on the rotating-anode sources were designed to perform the single-crystal X-ray diffraction measurement. Typically, in modern single-crystal X-ray diffraction measurement, a protein crystal is mounted on a goniometer and illuminated with a focused beam of X-rays (Fig.1-3). The cryocooling protection for protein crystals is introduced for the X-ray diffraction experiment to collect complete datasets from a single crystal, especially for some samples that are sensitive in long-time exposure measurement. Then the diffraction pattern of regularly spaced spots is obtained and analysed after obtaining the full datasets. Besides, compared with the early stage of data analysis, the implementation of scientific software and computing can shorten the time of data collection, data processing, phasing, model building (researchers can then produce a 3D picture of the density of electrons within the crystal) and refinement (Smyth & Martin 2000).

Notably, the size of the protein crystal used for conventional single-crystal X-ray diffraction is of great importance, as X-ray diffraction peak intensities are proportional to the ratio of the crystal volume to the unit cell volume (Hunter

*et al.*, 2011; Toraya, 2016). If the crystal is too small, poor resolution or even errors may occur. That is to say, smaller crystals are not suitable for conventional single-crystal X-ray diffraction structure analysis because weak signal intensities cannot be used. In general, the size of a single crystal used for conventional X-ray diffraction should not be smaller than 50  $\mu\text{m}$  x 50  $\mu\text{m}$  x 50  $\mu\text{m}$  (Hunter *et al.*, 2011). Hence, researchers were trying to optimize the protein crystallization protocol to produce well-ordered *in vitro* protein crystals with a larger dimension. In contrast to *in vitro* protein crystallization, *in vivo* protein crystallization has been considered as peculiar behaviour and thus those *in vivo* protein crystals had been neglected in optimizing for X-ray diffraction for a long time. Furthermore, although researchers had found that *in vivo* protein crystal formation is related to cellular functions for many years, the determination of the 3D structure of *in vivo* protein crystal was impossible in the past as the size of *in vivo* protein crystal was limited by the cell size (Boudes *et al.*, 2016). Consequently, smaller *in vitro* and *in vivo* protein crystals possessing low diffraction capabilities were not considered in laboratory protein crystallography for many years and prevented a systematic investigation.

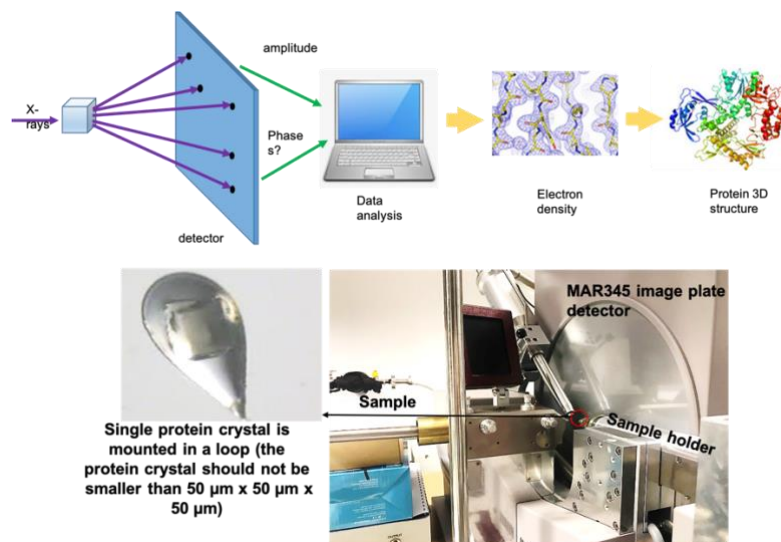


**Fig. 1-3 The process of single-crystal X-ray diffraction.** The upper graph shows the workflow of single-crystal X-ray diffraction, and the lower graph shows the single-crystal X-ray diffraction measurement performed by a lab-based X-ray source diffractometer.

### 1.3.2 New approach to solving protein structure from tiny crystal

As mentioned in section 1.3.1, large and well-ordered protein crystals are required for protein structure determination by the lab-based single-crystal X-ray diffraction. Many proteins, especially membrane proteins and *in vivo* proteins, are difficult to form large crystals but can form nano- or micro-sized crystals (Moraes *et al.*, 2014). Since such tiny crystals are easily damaged before recording diffraction data, they were not considered to perform diffraction for decades until new technologies were developed (Hunter *et al.*, 2011; Mueller-Dieckmann *et al.*, 2005).

One approach is synchrotron radiation crystallography. A synchrotron facility aims to accelerate electrons to high energy and then change radiation direction periodically. Electrons generated from a heated cathode are generally injected into a linear accelerator for acceleration and then inserted into a circular storage ring, keeping on a circular path by bending magnets in the storage ring (Rowe & Mills 1973). Finally, X-rays beams emitted by the electrons are directed towards "beamlines" stations that surround the storage ring (As shown in Fig. 1-4).

The third-generation synchrotron radiation has been a powerful tool for protein structure research from the very beginning because of its high-intensity and high-energy photon beams. With the increasing flux of new synchrotron radiation sources (third generation), the minimal size of the crystal required for measuring reliable diffraction intensities continuously decreases (Su *et al.*, 2015; Smith *et al.*, 2012). Compared with laboratory-based X-ray sources, synchrotron radiation sources enable higher-resolution structure determinations and almost 90% of the X-ray single-crystal structure determinations being from synchrotrons (<http://biosync.sbkb.org>).

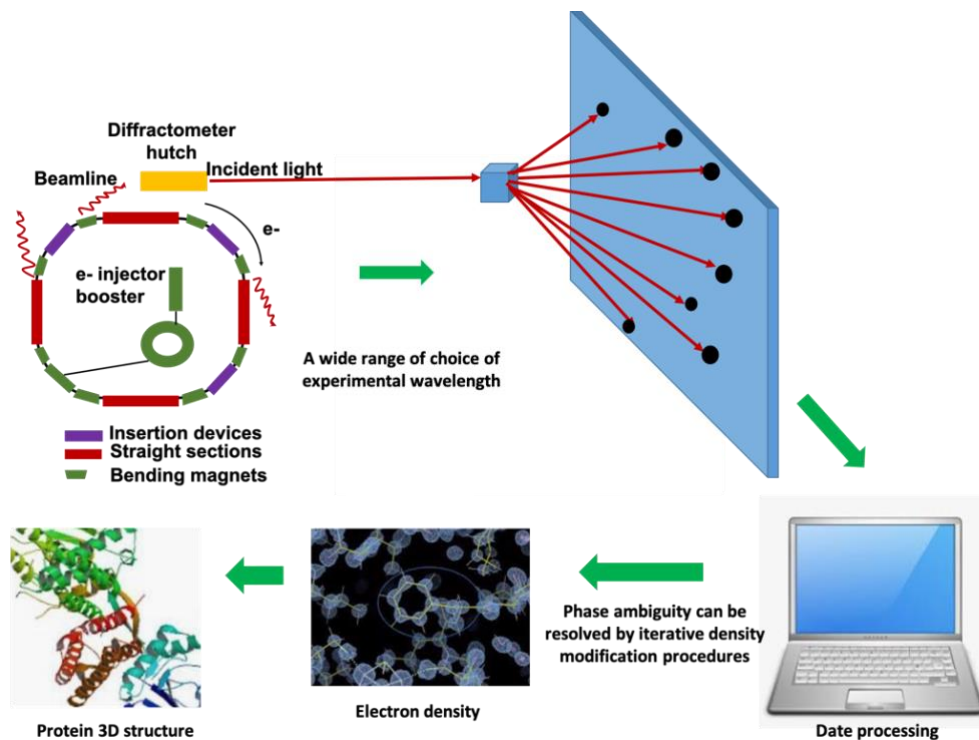


**Fig. 1-4 The process of synchrotron radiation single-crystal X-ray diffraction.**

Another approach is XFEL crystallography, the fourth-generation sources emerging in the form of free-electron lasers (FEL) (Oberthür, 2018). Compared with the current synchrotron radiation sources, the fourth-generation sources have a peak brilliance of more than 100 million times higher (Borland *et al.*, 2014; Liu & Lee 2019; Marx, 2014). However, nano- or micro-sized crystals (less than 5  $\mu\text{m}$ ) are sensitive to radiation damage, which may disrupt the lattice structure when using high-intensity synchrotron sources for crystal diffraction data collection (Holton & Frankel 2010). Although freezing the crystal with liquid nitrogen at a low temperature can effectively reduce radiation damage, the damage cannot be avoided entirely. In 2000, the results of molecular dynamics simulation performed by Janos Hajdu's research group at Uppsala University in Sweden showed that the structure information could be obtained before the molecule was damaged by irradiating the crystal with a suitable femtosecond high-intensity X-ray pulse (Neutze *et al.*, 2000). Thus, the concept of "diffraction before destruction" was

proposed and then performed (Chapman *et al.*, 2011; Spence & Chapman 2014; Tavella *et al.*, 2011).

The X-ray free-electron lasers (XFELs) can provide short femtosecond X-ray pulses with data collected in a serial fashion. Then a large number of tiny crystals are delivered to the X-ray beam in their mother liquor at room temperature in a liquid jet, which is termed serial femtosecond X-ray crystallography (SFX). With the ability to collect data on crystals  $<1\ \mu\text{m}$  in diameter, SFX allows for the structural determination of challenging proteins without forming larger crystals, which are in some cases, are submicron crystals rather than those with a few microns. With such a high intensity, diffraction data collection applying the nano- or micro-sized protein crystals has become possible (Boutet *et al.*, 2012; Bogan *et al.*, 2010; Batyuk *et al.*, 2016; Wiedorn *et al.*, 2018; Lomelino *et al.*, 2018; Kupitz *et al.*, 2014). The schematic graph of XFEL crystallography and crystallography experimental set-up can be found in Fig. 1-5. The recent development of femtosecond nano-crystallography methods has also opened a new route in *in vivo* protein crystal structural biology (Koopmann *et al.*, 2012). In 2007, the first native structure of *in vivo* protein crystals, the insect virus polyhedra, was reported (Coulibaly *et al.*, 2007). Also, natively inhibited Trypanosoma brucei cathepsin B structure (*in vivo* crystal) was determined in 2012 upon the application of the combination of the FELs of Linac Coherent Light Source (LCLS) and continuous SFX (Redecke *et al.*, 2013). The XFEL-based femtosecond nano-crystallography provides the possibility of determining the 3D structure of proteins. The size of protein crystals suitable for femtosecond nano-crystallography ranges from 200 nm to  $2\ \mu\text{m}$  (Chapman *et al.*, 2011). Inspired by SFX, the serial crystallography experiment can also be performed on the synchrotron radiation (SR) by carrying out helical line scans at a synchrotron source, paving the way for the implementation of serial synchrotron X-ray crystallography (SSX) (Yamamoto *et al.*, 2017).

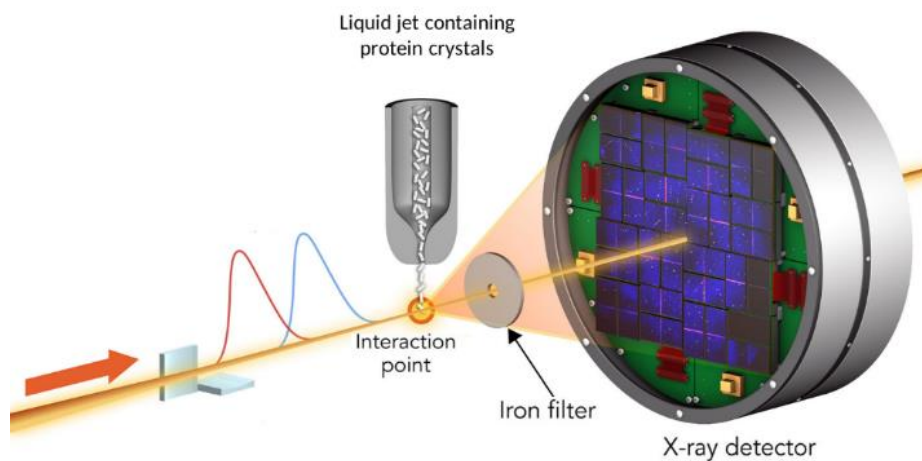


**Fig. 1-5 Schematic of XFEL crystallography and crystallography experimental set-up.** Each protein crystal is hit by a single X-ray pulse with THz frequency to form a single diffraction pattern. The detector records the diffraction patterns from crystals flowing in a liquid jet before damage (Boutet *et al.*, 2012).

In the meantime, various sample delivery systems developed for SFX and SSX enable fast data collection, lower sample consumption, and weaker diffraction background (Zhao *et al.*, 2019). Briefly, protein crystals can be delivered through a gas-focused dynamic virtual nozzle (GDVN), a double flow focusing nozzle (DFFN), or a microfluidic device (as shown in Fig. 1-6). They can also be embedded in a lipid cubic phase (LCP) or delivered on a driving tape (Stagno *et al.*, 2017; Meents *et al.*, 2017; Martin-Garcia *et al.*, 2019; Tolstikova *et al.*, 2019; Cheng, 2020; Monteiro *et al.*, 2019; 2020; Basu *et al.*, 2019). Since then, the existence of SFX and SSX has opened a new era for the structural determination of proteins.

In addition, microcrystal electron diffraction (MicroED) emerged in late 2013 as a powerful method for protein structure determination (Shi *et al.*, 2013; Nannenga *et al.*, 2014). This method was developed for the

structure determination of protein nano- or micro-sized crystals that are not suitable for conventional X-ray diffraction. MicroED was able to collect useful data from tiny crystals that are smaller (approx. 100 nm), as electrons interact much more strongly with matter than X-rays and deposit less energy onto the sample.

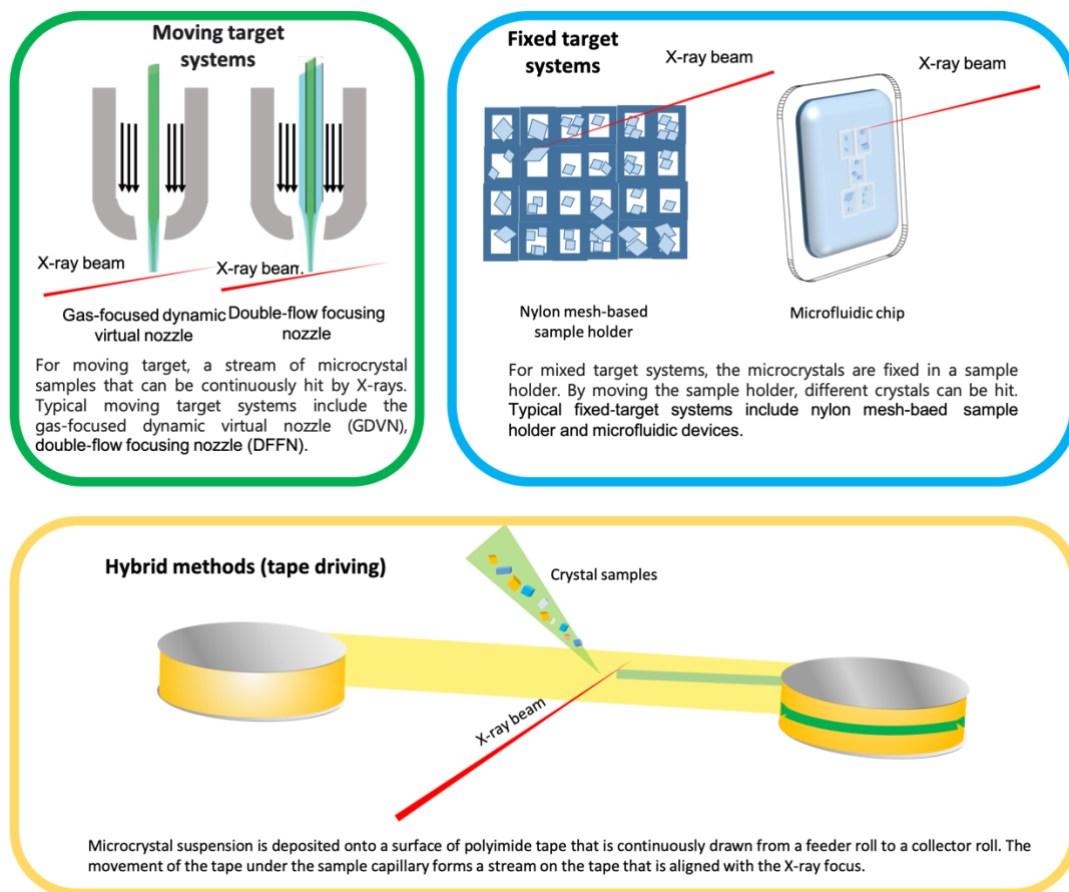


**Fig. 1-6 Schematic representation of sample delivery methods for serial synchrotron and femtosecond crystallography.**

### 1.3.3 Time-resolved crystallography

Furthermore, understanding the molecular function and the detailed mechanism is vitally important, so as to study the dynamic processes happening in the biomolecules. Capturing the structure change in reaction initiation and probing is difficult in the time-resolved experiment due to the very short-lived intermediate reaction states (Orville, 2018). Time-resolved X-ray diffraction is a unique tool for visualizing reactions of interest in the crystal at different time points through X-ray crystallography imaging (Schotte *et al.*, 2003). In this method, the investigation into real-time structural changes while performing their functions can be observed. So far, short and intense X-ray pulses at third-generation synchrotron sources have been used to perform a time-resolved crystallography experiment to observe reactions rapidly

occurring in molecules within crystals (Yorke *et al.*, 2014; Schmidt, 2019; Levantino *et al.*, 2015). However, the synchrotron time-resolved crystallography experiment still needs the well-ordered and relatively larger protein crystals under the cryo-protection environment to avoid damage. After the serial femtosecond crystallography development, conducting time-resolved experiments is easier to be carried out at room temperature. This method has created the possibility of using nano- or micro-sized protein crystals for a time-resolved crystallography experiment on timescales from fs to seconds. Besides, time-resolved experiments can be performed at room temperature to capture near-physiological conformation changes. Currently, pharmacologically and biomedically important reactions can be observed through time-resolved experiments of femtosecond nano-crystallographic methods (Spence *et al.*, 2012; Spence, 2017; Neutze, 2014; Pandey *et al.*, 2019).

## **1.4 Linear optical imaging methods for detecting and identifying protein crystal**

As mentioned in section 1.3, serial X-ray crystallography and MicroED require a much smaller size of protein crystals. Thus, the requirement tendency of smaller protein crystals leads to two problems for the detection: 1) how to identify the protein crystals efficiently if they are in nano- or micro-size; 2) how to distinguish salt crystals from protein crystals yielded by protein crystallization screening experiments. Thus, a method for determining whether protein crystals in smaller dimensions are proteins or have grown at all is suggested. In the following sections (1.4.1-1.4.4), different linear optical imaging methods for protein crystals detection are demonstrated.

### **1.4.1 Conventional optical microscopy**

The optical microscope (also referred to as a light microscope) is the most widely used imaging tool for generating magnified images of small crystals in labs. The basic optical microscope involves a bright field imaging applying transmitted light in the imaging process. In the bright field, the background is

bright while the target is dark. Besides, many complicated designs of the optical microscope aim to improve imaging contrast and optical resolution.

Due to the limited resolving power of the visible light, the maximum magnification of an optical microscope is usually limited to about 1000 times, which is the product of the eyepiece (10 times) and the objective lens (100 times), and the total magnification is 1000 times.

In Fig. 1-7, different protein crystals are shown in different sizes applying the conventional optical microscope. However, as shown in Fig. 1-7f, identifying smaller-sized protein crystals is challenging. Besides, the bright-field imaging cannot discriminate between protein crystals and salt crystals, as most of the crystals are colorless.

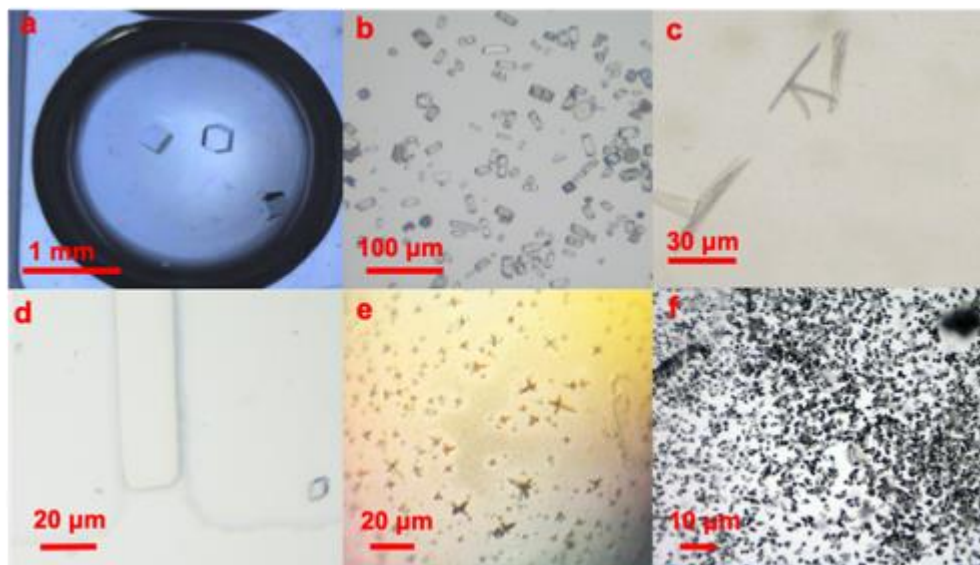


**Fig. 1-7 Examples of various protein crystals detection applying the conventional optical microscopy.**

(a) Lysozyme crystals. (b) Thermolysin crystals. (c) Glucose isomerase crystals. (d) Proteinase K crystals. (e) Hemoglobin crystals. (f) Thaumatin crystals.

Since the conventional optical microscope is limited in terms of distinguishing the protein and salt crystal, the “crush test” is the alternative. In the "crush test" method, the crystal is poked with a sharp needle. A crystal that is not easy to break apart is likely to be salt crystal, while the crystal is likely to be

protein crystal if the crystal is easy to break apart. This test is not very convincing, as some protein crystals will become more difficult to break apart with an increase in the crystal size. Thus, the alternative way to distinguish protein crystals and salt crystals is labelling the protein crystal with some dyes (such as JBS Deep Purple, in Fig. 1-8), which are able to permeate through the solvent channels of proteins and thus color proteinaceous samples (including protein crystal and amorphous protein aggregation). In contrast, salt crystals will remain colorless (Wilkosz *et al.*, 1995). Nevertheless, the differentiation nano or micro-sized protein crystals from amorphous with dyes applying normal bright-field microscopy is still difficult. Moreover, these dyes are for *in vitro* use only, being unable to be used for *in vivo* protein crystal samples. In consequence, new imaging methods for micro-sized and nano-sized protein crystals are still needed to be developed.

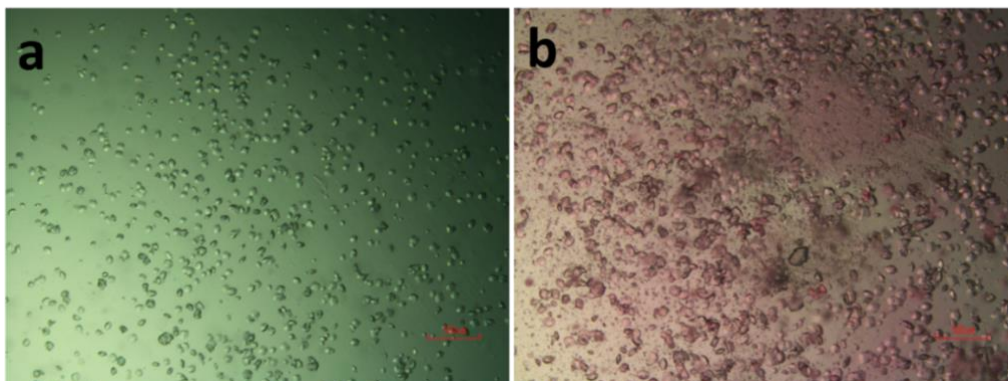


**Fig. 1-8 Unstained protein crystals and stained protein crystals.**  
(a) Unstained protein crystals. (b) Stained protein crystals.

#### **1.4.2 Transmission electron microscopy**

Currently, the most reliable method for microcrystal characterization is transmission electron microscopy (TEM), the imaging principle of which is similar to that of the optical microscope. TEM has three essential systems: (1) an electron gun for the generation of the electron beam, (2) an illumination system, consisting of the condenser lens and condenser aperture, and (3) an imaging system, including the intermediate and projector lenses. The

difference is that TEM uses an electron beam as the illumination source instead of the visible light (as shown in Fig. 1-9). Since the resolution of microscopes is limited by the wavelength (the wavelength of high-speed electrons is shorter than that of the visible light), the theoretical resolution of TEM (about 0.1 nm) is much higher than that of the conventional optical microscope (about 200 nm). However, TEM requires extensive sample preparation efforts and may, for example, involve negative staining, chemical cross-linking, or cryo-preparation. In addition, due to the weak penetrating power of electron beams, the sample used for electron microscopy must be made into ultra-thin sections with a thickness of around 100 nm.

TEM is a powerful tool to characterize protein crystal, especially for revealing crystal morphology and size, crystal orientation, and crystal defects. The most significant characteristic of TEM is to show local structures in an atomic scale or a nanometer scale. For protein crystal characterization, TEM images can distinguish the protein crystal from the salt crystal by visualizing and calculating the crystal lattice (calculating the distance between the lattice spacing) (Stevenson *et al.* 2014a; 2014b).

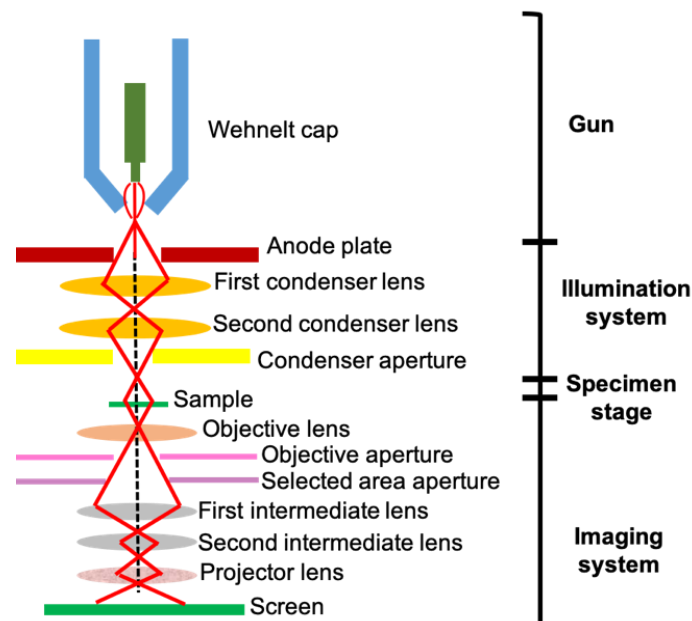


**Fig. 1-9 Schematic diagram of TEM system.**

### 1.4.3 Dynamic light scattering (DLS) and depolarized dynamic light scattering (DDLDS)

Dynamic light scattering (DLS), also called quasi-elastic light scattering, is a physical characterization method used to measure the particle size distribution in a solution or suspension (Falke *et al.*, 2018; Baitan *et al.* 2018; Oberthür *et al.*, 2012; Dierks *et al.*, 2008; Stetefeld *et al.*, 2016; Kadima *et al.*, 1990). When the light hits a small particle much smaller than its wavelength, the light will scatter in all directions. If the light source is a laser in a certain direction, the intensity of the scattered light will not be constant but fluctuate with time. This fluctuation results from Brownian motion undergone by the particles and thus the distance between each scattered particle changes with time (Bloomfield, 1981). Since the velocity of the particles in Brownian motion is related to the particle size, the time dependence of the intensity is related to the particle size. Large particles move slowly, while small particles move fast. If large particles are measured, the intensity of the scattered light spot will fluctuate slowly because of their slow motion. On the contrary, if small particles are measured, the density of the scattered light spots will fluctuate rapidly due to their rapid movement. Then the scattered light will produce constructive or destructive interference from different particles, which contain information about the time scale of the scattered intensity (Baldwin *et al.*, 1986).

The correlation curve or correlation function is the primitive signal obtained by the DLS measurement, including the information about the particle size and its distribution.

The diffusion coefficient of the particle  $D$  (unit is  $\mu\text{m}^2/\text{s}$ ), also known as the hydrodynamic diameter  $D$ , is obtained through the Stokes-Einstein equation. Finally, the particle size and its distribution are calculated by the light intensity fluctuation change and the light intensity correlation function.

$$D = \frac{kT}{3\pi\eta D} \quad (1-2)$$

Where  $k$  is Boltzmann's constant,  $T$  is the ambient temperature (unit is K), and  $\eta$  is the solvent viscosity (unit is cp).

In Fig. 1-10, the DLS instrument used in the lab is shown below. However, DLS can only measure the particle size distribution in a solution or suspension without identifying whether the particle is crystal or non-crystal.

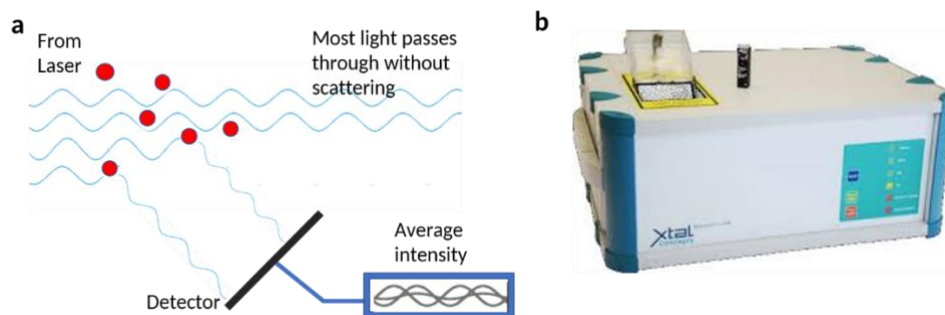


**Fig. 1-10 Schematic graph of DLS and DLS instruments.**

(a) Schematic graph of DLS. (b) DLS instrument used in the lab. For the DLS measurement, a laser with a wavelength of 660 nm and an output power of 100 mW is used.

This bottleneck is overcome/reduced, in part, by applying depolarized dynamic light scattering (DDLS) where the experimental set-up is used to detect nanocrystal formation (Schubert *et al.*, 2015). The DDLS method can identify nanocrystals via the detection of the depolarized signal, which is a combination of form and intrinsic birefringence (Bragg & Pippard 1953; Oldenbourg & Ruiz 1989). Resulting from the anisotropy of the individual protein molecules in the crystal lattice, the form birefringence is very sensitive to the direction in a geometrically ordered material such as crystal (Owen & Garman 2005). Thus, the DDLS method can identify the presence of ordered crystals owing to the birefringent property. The presence of nanocrystals in the early stages of the crystallization process can be identified through the detection of the DDLS signal.

The DDLS intensity depends on two components: the amplitude caused by the particle rotation and the phase caused by the center of the mass movement. When depolarized scattering is measured, the interpretation is easier as  $D_t$  is a constant contribution across all scattering angles. As a result, the translational diffusion constant  $D_t$  is derived from the Stokes–Einstein equation.

$$D_t = \frac{kT}{6\pi\eta D} \quad (1-3)$$

The rotational diffusion constant  $D_r$  can be determined from the rotational decay time constant by the Stokes-Einstein-Debye equation:

$$D_r = \frac{kT}{8\pi\eta D} \quad (1-4)$$

Where  $K$  is the Boltzmann constant,  $\eta$  is the viscosity,  $T$  is the temperature, and  $r$  is the particle radius. In Fig. 1-11, the DDLS instrument used in the lab is shown below.

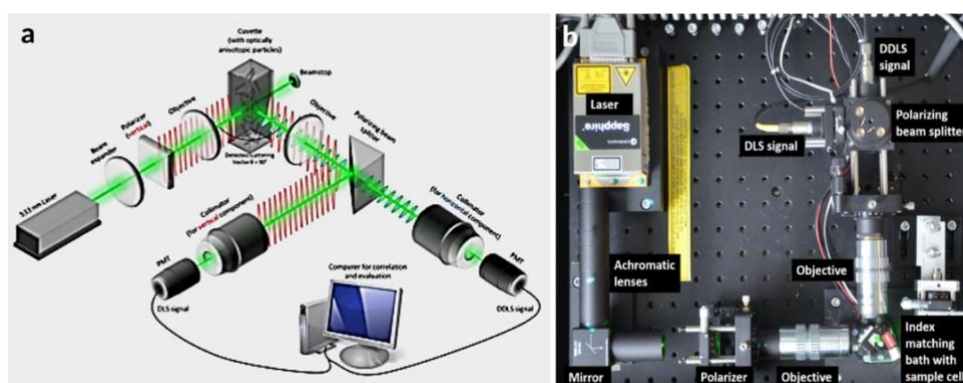


**Fig. 1-11 Schematic and photographic presentation of DDLS set-up.** (a) Schematic DDLS set up. (b) DDLS instrument used in the lab. For the DDLS measurement, a sapphire laser with a wavelength of 532 nm and an output power of 100 mW is used (Modified from Schubert *et al.*, 2015).

#### 1.4.4 X-ray powder diffraction

Another reliable and direct method for identifying protein crystal is X-ray diffraction. For protein crystal identification, protein crystals exhibit many closely spaced diffraction spots as protein crystals possess larger unit cells than salt crystals. By contrast, salt crystals only show a few scattering spots (Stahl *et al.*, 2013). However, protein crystals may be too small or in poor diffraction quality, possessing low diffraction capabilities for conventional X-ray single-crystal diffraction methods. Thus, these small protein crystals can be identified by performing X-ray powder diffraction. The X-ray powder

diffraction can be used to quickly and accurately identify a known substance, or to verify that two unknown samples are the same material. For nano- or micro-sized protein crystal identification, X-ray powder diffraction is a reliable way to distinguish between the protein crystal, simple salt crystal, and amorphous (Spiliopoulou *et al.*, 2020). Different from X-ray single-crystal diffraction, X-ray powder diffraction is based on the sample of countless crystal particles instead of a single crystal. Thus, the powder diffraction pattern crystalline sample is comprised of intense rings rather than spots (Fig. 1-12). Also, X-ray powder diffraction is able to provide information about the diffraction quality of protein crystals but demands a relatively large sample volume (Stahl *et al.*, 2013; Devaud *et al.*, 1992; Norrman *et al.*, 2006).

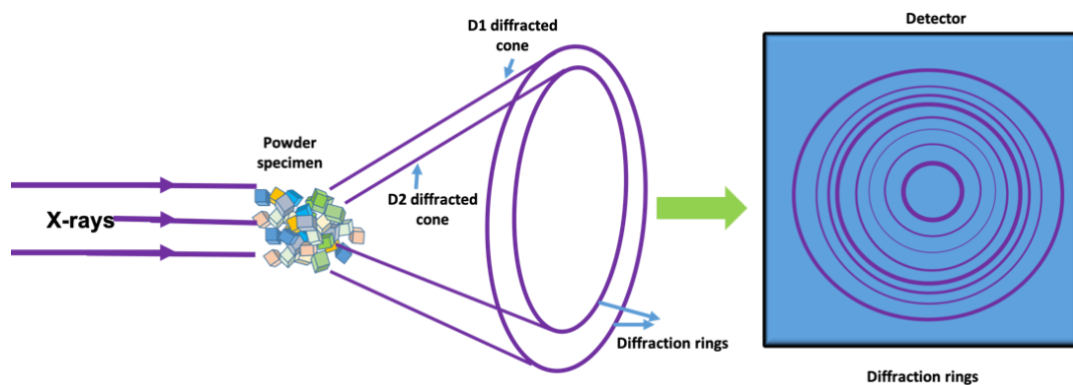


**Fig. 1-12 Schematic representation of X-ray powder diffraction.**

## **1.5 Theory (Nonlinear optical imaging methods)**

Nonlinear optical imaging technology is an important imaging method for the non-invasive visualization of biological samples. Nonlinear optical imaging can be classified into three categories: multiphoton fluorescence, high harmonic generation, and vibration scattering. In bio-imaging, high harmonic generation and fluorescence imaging methods are most widely used.

### **1.5.1 Multiphoton fluorescence imaging**

Multiphoton fluorescence imaging is a powerful tool for capturing high-resolution and three-dimensional images of samples. Two-photon and three-photon fluorescence imaging methods are widely used to study living cells and

tissues (Benninger & Piston 2013; Guesmi *et al.*, 2018; Cheng *et al.*, 2014; Rowlands *et al.*, 2017; Masters *et al.*, 1997).

Unlike single-photon fluorescence, two-photon fluorescence involves two photons interacting simultaneously with the fluorophore to illicit a transition to the excited state (Fig. 1-13). The working principle of three-photon fluorescence is similar to that of two-photon fluorescence. The difference is that three photons are simultaneously absorbed by combining their energies to provoke the electronic transition of a fluorophore to a higher electronic state (Fig. 1-13). The two photons in two-photon fluorescence and three photons in three-photon fluorescence should have longer wavelengths than that required for the single-photon excitation as the energy level of a photon (energy of a photon) is inversely proportional to its wavelength.

For two-photon fluorescence, a laser emitting a wavelength between 700 nm and 1 000 nm is able to excite a fluorophore between 400 nm 500 nm (almost half of the excitation wavelength). The three-photon fluorescence has lower energy and longer wavelengths than those used to excite the same fluorophore in two-photon fluorescence imaging. For instance, three photons having a wavelength of 1050 nm can be combined to excite a fluorophore in approximately 350 nm (almost one-third of the excitation wavelength) (Chung *et al.*, 2018; Denk *et al.*, 1990).

Advantages of two-photon and three-photon fluorescence imaging methods are that they can penetrate deeper into the sample due to the multiphoton absorption (the background signal is strongly suppressed with more photons absorption) and decrease photodamage and photobleaching due to the lower level of energy with a longer wavelength, which is vitally essential when observing living samples (Drobizhev *et al.*, 2011; Hell *et al.*, 1996).

Compared with the two-photon fluorescence, the three-photon fluorescence has an increased penetration depth and higher resolution due to longer wavelengths, which are scattered lesser than shorter wavelengths and beneficial to high-resolution imaging (Benninger & Piston 2013).

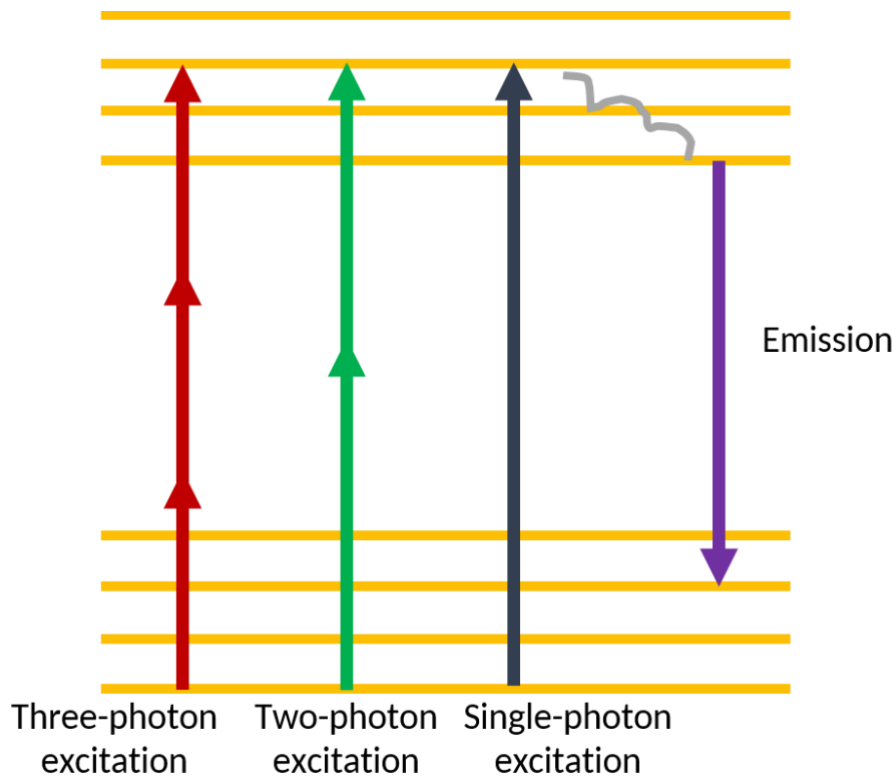


**Fig. 1-13 Multiphoton fluorescence diagram.** Energy diagram showing single-photon, two-photon and three-photon excitation fluorescence.

Multiphoton fluorescence microscopy used for detecting protein crystals has been developed in recent years (Albota 1998; Watts *et al.*, 2010; Madden *et al.*, 2011; Judge *et al.*, 2005). UV-fluorescence imaging is the most common method applied to the identification of protein crystals (Dierks *et al.*, 2010; Gill, 2010; Vernede *et al.*, 2006). The UV fluorescent amino acids contain tryptophan (Trp), tyrosine (Tyr), and phenylalanine (Phe), which can emit fluorescence without any dyes or markers. Trp, Tyr, and Phe have different fluorescence excitation and emission spectra due to their side-chain chromophore groups (Determann *et al.*, 1998). As shown in Fig. 1-14, Trp has the highest fluorescence absorption intensity, Tyr has the second highest, and Phe contributes the least. The emission of Phe can rarely be observed as the Phe is not absorbed under most experimental conditions. Consequently, the fluorescence of proteins is mainly derived from Trp and Tyr residues. Since Trp residues are sensitive to the changes in the microenvironment and most

proteins contain several different Trp residues, they are often used as endogenous fluorescent probes to study the conformation of proteins in the solution state as well as the detection of protein crystals.

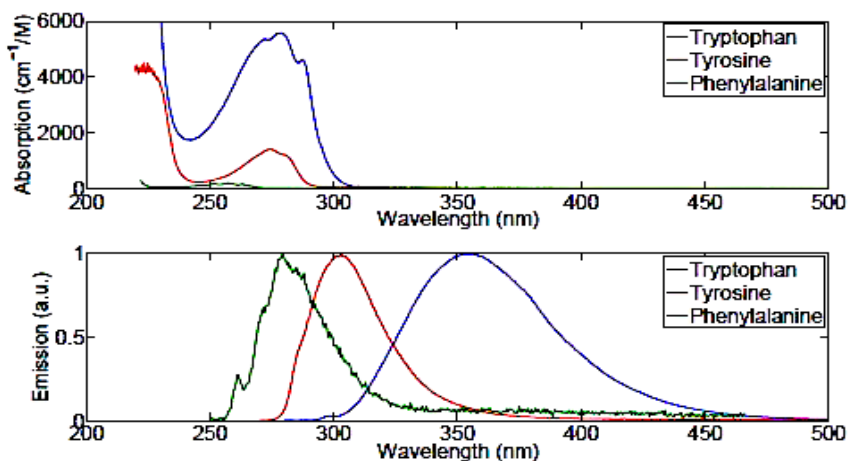


**Fig. 1-14 Absorption and emission spectra of tryptophan, tyrosine, phenylalanine** (Modified from Lakowicz, 2006).

The imaging of intrinsic protein fluorescence is the most common technique in distinguishing protein crystals from salt crystals. Moreover, tryptophan absorbs light at a wavelength of  $290 \pm 5$  nm with a fluorescent emission of 320–350 nm, which can be used to visualize proteins both in crystals and in solution (Dierks *et al.*, 2010). Commercially available instruments for UV imaging commonly utilize UV light at 295 nm.

UV imaging is generally combined with conventional optical microscopes to detect protein crystals. The normal approach is the introduction of a UV light source to achieve UV imaging. In Fig. 1-15, this schematic set-up of the UV imaging microscope used in the lab and UV imaging of a glucose isomerase crystal is shown. The UV-imaging system consists of a two-light source (UV and bright light) system and a CCD microscope system equipped with a motorized XY stage. With the CCD microscope system equipped with a motorized XY stage, all droplet positions in multi-well crystallization plates used in crystallization experiments can be scanned and located.

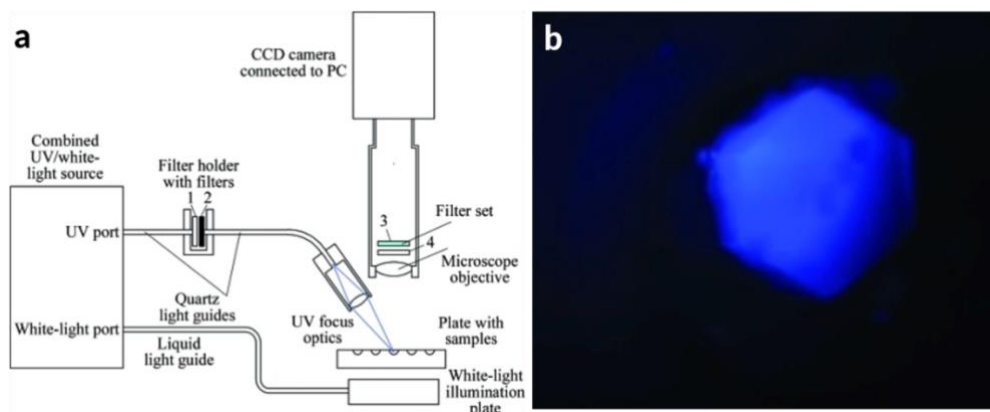


**Fig. 1-15 Schematic set-up of UV instrument applied to protein crystal detection experiment.**

(a) Schematic set-up of a UV instrument. (b) UV imaging of a large glucose isomerase crystal (Modified from Dierks *et al.*, 2010).

### 1.5.2 High harmonic generation imaging

High harmonic generation is a nonlinear optical phenomenon. Different from multiphoton excitation fluorescence (MPEF), high harmonic generation does not involve photon absorption by the sample nor an electron transition between real energy states (Imasaka *et al.*, 1990). When a fundamental frequency wave of a single frequency is projected on a nonlinear medium, lightwave radiation with a frequency two to three times or even higher than the incidence light wave (base frequency wave) is generated due to the coupling effect of the high-order nonlinear polarization coefficient.

Among a variety of nonlinear optical phenomena, SHG ( $n = 2$ ) and THG ( $n = 3$ ) are the most common harmonic generation (HG) processes, which are capable of visualizing objects with special characteristics. In this section, the theory of higher harmonic generation is introduced as follows.

At a low field ( $\vec{E}$ ), the amount of induced dipole ( $P$ ) is proportional to the electric field, as shown in Equation (1). Where  $\chi$  is the electric susceptibility,  $\epsilon_0$  is the permittivity. The  $P$  is the linear response of the electric field.

$$P = \epsilon_0 \cdot \chi \cdot E \quad (1-5)$$

The induced polarization of a matrix under an electric field can be calculated through the Maxwell Equation.

$$P = \epsilon_0 [\chi \cdot E + \chi^2 \cdot E^2 + \chi^3 \cdot E^3 \dots] \quad (1-6)$$

Eqs. (1-5) and (1-6) are results of polarization calculated from the Maxwell equation, and the higher-ordered terms under the higher field indicate the nonlinear interactions.

Equation (1-5) can also be written as:

$$E = E_0 \cdot \sin(\omega t) \quad (1-7)$$

Equation (1-6) can also be written as:

$$P = \epsilon_0 [\chi \cdot E_0 \cdot \sin(\omega t) + \chi^2 \cdot E^2 \cdot (1 - \cos(2\omega t)) \dots] \quad (1-8)$$

The second term,  $\chi^2 \cdot E^2 \cdot (1 - \cos(2\omega t))$ , indicates the electromagnetic waves with the frequency doubling that of the input waves. This is the second-harmonic generation, which can also be written as Equation (1-9),

$$P_i(2\omega) = \frac{1}{2} \epsilon_0 \chi^{(2)}_{ijk}(2\omega; \omega, \omega) E_j(\omega) E_k(\omega) \quad (1-9)$$

where  $\chi^{(2)}_{ijk}(2\omega; \omega, \omega)$  represents a second-order nonlinear susceptibility tensor, which is a tensor of the third rank responsible for the SHG process, while  $E_j(\omega)$  and  $E_k(\omega)$  are the laser field amplitude.

$P_i(2\omega)$  refers to the induced SHG nonlinear polarization in the direction at a frequency twice of the fundamental frequency, coupling and generating light field radiation  $E_i(2\omega)$  twice (Fig. 1-16 shows the energy band diagram of SHG).

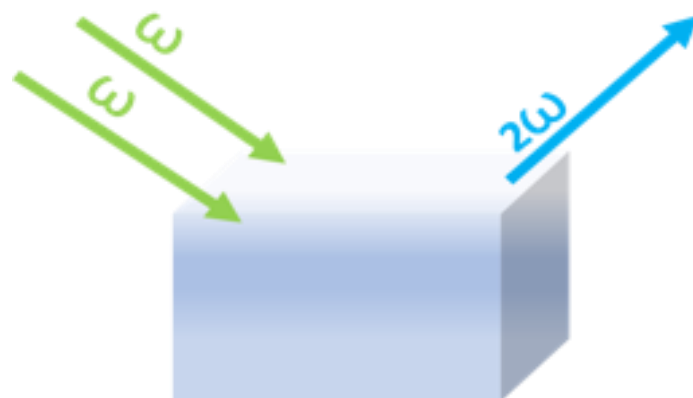


**Fig. 1-16 Energy band diagram of second-harmonic generation.**

THG, a nonlinear optical phenomenon, represents the third-harmonic generation and is the generation of light at a tripled frequency (Fig. 1-17 shows

the energy band diagram of THG). The interaction of nonlinear polarization and the excitation light is realized through a nonlinear susceptibility. Similarly, the THG process is related to the creation of a third-order nonlinear polarization  $P^{(3)}$  (at  $3\omega$  angular frequency) according to Equation (1-10).

$$P^{(3)}(3\omega) = \frac{1}{4} \epsilon_0 \chi^{(3)}_{ijkl}(3\omega : \omega, \omega, \omega) E_j(\omega) E_k(\omega) E_l(\omega) \quad (1-10)$$

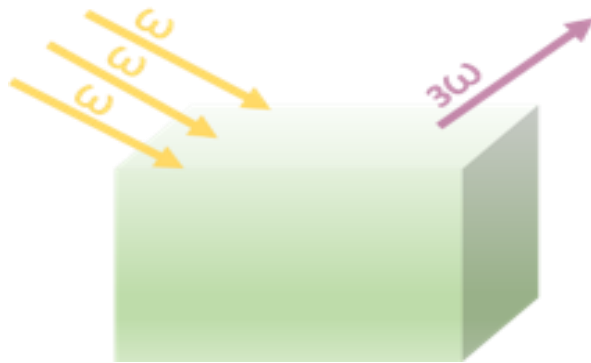


**Fig. 1-17 Energy band diagram of third-harmonic generation.**

SHG, as a nonlinear phenomenon, has been widely applied in material studies for surface monolayer detection and nonlinear crystal characterization, as well as biological tissue imaging (Campagnola & Loew, 2003; Lukina *et al.*, 2019). Today, SHG combined with scanning microscopes is an emerging technique for a wide range of biological, medical, and material investigations (Fine & Hansen 1971; Freund *et al.*, 1986). Compared with amorphous aggregates and centrosymmetric materials, SHG is only allowed in samples that do not possess centrosymmetry (Sun, 2005; Wampler *et al.*, 2008). Since the majority of the protein crystals are non-centrosymmetric and structurally ordered media, the second-harmonic generation signal can be obtained from the protein crystal sample instead of protein aggregation. Therefore, SHG can also be applied to the identification of protein crystals.

Being sensitive to interfaces with optical inhomogeneity, THG is a label-free multi-photon scattering process (Debarre *et al.*, 2006; Oron *et al.*, 2004; Tsang,

1995). In life science, THG imaging has been widely used in the bio-imaging field (Horton *et al.*, 2013). For instance, THG signals occur at interfaces between protein aggregates and water (Rehberg *et al.*, 2011; Weigelin *et al.*, 2012). Furthermore, THG signals can also be found in inorganic structures such as calcified bone and enamel in teeth (Chen *et al.*, 2008; Oron *et al.*, 2004). Different from SHG imaging, THG imaging is not limited by the observation of centrosymmetric materials. Even in materials with inversion symmetry, the third-order nonlinear polarization will not be zero. Thus, THG signals can be detected from crystals with and without centrosymmetric structures.

### **1.6 Second-order nonlinear imaging of chiral crystals (SONICC) for detecting small protein crystal**

According to a recent report, 84% of the protein crystals deposited in the PDB were non-centrosymmetric (Newman *et al.*, 2016). However, non-centrosymmetric salt crystals can also result in this false-positive SHG signal. Those salt crystals can originate from a precipitant solution used in the protein crystallization experiment. In general, UV-fluorescence imaging techniques are applied to further distinguish protein crystals from salt crystals. As shown in Fig. 1-18, the strategy to combine SHG with UV imaging methods to achieve protein crystal identification more efficiently and reliably. Among the existing commercially available instruments, an instrument capable of simultaneously detecting the UV-fluorescence signal and the SHG signal is developed, termed SONICC, which employs three imaging methods, including bright-field, SHG, and ultraviolet two-photon excitation fluorescence (UV-TPEF) imaging (Kissick *et al.*, 2011).

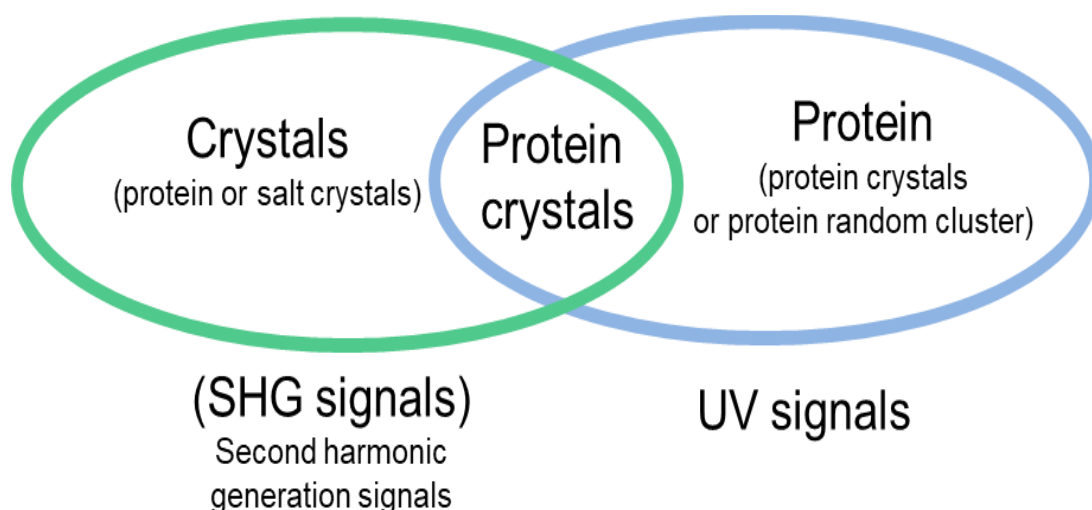


**Fig. 1-18 Strategy of combining UV and SHG image methods.**

SHG results from all chiral crystals, including some salt crystals. These chiral salts and small molecule crystals will lead to false-positive phenomena when SHG imaging occurs. To prevent this, SONICC is also equipped with UV-TPEF imaging, which is analogous to traditional UV fluorescence and creates images based on the fluorescence of UV excited amino acids such as tryptophan. In particular, UV-TPEF is a multi-photon technique that uses longer wavelengths of excitation than traditional linear imaging, thereby providing significant advantages, including compatibility with more plates, less damage to protein, and confocal imaging. The Formulatrix SONICC instrument (as shown in Fig. 1-19a) is composed of a laser pulse generator, SONICC optics, power switches, LBO (Lithium Triborate –  $\text{LiB}_3\text{O}_5$ ) crystal oven, SHG Objective, photomultiplier (PMT), motorized condenser, door sensor, and visible camera (as shown in Fig. 1-19b). Among these components, the LBO crystal oven is used to generate the femtosecond pulse laser, SHG objective makes the optional compound zoom available, the high NA objective is used to narrow the laser to a very small scale, and the PMT is used as an extremely sensitive detector of SHG and UV signals.

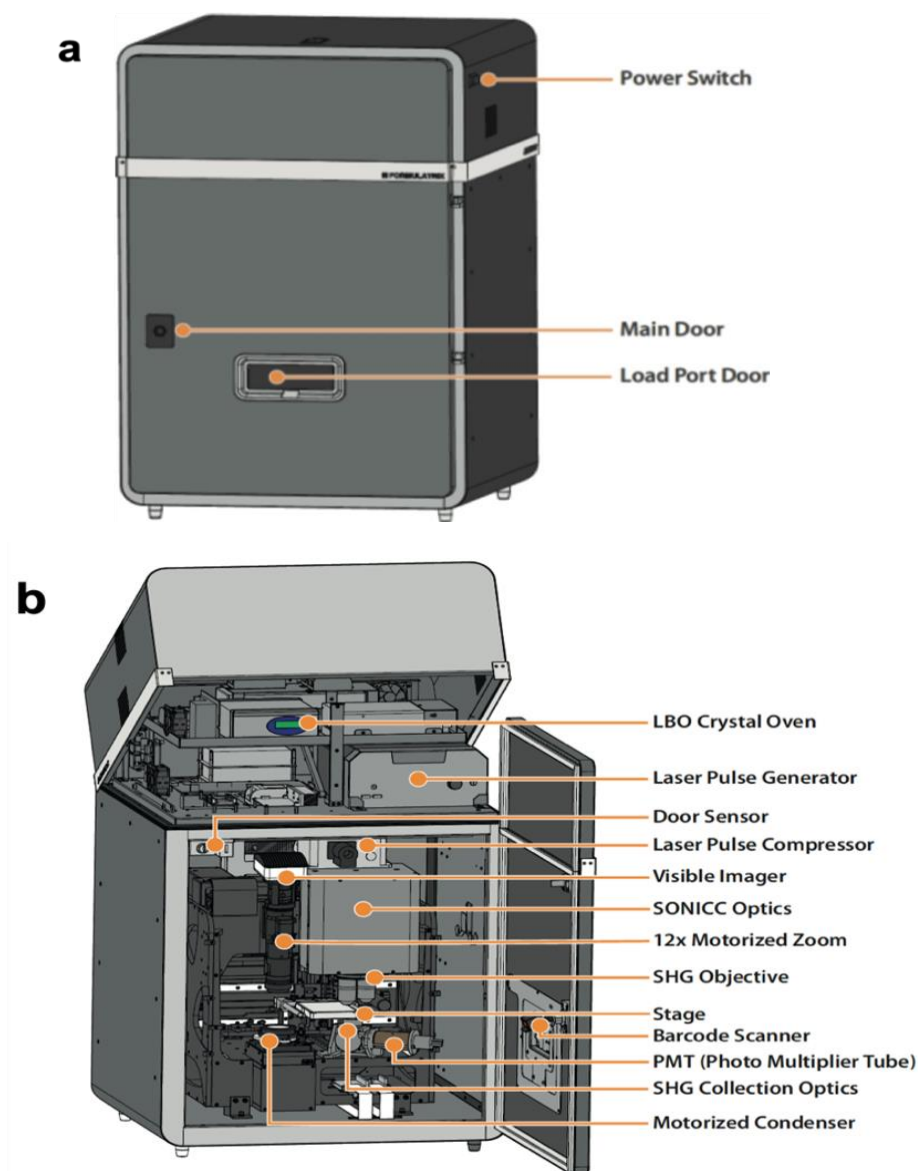


**Fig. 1-19 External and internal views of the Formulatrix SONICC.**  
 (a) External view. (b) Internal view (User's Guide).

The laser of the SONICC system operates with a pulse width of 200 fs and an average power (after the objective lens) of approximately 100 mW to 1 W at an 80 MHz repetition rate. SHG identifies non-centrosymmetric crystals by visualizing the crystal sample with the infrared light (1064 nm) and detecting the frequency-doubled response (532 nm) (Fig. 1-20a). To probe the fluorescence of a protein crystal, the laser wavelength is halved with a nonlinear optical crystal from 1064 nm to 532 nm. The green light (532 nm)

generated is used to obtain the fluorescence of the sample, which can result in the two-photon fluorescence signal from the protein crystal (350-400 nm) (Fig. 1-20b).

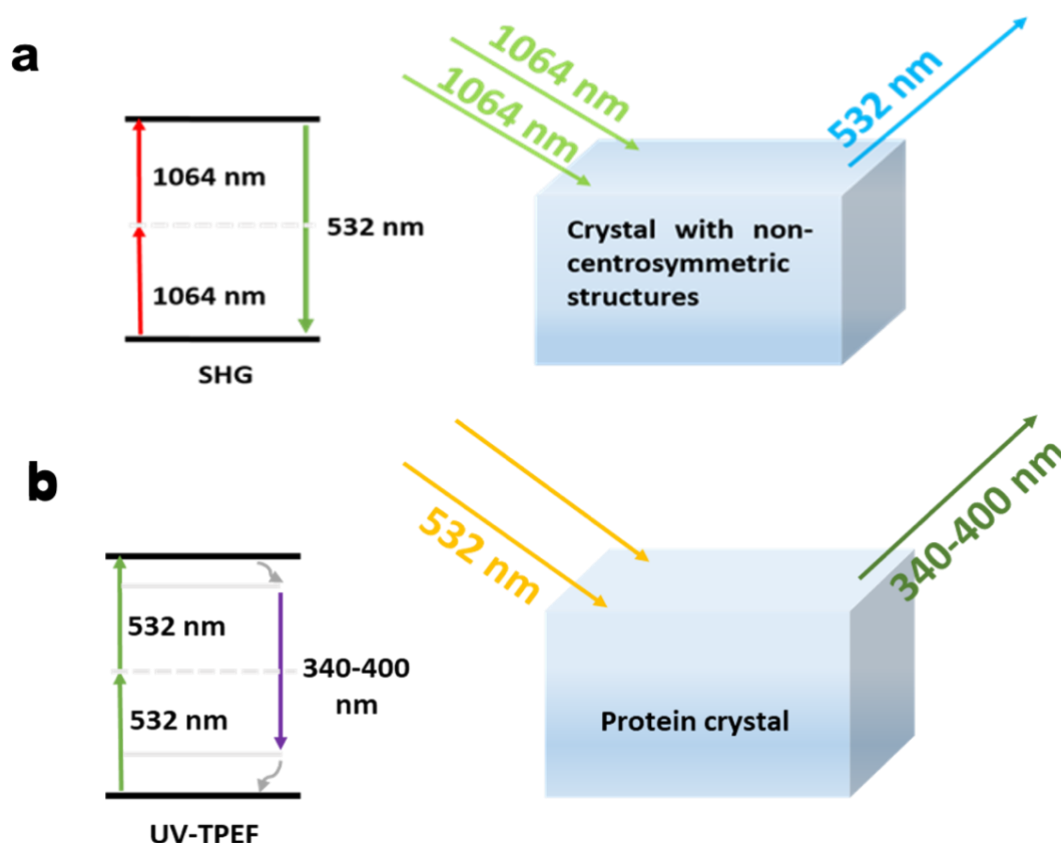


**Fig. 1-20 Schematic representation of SONICC imaging.** (a) Two-photon of green light interacts with a non-centrosymmetric crystal to produce SHG signal. (b) Two-photon of green light interacts with a protein crystal (non-centrosymmetric crystal) to produce two-photon UV signal.

Although the application of SONICC to protein crystal detection is quite encouraging, the imaging technique is still in its infancy. Notably, researchers have found that the SHG response increases with an increase in the size of the crystallite (Lisinski *et al.*, 2010). The SHG intensity varies with the distance travelled in the crystal length  $L$  with a period of  $L=2\pi/\Delta k$  where the  $\Delta k$  is the

phase mismatch factor. Half of this distance is called the coherence length  $L_c$ , at which the SHG intensity reaches a maximum from the crystal entrance to the focus point. Therefore, the generated second-harmonic intensity depends on the crystal size. In addition, the SHG intensity is also related to the square of the second-order nonlinear optical susceptibility, which in turn depends on the space groups of crystals (Kissick *et al.*, 2011).

In crystallography, space groups represent a description of the symmetry of the crystal. The space groups are derived from combinations of the 32 crystallographic point groups with the 14 Bravais lattices (triclinic, simple orthorhombic, body centered orthorhombic, face centered orthorhombic, base centered rhombic, simple monoclinic, centered monoclinic, trigonal, simple tetragonal, centered tetragonal, simple cubic, body centered cubic, face centered cubic, and hexagonal), each of the lattices belongs to one of the 7 crystal systems (tetragonal, orthorhombic, monoclinic, triclinic, trigonal, hexagonal, and cubic systems). The combination of all these symmetry operations results in 230 different space groups describing all possible crystal symmetries.

Although the protein crystal with a non-centrosymmetric structure can be detected by the SHG imaging in theory (Newman *et al.*, 2015), the effect of crystals with higher space groups should also be considered. To be more specific, protein crystals of lower space groups can generate stronger SHG signals than protein crystals of higher space groups (Xiao *et al.*, 2015). This is because each nonzero element contributes to the measured SHG intensity and protein crystals with high symmetry but lacking sufficient nonzero elements emit weaker SHG signals. Due to the limitation of high symmetry, the SHG activity is disappearing (Kissick *et al.*, 2011; Newman & Simpson 2016).

In other words, additional experiments should be performed to better understand the limitations of SONICC for protein nano- or micro-sized crystal detection. 1) To which extent does the intensity of the SHG signal depend on different space groups of crystals? 2) Is it possible to detect *in vivo* protein crystals?

## 1.7 Objectives of this study

As mentioned in sections 1.4 -1.6, there are various methods used to visualize and identify the presence of nano- or micro-sized protein crystals, including bright-field imaging, TEM, DLS, DDLS, X-ray powder diffraction, UV fluorescence imaging, SHG imaging, and THG imaging. However, the accuracy of the detection results is affected by the limitations of each technique. Thus, the combination of different imaging methods should be taken into consideration.

As a result, a new imaging system is needed to detect nano- or micro-sized protein crystals accurately.

This research focuses on the construction of a new imaging system and the detection and identification of nano- or micro-sized protein crystals according to the following objectives (Fig. 1-21).

1. To prepare salt, *in vitro*, and *in vivo* nano- or micro-sized protein crystals of different space groups.
2. To design and construct the new imaging system.
3. To carry out different testing experiments (bright-field, SONICC, DLS, DDLS, TEM, X-ray powder diffraction).
4. To compare the imaging results from conventional imaging and new imaging systems.
5. To identify and characterize salt, *in vitro*, and *in vivo* nano- or micro-sized protein crystals.

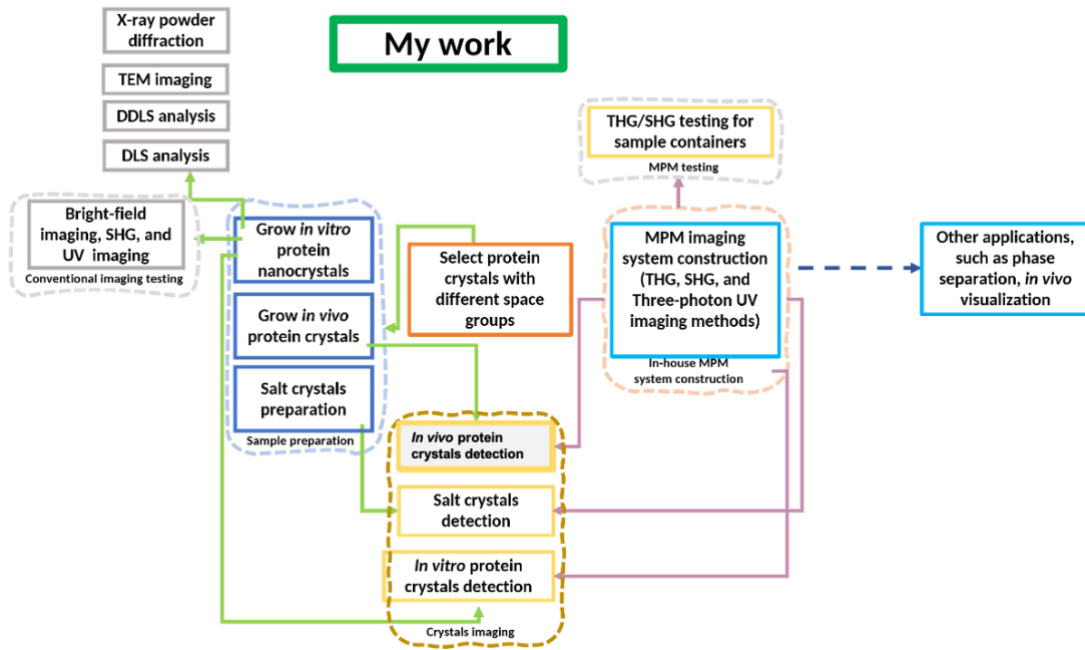


Fig. 1- 21 Flow chart of the experimental work carried out in this thesis.

## 2 Materials and methods

### 2.1 Proteins, chemicals, and reagents

Eight proteins were used for *in vitro* protein crystallization, including lysozyme, proteinase K, thaumatin, thermolysin, glucose isomerase, bovine serum albumin, insulin and lactamase. The first seven were purchased from Hampton and Sigma-Aldrich, and the last one was purified in house. The proteins used in this work are shown in Table 2-1. Moreover, the chemicals and reagents used in this work are provided in Table 2-2.

**Table 2-1** List of proteins used for crystallization.

Protein	Supplier	Molecular weight (kDa)	Isoelectric point
Lysozyme ( <i>Chicken egg white</i> )	Hampton	14.3	10.7
Proteinase K ( <i>Tritirachium album</i> )	Sigma-Aldrich	28.9	8.9
Thaumatococin ( <i>Thaumatococcus daniellii</i> Bennett)	Sigma-Aldrich	22.0	11
Thermolysin ( <i>Geobacillus Stearothermophilus</i> )	Sigma-Aldrich	34.6	5
Glucose Isomerase ( <i>Streptomyces murinus</i> )	Hampton	173.0	4.3
Bovine Serum Albumin ( <i>Bovine serum</i> )	Sigma-Aldrich	66.46	4.5-5.0
Insulin ( <i>Bovine pancreas</i> )	Sigma-Aldrich	5.8	5.3
Lactamase ( <i>Penicillin</i> )	--	29	8.7

**Table 2-2** List of chemicals and reagents used in this work.

Chemicals and Reagents	Chemical Formula	Supplier
Acetic acid	CH <sub>3</sub> COOH	Chem-solute
Ammonium chloride	NH <sub>4</sub> Cl	Sigma-Aldrich
Ammonium sulfate	(NH <sub>4</sub> ) <sub>2</sub> SO <sub>4</sub>	Carl Roth
Bis-tris methane	C <sub>8</sub> H <sub>19</sub> NO <sub>5</sub>	Sigma-Aldrich
Caesium chloride	CsCl	Carl Roth
Calcium chloride	CaCl <sub>2</sub>	Sigma-Aldrich
Calcium acetate	(CH <sub>3</sub> COO) <sub>2</sub> Ca	Sigma-Aldrich
Dulbecco's modified eagle medium (DMEM)	--	Sigma-Aldrich
Dimethyl sulfoxide (DMSO)	C <sub>2</sub> H <sub>6</sub> OS	Sigma-Aldrich
Ethylenediaminetetraacetic acid (EDTA)	C <sub>10</sub> H <sub>16</sub> N <sub>2</sub> O <sub>8</sub>	Sigma-Aldrich
Potassium chloride	KCl	Carl Roth
Sodium chloride	NaCl	Carl Roth
Sodium hydroxide	NaOH	Sigma-Aldrich
Magnesium chloride	MgCl <sub>2</sub>	Carl Roth
Lithium sulfate	Li <sub>2</sub> SO <sub>4</sub>	Applichem
Sodium sulfate	Na <sub>2</sub> SO <sub>4</sub>	Sigma-Aldrich
Monosodium phosphate	NaH <sub>2</sub> PO <sub>4</sub>	Applichem
Disodium phosphate	Na <sub>2</sub> HPO <sub>4</sub>	Applichem
Sodium nitrate	NaNO <sub>3</sub>	Sigma-Aldrich
Sodium acetate	CH <sub>3</sub> COONa	Sigma-Aldrich
Sodium potassium tartrate	NaKC <sub>4</sub> H <sub>4</sub> O <sub>6</sub>	Sigma-Aldrich

Sodium tartrate	$\text{Na}_2\text{C}_4\text{H}_4\text{O}_6$	Applichem
Serum-free medium (EX Cell® 420)	--	Sigma-Aldrich
Fetal bovine serum (FBS)	--	Sigma-Aldrich
4-(2-hydroxyethyl)-1-piperazineethanesulfonic acid (HEPES)	$\text{C}_8\text{H}_{18}\text{N}_2\text{O}_4\text{S}$	Sigma-Aldrich
Phosphate-buffered saline (PBS)	--	Sigma-Aldrich
Polyethylene glycol (PEG) 3350	$\text{H}-(\text{OCH}_2\text{CH}_2)_n-\text{OH}$	Sigma-Aldrich
polyethylene glycol (PEG) 8000	$\text{H}-(\text{OCH}_2\text{CH}_2)_n-\text{OH}$	Sigma-Aldrich
Polyethyleneimine (PEI)	$(\text{C}_2\text{H}_5\text{N})_n$	Sigma-Aldrich
Paraformaldehyde (PFA)	$\text{OH}(\text{CH}_2\text{O})_n\text{H}$ (n = 8 - 100)	Sigma-Aldrich
Penicillin-Streptomycin	--	Sigma-Aldrich
Silicone based elastomeric kit	Sylgard® 184	Dow Corning
Tris(hydroxymethyl)aminomethane (Tris)	$(\text{HOCH}_2)_3\text{CNH}_2$	Fluka

## 2.2 Instruments and consumables

The instruments used in this work are shown in Table 2-3, including those used for DLS and DDLS measurements, transmission electron microscopy (TEM) imaging, X-ray powder diffraction, protein crystallization, salt crystallization, and THG\SHG testing.

Syringes, syringes filters, centrifuge tubes, safe-lock tubes, PTFE Tubing, coverslips, glass slides, LCP (lipidic cubic phase) sandwich plates, and pipette tips have been used in this work. The following Table 2-4 shows an overview of consumables used and the corresponding suppliers.

**Table 2-3** Overview of consumables.

Consumables	Supplier
96-well Swissci MRC-2 plates	Hampton
Centrifuge tubes 15 ml, 50 ml	Merck Millipore
Coverslips 25.4 × 25.4 mm	VWR
Glass slides 76.2 mm x 50.8 mm x 1.2 mm	Paul Marienfeld
LCP sandwich plates	Hampton
Pipette Tips 10 µl, 100 µl, 1000 µl	Millipore
PTFE Tubing, 0.012"ID x 0.030"OD	Cole-Parmer Instrument
Safe-lock tubes 0.5 ml, 1.5 ml, 2 ml	Eppendorf
Syringes 1ml, 5 ml, 10 ml	VWR
Syringe filter 0.22 µm	VWR

**Table 2-4** List of instruments used in this work.

Instrument	Specification	Manufacturer
Balance	CP224S	Sartorius
Centrifuge	5415R	Eppendorf
Crystal plate incubator	RUMED 3001 incubator	Rubarth
DLS instrument	SpectroSize 300	XtalConcepts
DDLs instrument	--	XtalConcepts
Glow discharge system	GloQube	Gloqube® Plus
Microscopes	SZX12 with camera DP10 CLSM	Olympus Zeiss
Erbium-doped fiber laser (EDFL)	--	Home-built
Mixer	ARE-250	Thinky
Magnetic stirring hotplate	MR3001	Heidolph
Objective	XLPLN25XWMP2	Olympus

PH meter	FP20-Std- Bundle	Mettler Toledo
Plasma cleaner	Zepto	Diener electronic
Refrigerated centrifuge	5418R	Eppendorf
Scanning microscope	MPM-2PKIT	Thorlabs
SONICC	Benchtop	Formulatrix ®
Stirrer	MR 3001	Heidolph
Transmission electron Microscopy (TEM)	JEM-2100 Plus	JOEL Ltd.
Vacuum desiccator	Bel-Art 42025	Scienceware ®
X-ray sources	l $\mu$ S	Incoatec.
X-ray detection system	MAR 345	MAR Research

## 2.3 Crystal preparation

### 2.3.1 *In vitro* protein crystal preparation.

Firstly, buffers were prepared using de-ionized water. Buffer pH was measured using a pH-meter and monitored while adjusting (as shown in Table 2-5). All buffers were filtered through a 0.22  $\mu$ m filter prior dissolving proteins and precipitants. To prepare nano- or micro-sized protein crystals for measurement, the sample solution was prepared as described in Table 2-5. Proteins were weighed and dissolved in the appropriate buffer solutions, and then the protein solutions were centrifuged at 8000 rpm for 60 min and filtered through a 0.22  $\mu$ m pore-size filter to obtain homogeneous protein solutions. Meantime, the precipitants were prepared for use. Then, an equal volume of 50  $\mu$ l protein solution was mixed with a 50  $\mu$ l precipitant (the crystallization conditions are illustrated in Table 2-5). The crystallization solution was stored in different containers at room temperature (295 K) for crystallization.

**Table 2-5** Batch crystallization conditions of all investigated proteins with space groups of the resulting crystals.

Protein	Buffer solution	Protein concentration (mg/ml)	Precipitant	Space group
Lysozyme	100 mM sodium acetate, pH 4.5	100	4.5 M sodium chloride, 5% PEG 8000, 0.1 M sodium acetate, pH 4.5	P 4 <sub>3</sub> 2 <sub>1</sub> 2
Proteinase K	20 mM MES-NaOH, pH 6.5	40	1 M sodium nitrate, 0.1 M calcium chloride, 0.1 M MES-NaOH, pH 6.5	P 4 <sub>3</sub> 2 <sub>1</sub> 2
Thaumatococin	50 mM Bis-tris, pH 6.5	30	MES-NaOH, pH 6.5, 2 M sodium tartrate, 50 mM Bis-tris, pH 6.5	P 4 <sub>1</sub> 2 <sub>1</sub> 2
Thermolysin	45% DMSO, 2.5 M caesium chloride, 50 mM Tris, pH 7.0	45	H <sub>2</sub> O	P 6 <sub>1</sub> 2 2
Glucose Isomerase	10 mM HEPES, pH 7.0	30	2 M ammonium sulfate, 50 mM HEPES, pH 7.0	I 2 2 2
Bovine Serum Albumin	0.1 M Tris HCl, pH 6.5	20	0.2 M calcium acetate, 20% PEG 3350, 0.1 M Tris HCl, pH 6.5	C 2
Insulin	50 mM sodium phosphate, 10 mM EDTA, pH 10.0	20	0.5 M sodium phosphate, pH 10.0	I 2 <sub>1</sub> 3
Lactamase	20 mM MES, 50 mM NaCl, pH 4.5	7	25% PEG 8000, 0.2 M Li <sub>2</sub> SO <sub>4</sub> , 0.1 M Na Acetat, pH 4.5	P 3 <sub>2</sub> 2 <sub>1</sub>

### 2.3.2 *In vivo* protein crystal preparation

As a result of the expression of recombinant genes, crystal growth in host cells has been reported in plant cells, chickens, and mammals, as well as baculovirus-infected insect cells. In this work, insect cells and mammalian cells were selected to grow protein crystals as mammalian cells and insect cells can support a more general qualification of this cellular environment to promote intracellular crystal growth.

Sf9 (*Spodoptera frugiperda*) (Expression Systems, 94-001F), a clonal isolate of *Spodoptera frugiperda* Sf21 cells (IPLB-Sf21-AE), are commonly used in insect cell culture for recombinant protein production using baculovirus. Notably, they are established from ovarian tissue and can be grown in the absence of serum and cultured either attached or suspended.

HEK (Human embryonic kidney) 293 cells— often referred to as HEK cells — is a specific cell line derived from human embryonic kidney cells grown in tissue culture. HEK cells have been widely applied in cell biology research for numerous years because of their reliable growth and propensity for transfection. They are also used to produce therapeutic proteins and viruses for gene therapy in the biotechnology industry (He *et al.*, 1998).

Insect cells and mammalian cells were selected to obtain *in vivo* grown protein crystals. Sf9 insect cells and mammalian cells were seeded in a different medium, Sf9 insect cells were seeded in serum-free medium plus 10% Penicillin-Streptomycin, while mammalian cells were seeded in Dulbecco's modified eagle medium (10% Penicillin-Streptomycin + 5% fetal bovine serum). Then they were infected with four corresponding baculovirus constructs, namely P21 serine /threonine kinase 4 (PAK4), PAK4 in complex with green fluorescent protein (PAK4-GFP), PAK4 in complex with its inhibitor Inka1 (PAK4-Inka) and Iosine-5'-monophosphate dehydrogenase (IMPDH). Afterwards, infected Sf9 were incubated at 27°C without additional CO<sub>2</sub> for 3-4 days and mammalian cells were cultured at 37°C with 5% CO<sub>2</sub> for several days. Last, cells were harvested 3-4 days after transfection and inactivated by a mild fixation with freshly prepared 4% paraformaldehyde (PFA), followed by

several PBS-washing and centrifugation steps to remove unbound PFA and stored in 1 × PBS at 4°C for use.

### **2.3.3 Salt crystal preparation**

In the experiment, since not all the selected salt crystals exhibit centrosymmetric, the SHG responses could be observed for non-centrosymmetric structures. As a result, common salts that are regularly used as precipitants in protein crystallization were selected.

The salt crystal preparation process is as follows:

1. Completely dissolving the salt in a beaker containing 1 ml distilled water
2. Removing the saturated salt solution from the breaker, pipetting the saturated salt solution into the sample contains.
3. Then, putting the sample containers (with a saturated salt solution) from step 2 in the fridge and storing overnight at 4 degrees.
4. Checking the sample using a normal optical microscope.

## **2.4 DLS and DDLS measurements**

For lysozyme, thaumatin, and proteinase K crystallization processes were recorded using a DDLS instrument, which can perform DLS and DDLS measurements. The laser has an output power of 100 mW and a wavelength of 532 nm. The refractive index of water was used for all calculations as all sample solutions were aqueous.

Prior to performing DLS and DDLS measurements, samples were centrifuged at 8000 rpm for at least 10 min. To determine the initial hydrodynamic radius of the investigated protein, 20 µl of the protein solution was pipetted into the DDLS cuvette. All solutions were prepared using ultrapure water and filtered through a 0.22 µm filter. Protein crystallization was achieved by the addition of the corresponding precipitant (Table 2-4). Samples were measured at room temperature and each measurement was performed for 20 s with a waiting time at 10-s intervals. The XtalConcepts software was used for recording the real-time DLS and DDLS measurements automatically. The hydrodynamic

radii were calculated by the XtalConcepts software from the decay time constant of the auto-correlation function.

## **2.5 TEM imaging**

The transmission electron microscopy (TEM) images of the three proteins crystals were performed at the European XFEL with the assistance of Dr. Robin Schubert. Three copper grids with carbon film were negative-discharged for 30 seconds at 25 mV in a glow discharge system. Then, the three copper grids were washed twice with 10  $\mu$ l water and stained with 5  $\mu$ l uranyl acetate for 30 seconds. Afterward, 4-5  $\mu$ l of nano- or micro-sized lysozyme, thaumatin, and proteinase K crystal samples were respectively incubated on the copper grids for 30 seconds. Grids were mounted on a specimen plate of a single-tilt holder and inserted into a microscope operating at 120 kV. Using the FEI T12 user interface program, images were obtained using the auto-exposure and low dose mode. The focus of the images was adjusted by minimal contrast and live fast Fourier transform (FFT). The images were defocused by  $-500$  to  $-1500$  nm in order to obtain more distinct lattice fringes. TEM images of three proteins crystals were collected on a CCD camera (Gatan, Inc. USA). Besides, FFT images of the selected nanocrystal lattice region were generated using the Digital Micrograph software (Gatan, Inc. USA).

## **2.6 X-ray powder diffraction**

The TEM samples were also analyzed by X-ray powder diffraction to analyze and verify crystallinity. 20  $\mu$ l of each sample suspension was pipetted into a quartz capillary with a diameter of 0.3  $\mu$ m and the sample was compacted by centrifugation (2000 rpm, 20 min). After cutting the capillaries with an appropriate length, they were sealed with wax. Diffraction images were recorded after mounting the capillary onto a 3-axis goniometer and aligning the sample pellet in the X-ray beam. A MAR 345 image plate detector in combination with an X-ray source was used to record a powder diffraction pattern at room temperature. Each sample was exposed to X-rays for 20 min

and oscillated for 2 degrees during the exposure. The distance of the sample to the detector was 250 mm.

## **2.7 Sample preparation in different sample containers**

### **2.7.1 Conventional sample container**

As the ideal sample container for SONICC imaging, the LCP sandwich plate (as shown in Fig. 2-1a) consists of a glass base, a 140  $\mu\text{m}$  double sticky spacer with 96 holes punched out, and a brown liner. The model representation in Fig 2-1b shows that the double sticky spacer adheres to the base plate, and the brown paper liner covers and protects the top of the double sticky spacer and base plate. After loading the sample into each of the wells on the base plate, the base plate with samples was covered and sealed by a 0.2 mm thick glass coverslip.

The protocol for loading the sample is as follows:

1. Removing the dust particles from the LCP sandwich plate by using duster-canned air.
2. Carefully removing the brown liner from the base plate.
3. Pipetting samples into each of the wells on the base plate.
4. Removing dust particles from the 0.2 mm thick glass coverslip by using duster-canned air.
5. Carefully aligning the glass coverslip with the base plate and then lowering the glass coverslip onto the base plate. Gently and carefully pressing the cover glass in the areas where the adhesive is located to seal the plate.

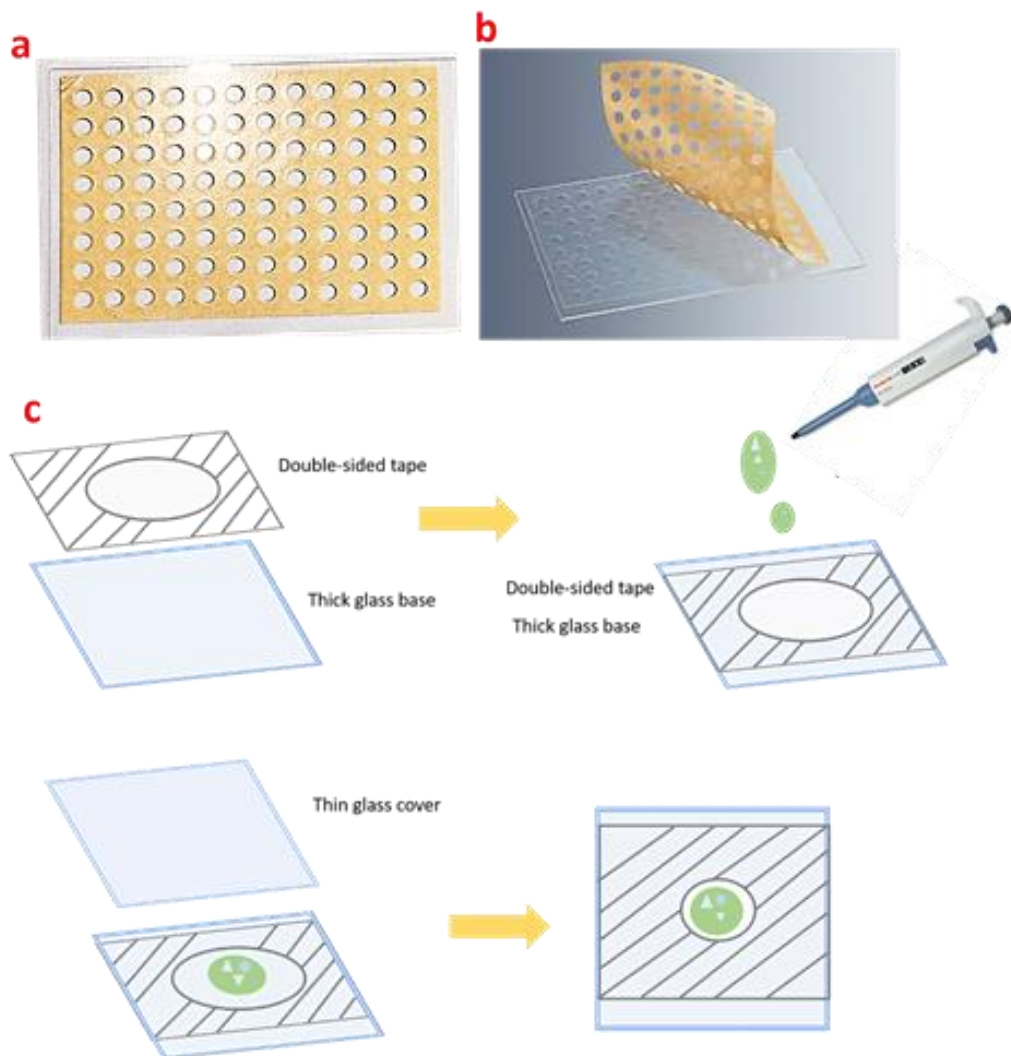


**Fig. 2-1 Sample preparation using the LCP sandwich plate.**

(a) LCP sandwich plate with a brown cover. (b) Removing the brown liner from the base plate. (c) Sample preparation in the unit of the LCP sandwich plate.

### 2.7.2 Polydimethylsiloxan (PDMS) microfluidic chip

The PDMS microfluidic chip is a set of micro-channels molded into PDMS. In protein crystallography, the PDMS microfluidic chip is widely used to set up crystallization experiments and can be used to perform *in situ* X-ray diffraction data collection. In this section, the manufacturing process of the PDMS microfluidic chip is described.

In Fig. 2-2, the manufacturing process of the PDMS microfluidic chip is illustrated. The microfluidic chip was manufactured via a master mold. The master mold used in this work is a silicon wafer with micro-channels of precise dimensions. As demonstrated in Fig. 2-2b, the silicon wafer is imprinted with the positive features of the microfluidic chip by using photolithography. Then, PDMS was poured onto the silicon wafer and the PDMS was peeled from the silicon wafer after the PDMS hardened. Finally, the dust was cleaned from the PDMS and the glass slide to stick the PDMS chip to the glass slide.

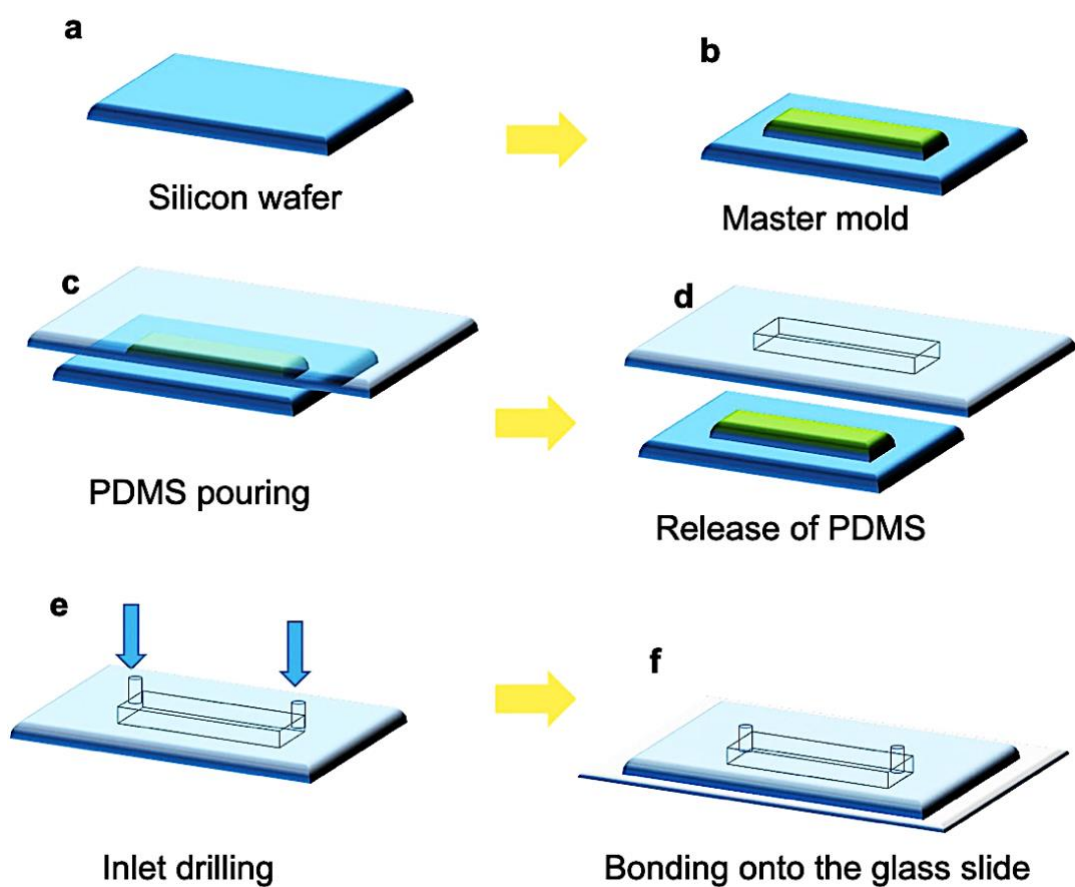


**Fig. 2-2 Scheme of the PDMS chip fabrication.**

(a) Silicon wafer without channels. (b) The silicon wafer is imprinted with the positive features of the microfluidic chip by using photolithography. (c) PDMS is poured on the wafer. (d) The dried PDMS is peeled off from the wafer. (e) The inputs and outputs of the microfluidic chip are punched with a puncher with the size of the future connection tubes. (f) The PDMS is bonded onto the glass slide.

Details of the manufacturing process of the PDMS microfluidic chip are described as follows:

1. PDMS, consisting of a mixture of silicone base with 10 % (w/w) curing agent, is thoroughly mixed by a mixing machine at 2000 r/min for 2 min, and ready for further use.
2. Placing the PDMS into the vacuum desiccator to remove air bubbles (Fig. 2-3c).
3. A 90 mm petri dish is wrapped with aluminum foil (carefully attached the aluminum foil around the petri dish) to ensure that the bottom of the aluminum foil is perfectly flat.
4. The wafer (Fig. 2-3b) is then positioned into a petri dish, and 20 g of PDMS without air bubbles (PDMS from the second step) is carefully pouring onto the wafer.
5. Then, the PDMS is cured in the oven for one hour at 70 °C and subsequently peels from the silicon wafer master mold (Fig. 2-3d).
6. The inlet/outlet is punched by a puncher, allowing the injection of fluids.
7. The glass slide and PDMS are treated with plasma cleaner to remove particles (Fig. 2-3e). Then, the microfluidic channels in the PDMS structure are carefully orientated to be parallel to the edges of the glass slide and both are shortly pressed together for bonding using the metal weight for 1 hour (Fig. 2-3f).
8. Finally, the glass slide with the PDMS is heated in a 70°C oven for 1 h to ensure the glass slide is tightly adhered.

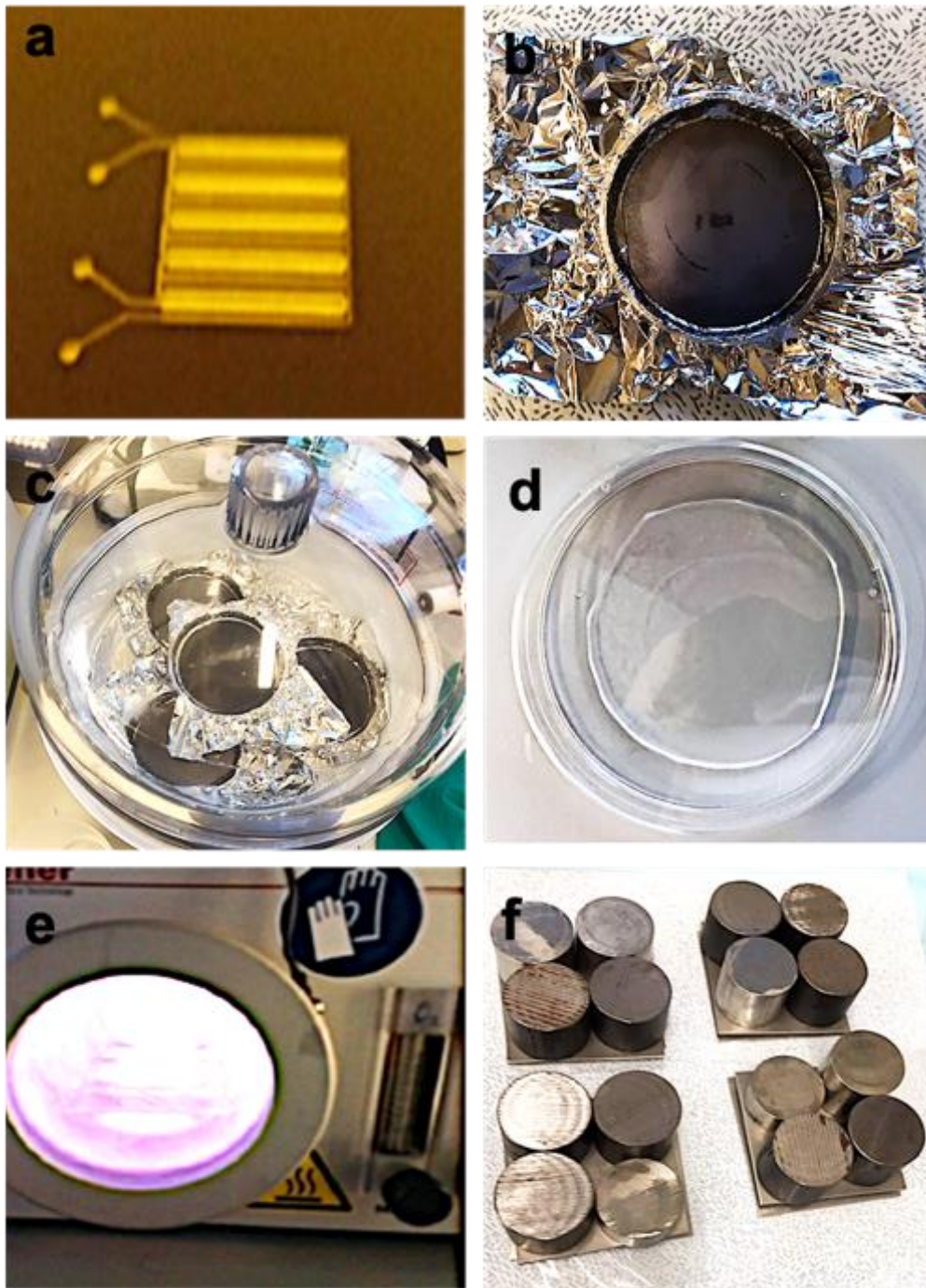


**Fig. 2-3 PDMS microfluidic chip preparation.**

(a) Silicone wafer. (b) Silicone base with 10 wt% curing agent is poured onto the wafer. (c) Air bubbles are removed with a vacuum desiccator. (d) After curing for 1 hour at 70 °C, the PDMS cast is removed from the master. (e) PDMS and a glass slide are exposed to O<sub>2</sub> plasma for removing dust. (f) Bonding PDMS mold and the glass slide using the metal weight.

The schematic diagram of the PDMS microfluidic chip used in this work is shown in Fig. 2-4, and the photographic image of the PDMS microfluidic chip is shown in Fig. 2-5.

The PDMS microfluidic chip consists of main channels, crystallization wells, capillary valves, and side channels. The crystallization solution was injected through the tubing connected with a wider main channel. After inserting the solution into the the PDMS chip, the air mixing in the wells escaped through the capillary valves and the side channel, and the solution was left in the crystallization wells. There were ten main channels marked by A–J, and each row of crystallization wells was labelled by the numbers 0–41. Thus, 410 crystallization wells could be used to incubate and store protein crystals.

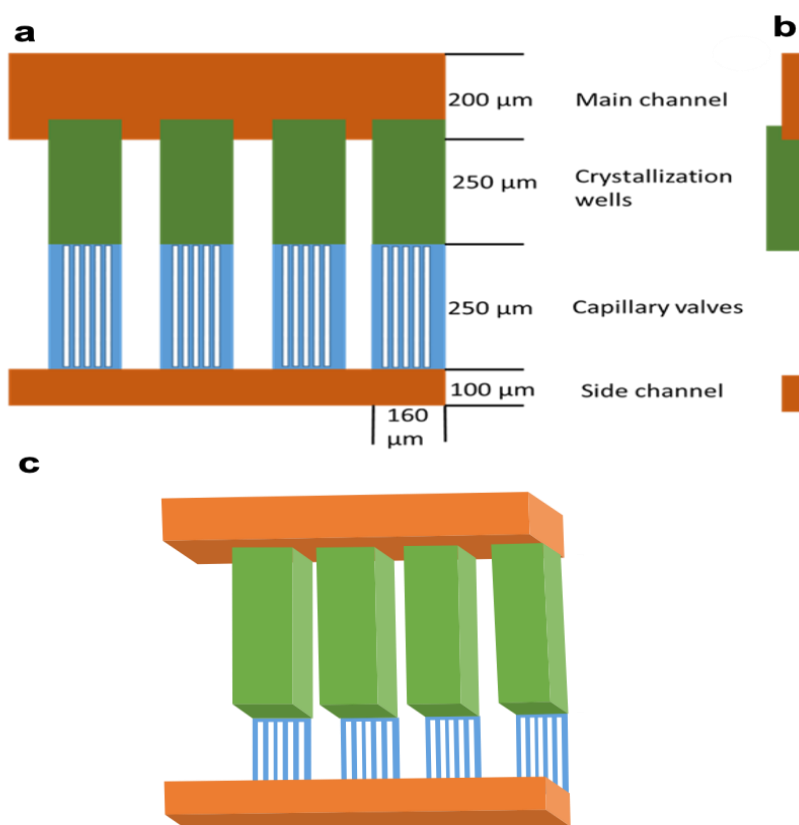


**Fig. 2-4 Scheme of the PDMS microfluidic chip.**

(a) Top view. (b) Side view. (c) Parallel view. Typical channel heights were: 50 μm bypass, 50-60 μm crystallization well, 5-10 μm capillary valve, corresponding to well volumes of about 2.5 nL .

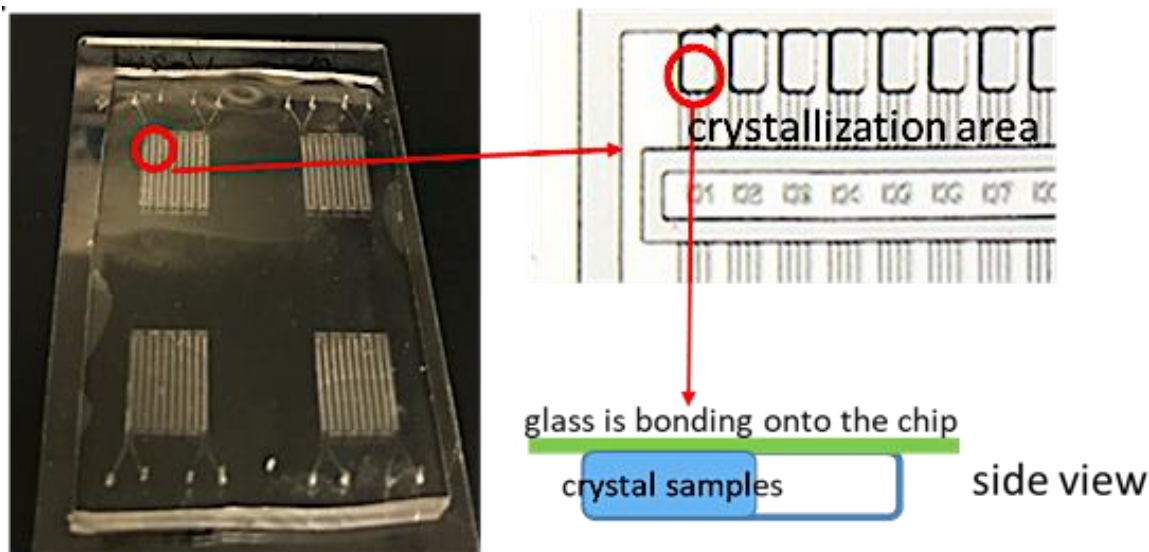


**Fig. 2-5 Sample preparation in the PDMS microfluidic chip.** The crystal sample is loaded through the access holes using a tubing with a diameter matching the access holes for optimal sealing.

### 2.7.3 The 96-well 2-drop MRC crystallization plate (MRC-2 plate)

The Swissci 96-well 2-drop MRC crystallization plate contains 96 units, each of which is constituted by two crystallization wells and one reservoir well (40-100  $\mu$ l of each reservoir well and 50 nl-5  $\mu$ l of each crystallization well). The micro-numbering labels alongside drop volumes are easily visible by microscope. The crystals can be observed in UV, polarized, and visible light, as the plate is molded from a UVXPO polymer.

The crystal sample can be loaded into the plate by a crystallization robot or pipette. 2  $\mu$ l of the mixed solution was then dispensed into each of the 96 wells of the crystallization plate by a pipette. Notably, the time disparity of dispensing each two crystallization wells was approximately 3-4 s in the same row through manual pipetting. Fig. 2-6 shows that the crystal sample is stored in the crystallization well, and subsequently sealed with tape.

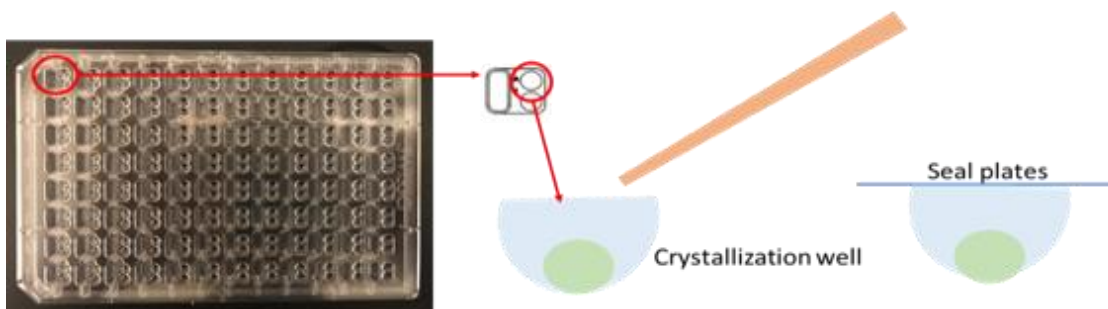


**Fig. 2-6 Sample preparation in the MRC-2 plate.**

The MRC-2 well crystallization plate contains a 2-drop chamber, 96 well crystallization plate for sitting drop vapor diffusion.

## 2.8 THG/SHG imaging

The thaumatin and lysozyme protein crystals were incubated and stored in the LCP sandwich plates, PDMS microfluidic chips and 96-well MRC-2 plates, respectively. THG and SHG signals were detected by using the MPM instrument.

The procedure of THG/SHG detection applying by MPM imaging instrument was as follows:

1. Loading different sample containers.
2. Turning to the imager menu, and inspecting the crystallization drops with THG imaging.
3. Imaging a specific drop with crystals: pointing to an image on the imager menu, and clicking interesting drop(s) to use the default imaging setting.
4. SHG imaging: clicking the SHG imaging mode to perform SHG imaging with the default imaging setting, and then scanning drops by setting focus manually.

## 2.9 Angular-dependent SHG polarization intensity

Protein crystals (lysozyme and glucose isomerase) from two different space groups were selected, and their micro- or nano-sized crystals were prepared

according to Table 2-5. Proteins were dissolved in appropriate buffer solutions and filtered along with precipitation solutions through 0.22  $\mu\text{m}$  filters, and then centrifuged at 8000 rpm for 60 min. After mixing the protein and precipitant at the same volume ratio (1:1), they were injected into PDMS microfluidic chips. The polarization dependence of glucose isomerase and thaumatin micro-sized crystals was examined from 0 to 90 degrees, with measurements taken at 10-degree intervals. To further study the relationship between the SHG response and angular change, the SHG signal intensities with polarization angle changes were simply calculated.

## **2.10 Imaging protein crystal applying the Formulatrix SONICC and the MPM imaging systems**

The SONICC instrument (bright-field, SHG, and 2-photon UV imaging methods) and the MPM imaging system (THG, SHG, and 3-photon UV imaging methods) were used for the imaging of different protein crystals of the distinguished space groups. A large lysozyme crystal, micro-sized lysozyme crystals, micro-sized proteinase K crystals, micro-sized thaumatin crystals, and micro-sized thermolysin crystals were detected applying the SONICC and the MPM systems. The *In vivo* grown protein crystal of PAK4, *in vivo* grown protein crystal of PAK4-GFP, and *in vivo* grown protein crystal of IMPDH were detected applying the MPM system.

The procedure of detection applying the Formulatrix SONICC instrument was as follows:

1. Loading the protein crystallization plate: clicking the imaging menu and selecting the load crystallization plate, and then placing the crystallization plate on the imaging hand.
2. Selecting the crystallization plate type: turning to the imaging menu, clicking plate using, and selecting the crystallization plate type according to the measurement.
3. Inspecting the entire crystallization drops with the default imaging settings to select the drops that contain crystals: pointing to an image

on the imaging menu, clicking drop, moving to the live imaging tab, and scanning the drops manually.

4. Magnifying the selected image through choosing the drop-down list.
5. Imaging a specific drop with crystals: turning to image on the imaging menu and clicking interesting drop(s) to use the default imaging setting.
6. SHG imaging: clicking the SHG imaging mode to perform SHG imaging applying the default imaging setting, and then scanning drops by setting focus manually.
7. UV imaging: changing the SHG imaging mode to the UV imaging mode, and then scanning drops by setting focus manually.

The images of crystal applying the SONICC system were acquired and processed by the Rock Maker software.

The procedure of detection applying the MPM imaging instrument was as follows:

1. Loading the PDMS chip.
2. Turning to the imaging menu, and inspecting the crystallization drops with the THG imaging.
3. Adjusting the miniature platform to allow XYZ positioning of crystals.
4. Imaging a specific drop with crystals: pointing to image on the imaging menu, and clicking interesting drop(s) to use the default imaging setting.
5. SHG imaging: clicking the SHG imaging mode to perform SHG imaging applying the default imaging setting, and then scanning drops by setting focus manually.
6. UV imaging: changing the optical filter to perform UV imaging, and then scanning drops by setting focus manually.

The images applying the MPM system were acquired and processed by the ThorImageLS software suite, and the software took a few seconds (3-5 s) to capture an image with 1024x1024 pixels.

## **2.11 Imaging of salt crystal applying the MPM imaging system**

The salt crystals were incubated and stored in the PDMS microfluidic plates; SHG signals were captured by the MPM system. The procedure of detection applying the MPM imaging system instrument was as follows:

1. Loading the PDMS chip.
2. Turning to the imaging menu, and inspecting the crystallization drops with the THG imaging.
3. Imaging a specific drop with crystals: pointing to image on the imaging menu, and clicking interesting drop(s) to use the default imaging setting.
4. SHG imaging: clicking the SHG imaging mode to perform SHG imaging applying the default imaging setting, and then scanning drops by setting focus manually.
5. UV imaging: changing the optic filter to perform UV imaging, and then scanning drops by setting focus manually.

## **3. Design and construction of the MPM system**

### **3.1 Design and construction**

#### **3.1.1 Nonlinear optical imaging methods selection**

In this work, the following requirements for choosing different imaging methods were taken into consideration: 1) Trying to select a cost-effective method to build a detection system; 2) Trying to prevent or reduce damage in the process of sample preparation to ensure the usability of the sample for diffraction experiments following optical detection; 3) Trying to identify nano- or micro-sized protein crystals and distinguish protein crystals from salt crystals. Thus, non-invasive, label-free nonlinear optical imaging methods are preferred except for those imaging methods requiring extensive sample preparation (TEM, X-ray powder diffraction).

As shown in Table 3-1, the advantages and disadvantages of different nonlinear optical imaging methods are presented below. For protein crystals detection, the first step is to locate and scan the sample. THG is a good choice as this imaging method is not limited to the non-centrosymmetric structures but relies on optical inhomogeneity within the excitation region. In other words, the THG imaging can detect both non-centrosymmetric and centrosymmetric media, thereby providing high contrast at the interface between the crystal and solution and revealing the morphology of crystals. Then the SHG is applied to the identification of non-centrosymmetric crystals, as most protein crystals and salt crystals are naturally colorless and transparent and cannot be distinguished by the THG imaging method. Furthermore, UV fluorescence imaging can be employed to further distinguish protein crystals from salt crystals. Besides, SHG and UV imaging can be combined to produce an overlapping signal that can confirm protein crystals. The detection process can be seen in Fig. 3-1.

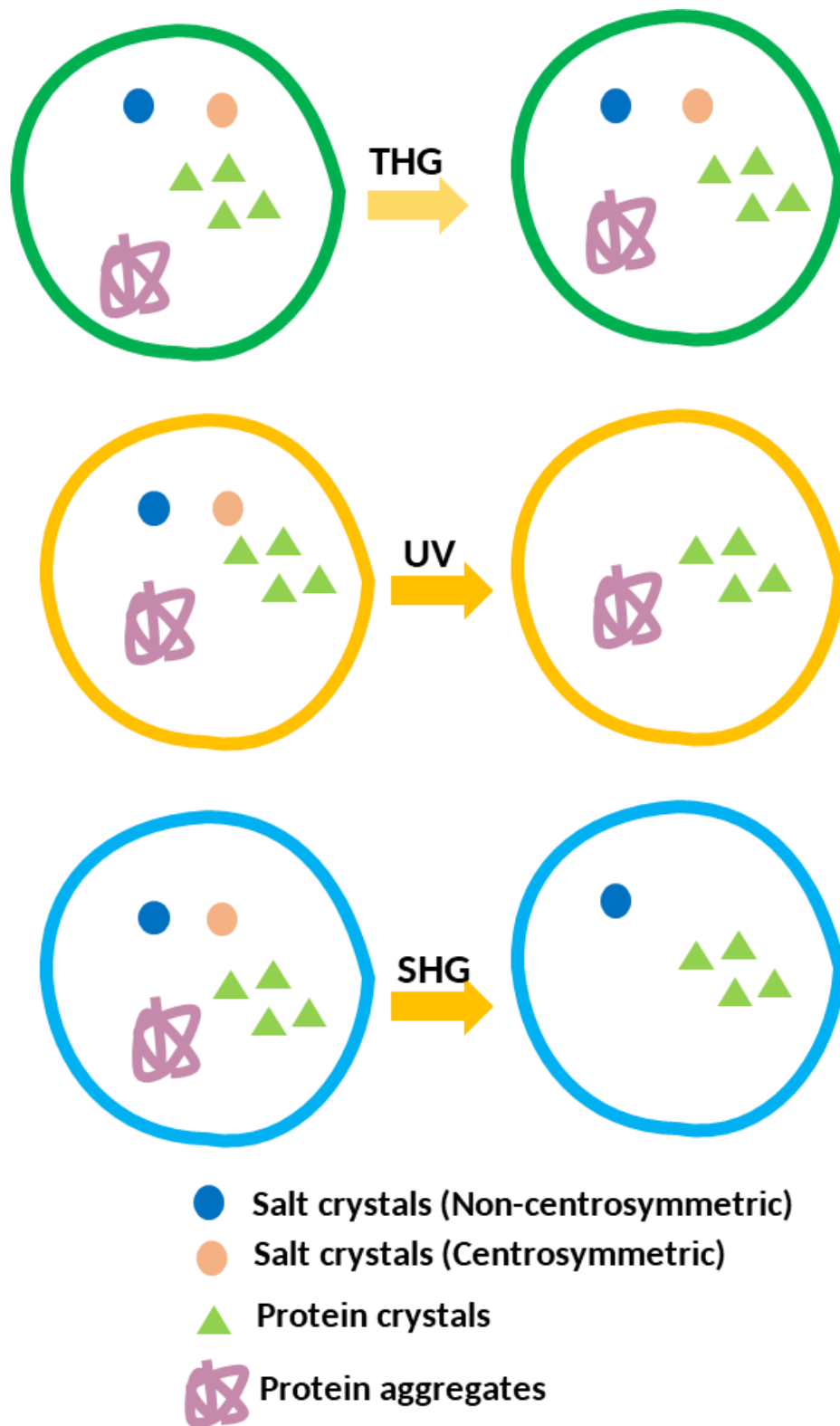


Fig. 3-1 Detection workflow using the multiphoton imaging system.

**Table 3-1** Comparison of different imaging methods.

Imaging methods	Applications	Advantages	Limitations
Bright-field	Sample with dimensions of approx. 0.1 mm and higher can be detected.	Easy to detect sample with an intrinsic color.	Nano- or micro-sized protein crystals that are naturally colorless and transparent mostly cannot be detected; Protein crystals and salt crystals cannot be distinguished.
THG	Morphogenesis, lipids in cells, collagen bundles, muscle fibers, and crystals imaging.	Label-free; Non-invasive; No requirement of a specific asymmetric structure.	Protein and salt crystals cannot be distinguished; False positive may from phase separation and amorphous aggregates.
SHG	Visualization of biological samples containing non-centrosymmetric unit;	Label-free; Non-invasive.	Protein crystals and salt crystals exhibit non-centrosymmetry cannot be distinguished
UV	Fluorescent proteins can support the localization of proteins, as well as the protein crystals.	Label-free; Non-invasive.	False positive from protein dense phase and protein aggregation.

In order to achieve various nonlinear optical imaging results for simultaneous image acquisition, a multimodal configuration incorporated in a single scanning microscope was employed. This combination of techniques is robust and popular as the same excitation laser source can be used for both imaging methods. An ultrafast pulsed laser is applicable to these nonlinear optical imaging methods (SHG, THG, UV), each of which requires a specific excitation and detection scheme shown in Table 3-2 that includes important optical parameters for each of these nonlinear optical imaging modalities.

Notably, the information can be learnt from Table 3-2 that a longer wavelength (i.e., >1200 nm for THG, and >750 nm for SHG) is required to perform SHG and THG. For UV wavelength selection, intrinsic AAAs (Tyr, Trp, Phe) in most protein crystals emit fluorescence at ~350 nm wavelength as a result of a 280 nm excitation through one-photon absorption. However, one-photon UV excitation may induce photochemical damage and thus multi-photon UV excitation is an alternative to detect protein crystals. Notably, since 3PEUVF can increase penetration depth and present higher resolution than 2PEUVF, the 3PEUVF was selected to detect protein crystals.

**Table 3-2** Optical parameters for different nonlinear optical imaging modalities.

Nonlinear optical imaging	Input	Output	Incident wavelength range (nm)	Typical excitation source	Detection scheme	Ref.
TPEF	$\omega$	$\omega < \omega' < 2\omega$	500-1140	Femtosecond laser	PMT	Denk <i>et al.</i> , 1990; Drobizhev <i>et al.</i> , 2011
3PEF	$\omega$	$\omega < \omega' < 3\omega$	750-1140	Femtosecond laser	PMT	Hell <i>et al.</i> , 1996
THG	$\omega$	$\omega' = 3\omega$	800-1550	Femtosecond laser	PMT	Müller <i>et al.</i> , 1998; Barad <i>et al.</i> , 1997
SHG	$\omega$	$\omega' = 2\omega$	500-1300	Femtosecond laser	PMT	Franken <i>et al.</i> , 1961; Gannaway & Sheppard 1978

### 3.1.2 Selection of laser sources

A number of ultrafast laser sources (e.g. Ti:sapphire laser, Cr:forsterite laser, and Er:fiber laser) have been developed and applied to different nonlinear optics imaging (Fig 3-2). These sources normally produce femtosecond pulses at different center wavelengths depending on the media.

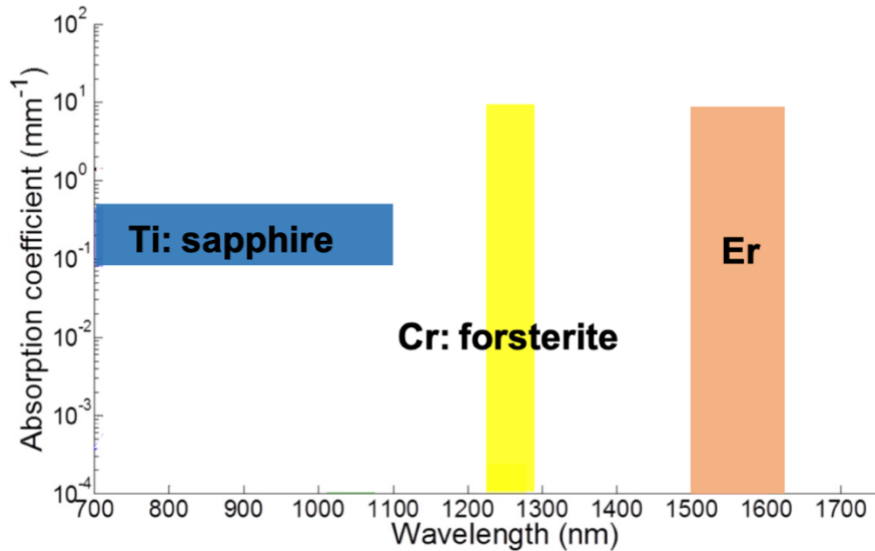


**Fig. 3-2 Optical wavelength coverage of common ultrafast lasers.**

The Ti:sapphire laser has the highest efficiency at ~800 nm with the wavelength ranging from 700 nm to 1100 nm, as shown in Fig. 3-2. Both 2PEF and SHG imaging can be performed by applying the laser source (Moulton, 1986; Erny & Hauri 2013).

The Cr:forsterite laser, which has its center wavelength at ~1250 nm with the direct emission from 1100 nm to 1350 nm, is an ideal source to drive high generation imaging. The application of Cr:forsterite lasers result in achievable SHG and THG, which benefit from less optical attenuation in the biological tissue (Chung *et al.*, 2018).

The Er-doped fiber laser (EDFL) has a center wavelength between 1530 nm and 1610 nm. Despite its availability for performing THG imaging, this laser

source is not commonly adopted due to the higher water absorption at this wavelength range (Liu *et al.*, 2017; Chung *et al.*, 2019a).

In principle, the 775-nm beam can excite SHG and 3PEUVF for protein crystal detection, being obtainable by implementing frequency doubling from 1550 driven by the EDFL laser. Besides, the excitation wavelengths around 1200-1300 nm for THG imaging (the attenuation was found to reach a minimum value around 1200-1300 nm) can be achieved by a self-phase modulation enabled spectral selection (SESS) source based on the EDFL laser (Chung *et al.*, 2018). Thus, an EDFL source was selected and used to achieve THG, SHG, and 3PUVF imaging.

In this work, the MPM system is comprised of two parts: a laser source and a scanning microscope. Fig. 3-3 and Fig. 3-4 show the schematic and photographic system. Two nonlinear wavelength converters were introduced (self-phase modulation enabled spectral selection and frequency doubling) to achieve two different excitation wavelengths: 1300 nm and 775 nm, which were used for THG/SHG imaging and SHG/3PEUVF imaging, respectively.

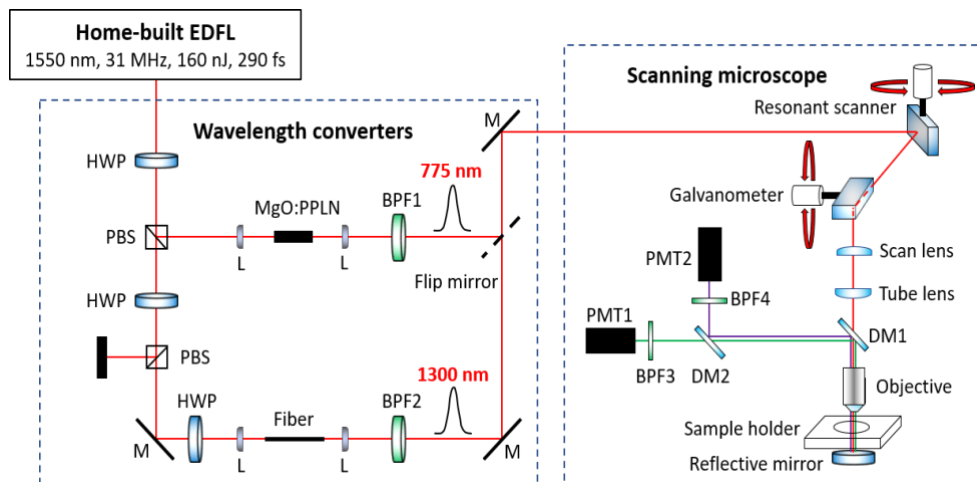


**Fig. 3-3 Scheme of the MPM system** (laser part and scanning microscope). This is made up of - HWP: half-wave plate; PBS: polarization beamsplitter; L: lens, M: mirror; MgO:PPLN: magnesium-doped periodically poled lithium niobite; DM: dichroic mirror; BPF: bandpass filter; and PMT: photomultiplier tube.

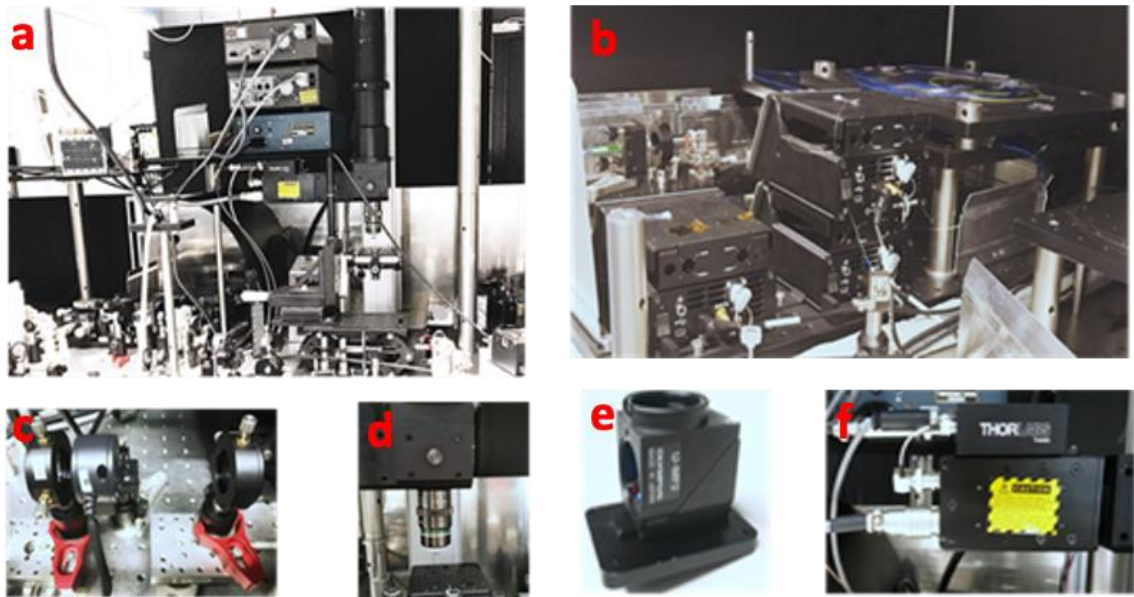


**Fig. 3-4 Photographic image of the MPM instrument.**

(a) MPM system. (b) Er-fiber chirped-pulse amplification (CPA) laser system. (c) MgO:PPLN. (d) Microscope system. (e) Dichroic mirror and bandpass filter. (f) Photomultiplier tube.

### 3.1.3 Construction

Firstly, a 31 MHz EDFL laser system was constructed by the group of Prof. Kärtner in CFEL. The laser system generated 290-fs pulses centered at 1550 nm with  $\sim 5$ W average output power (shown in Fig. 3-5). The development of high-power and high-pulse-energy ultrafast EDFLs is mainly confronted with one challenge: fiber nonlinearity. The issue that nonlinearity might distort the pulse while amplification can be solved by chirped-pulse amplification (CPA). The amplified 200-nJ pulses were described by a transmission diffraction-grating pair with 966.2-lines/mm groove density. The grating pair was set in a double-pass configuration with 80% transmission efficiency.

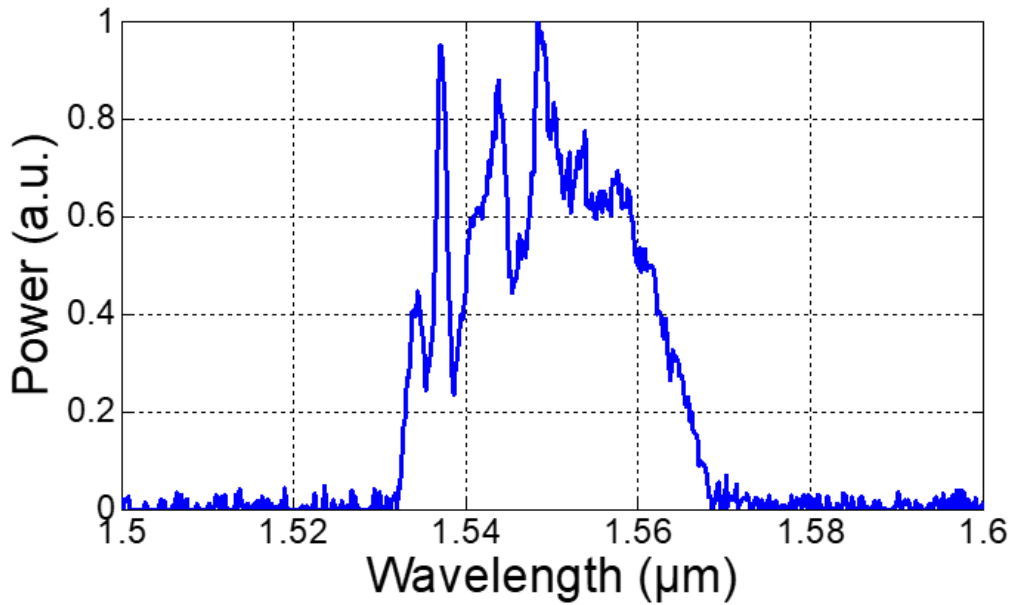


**Fig. 3-5 Simulation result of a 290-fs pulse propagating in an optical fiber.** Filtered spectrum entered at 1550 nm.

To achieve a 1300 nm beam for THG imaging, the self-phase modulation enabled spectral selection (SESS) method was adopted. Self-phase modulation (SPM) is a nonlinear optical effect of light-matter interaction. An ultrashort pulse of light, when travelling in a medium, can induce a varying refractive index of the medium. This variation in refractive index will generate a phase shift in the pulse, causing a change in the pulse's frequency spectrum. Self-phase modulation has crucial application in the field of ultrashort pulse: spectral broadening. To demonstrate SESS, the leftmost and the rightmost spectral lobes from the broadened spectrum was filtered by a BPF with 50-nm spectral width.

In this research, the femtosecond pulses peaking at 1300 nm could be obtained by implementing self-phase modulation enabled spectral selection (SESS) in a 9-cm dispersion-shifted fiber (DSF) (Fig. 3-6).

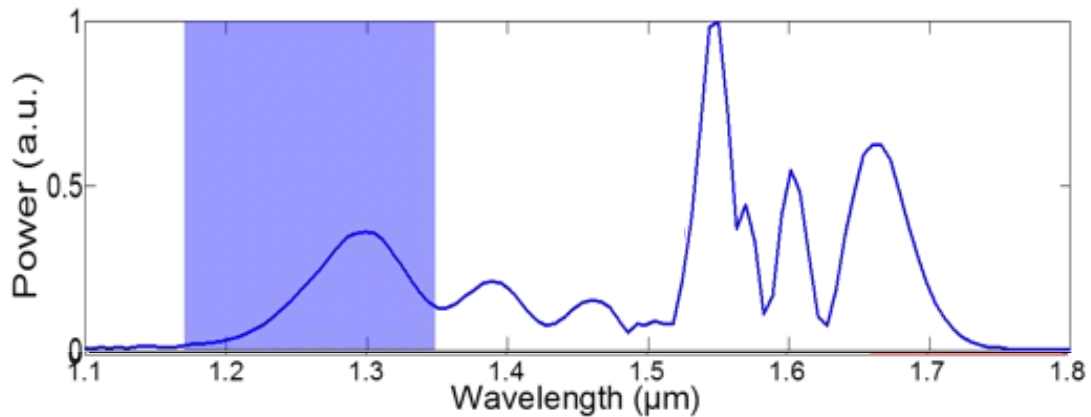


**Fig. 3-6 SESS source with peak power at 1300 nm.** The leftmost spectral lobe peaked at 1300 nm, and the resulting pulse was measured by an intensity autocorrelator. The SESS source based on 9-cm DSF produced  $\sim 100$ -fs pulses with  $\sim 16$ -nJ pulse energy at 1300 nm.

To obtain SHG and 3PEUVF imaging for protein crystals detection under 775-nm beam, the frequency doubling from 1550 driven by the EDFL laser can be realized by implementing with a nonlinear crystal. The MgO: PPLN crystal was selected to achieve frequency doubling. In contrast to other nonlinear crystals, MgO: PPLN has unique advantages for frequency doubling to visible wavelengths. To be specific, it is a non-critical quasi-phase-matching interaction employing the highest nonlinear optical coefficient. A short crystal ensures high conversion efficiency in ultra-short pulse lasers while minimizing group velocity dispersion. The large nonlinearity together with a long crystal allows high second harmonic generation efficiencies even at modest power levels.

In this study, the EDFL laser source operated at a 31-MHz repetition rate focusing on the 0.3-mm long MgO: PPLN crystal to perform frequency-doubling, which generated pulses centered at 775 nm as presented in Fig. 3-7.

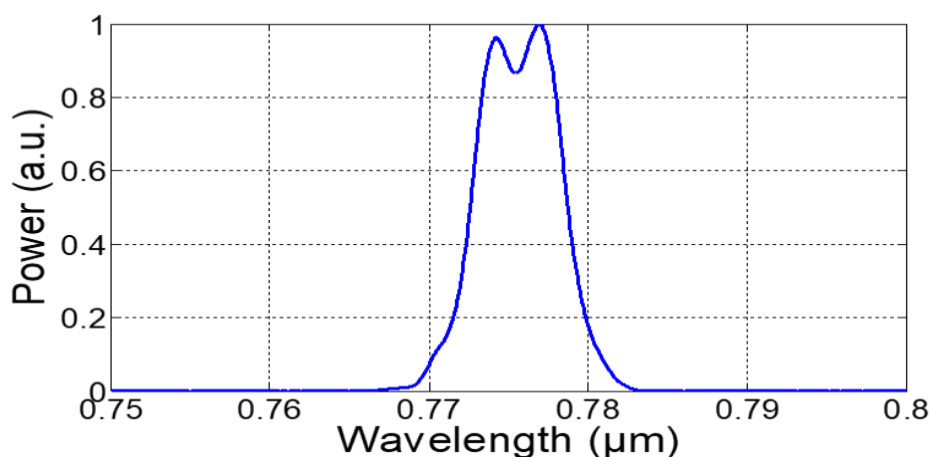


**Fig. 3-7 Simulation of frequency-doubling.** A periodically MgO:PPLN crystal was used for frequency-doubling, generates pulses centered at 775 nm.

In order to perform different imaging methods, a flip mirror was introduced to choose excitation beams (775 nm/1300 nm) within the scanning microscope. When choosing a 1300 nm excitation beam, a DM1 process was used to separate the excitation beam and the emitted signal. As shown in Fig. 3-8, dichroic mirror (DM) 1 cut at 550 nm to separate SHG from THG, and then a 425/50 bandpass filter was used for THG detection. When choosing a 775 nm excitation beam, a different set of DM2 and BPFs were used according to the modalities (THG and SHG/3PEF). The DM2 cut at 360 nm to separate SHG and UV fluorescence/THG. Then a 387/15 BPF and a 355/46 BPF as BPF3 and BPF4 were also used for SHG/3PEF detection (under 775-nm excitation) as shown in Fig. 3-9. The THG, SHG, and 3PEUVF signals generated at the sample were collected in the spherical lens and then measured with two PMTs. The basic MPM microscopy instrument was designed for compatibility with the multi-well plates. Modifications include the addition of a miniature platform to allow XYZ positioning of crystals in different sample containers. A software suite and a data acquisition card were used to acquire images.

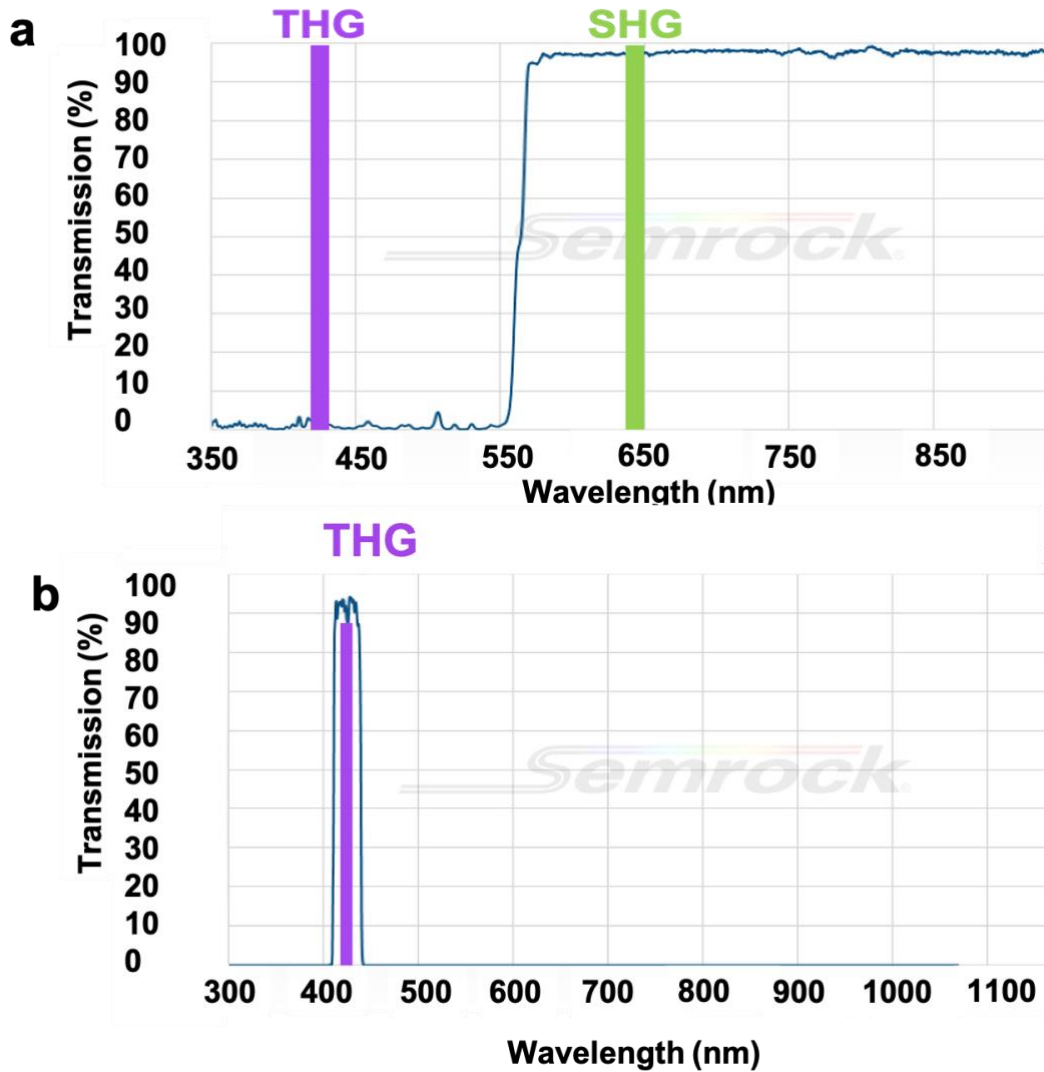


**Fig. 3-8 THG signal selection by setting DM (dichroic mirror) and BPF (bandpass filter) under 1300 nm excitation.**

(a) The dichroic mirror cuts at 550 nm to separate SHG and THG. (b) The bandpass filter is used to select the THG signal. In fluorescence microscopy, dichroic filters are used as beam splitters to direct illumination of an excitation frequency toward the sample and then at an analyzer to reject that same excitation frequency but pass a particular emission frequency.

The bandpass filter (BPF) is a device that passes frequencies within a certain range and rejects (attenuates) frequencies outside that range. The main function of such a filter in a transmitter is to limit the bandwidth of the output signal to the band allocated for the transmission.

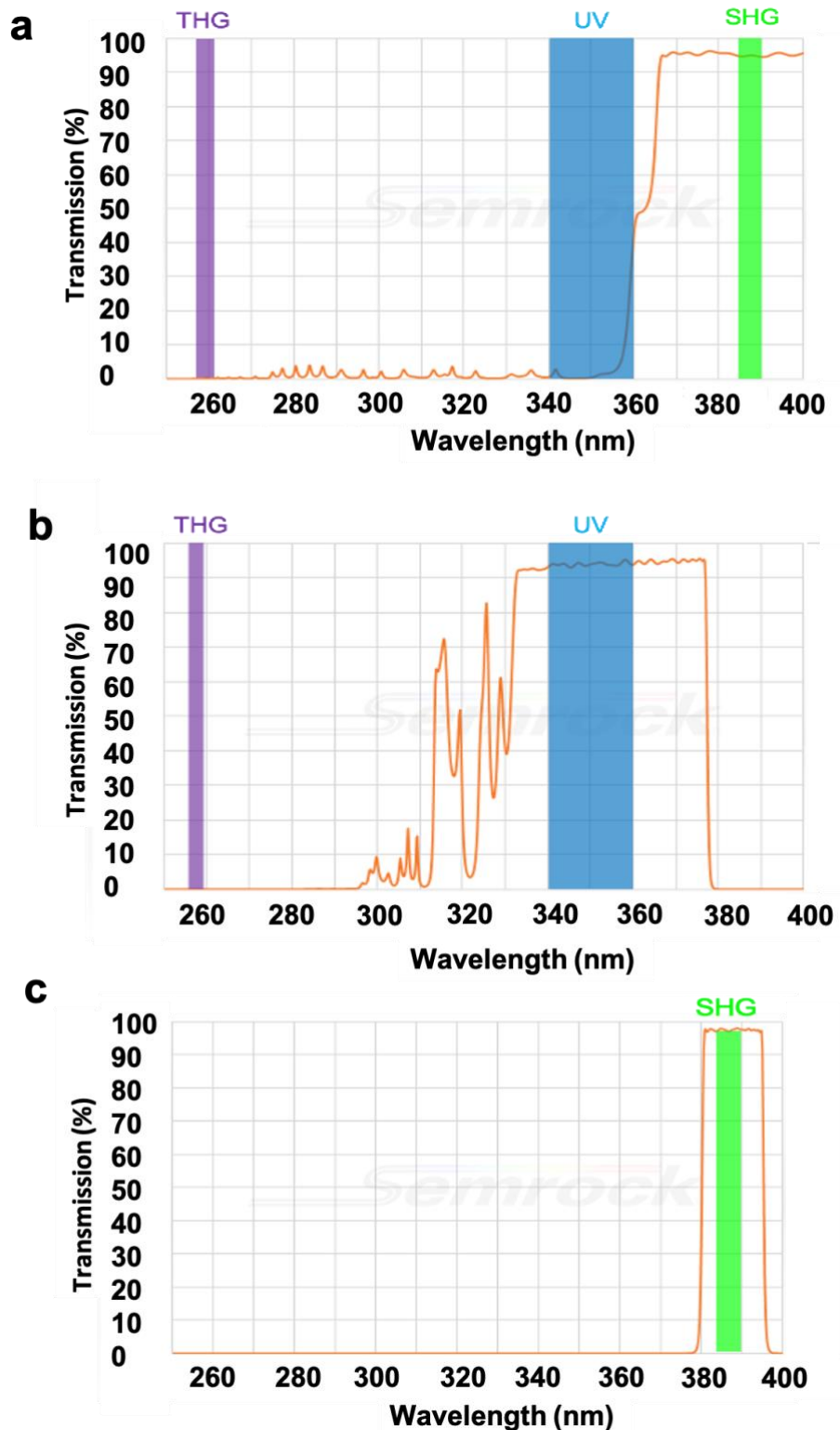


**Fig. 3-9 SHG/UV fluorescence signal selection by setting DM2 and BPFs under 775 nm excitation.**

(a) The dichroic mirror cuts at 360 nm to separate SHG and UV fluorescence/THG. (b) The bandpass filter is used to select the UV fluorescence signal. (c) The bandpass filter is used to select the SHG signal.

### 3.2 Poor reproducibility of *in vitro* protein crystallization results

In this study, the protein crystallization was difficult, as nano- or micro protein crystals could not be yielded for each crystallization trial. The poor reproducibility should not originate from the growth conditions, as the crystallization recipes, concentrations, buffer pH were stable (Table 2-5). During the process of nano- or micro-sized protein crystals preparation, identical crystallization droplets from the same mother liquid could yield different crystallization results under the same condition (micro-batch experiments were performed in the same lab and samples were stored at the same temperature with 24 h incubation time). As shown in Fig. 3-10, the crystallization results are different. In Fig. 3-10a, the left graph shows a large number of smaller lysozyme crystals, approx. ranging from 1  $\mu\text{m}$  to 5  $\mu\text{m}$ , while the middle graph presents few larger crystals (approx. 50  $\mu\text{m}$ ) and the right graph shows that even under the same crystallization condition are almost no protein crystal at all. This phenomenon occurred not only with lysozyme but also with thaumatin and proteinase K, as shown in Fig. 3-10b and Fig. 3-10c.

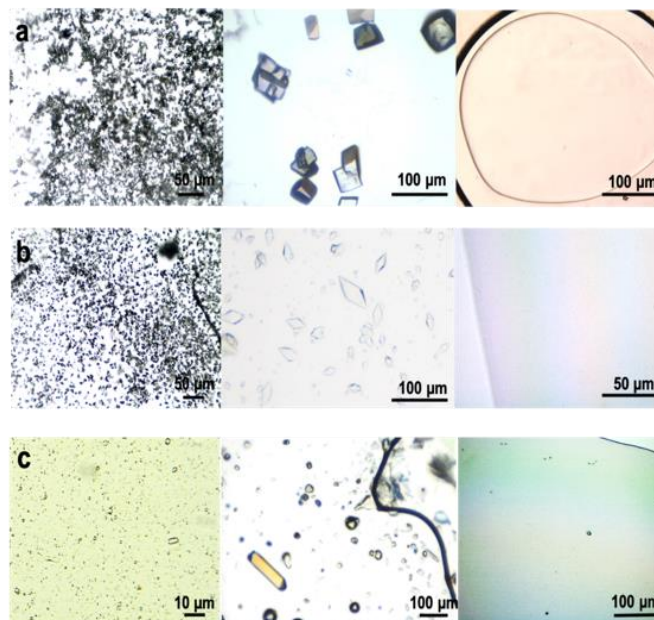


**Fig. 3-10 Protein crystallization results under some conditions.**

(a) Lysozyme. (b) Thaumatin. (c) Proteinase K. The left graphs show the nano- or micro-sized protein crystals of different dimensions, ranging from  $\sim 1$   $\mu\text{m}$  to 5  $\mu\text{m}$ . The middle graphs show the relatively bigger protein crystals: approx. 30-100  $\mu\text{m}$ . The right graphs show no protein crystal.

### 3.3 THG/SHG imaging

Regarding the THG/SHG measurement, sample containers included the LCP sandwich plate, MRC-2 plate, and PDMS microfluidic chip, which were used for both protein crystals incubation and detection. The THG/SHG measurement aimed to select a suitable sample container for the MPM system. The specification for sample containers and imaging conditions can be seen in Table 3-3.

**Table 3-3** Specification for sample containers and imaging conditions.

Containers	Volume of mixing solution	Crystallization wells	exposure time (s)
LCP sandwich plate	1 $\mu$ l (in each well)	96	3-5
PMDS microfluidic chip	100 $\mu$ l (in each plate)	410	3-5
MRC-2 plate	1 $\mu$ l (in each well)	96	3-5

After summarizing the different specifications for sample containers and imaging conditions (Table 3-3), the PDMS microfluidic chip consumes less sample volume but provides the most crystallization conditions.

Among the common sample containers, the MPM imaging system exhibited excellent compatibility with different sample containers. The results showed that the lysozyme and thaumatin crystals with higher space groups in three containers could be easily detected by SHG and THG imaging. Therefore, the LCP sandwich plate, the MRC-2 crystallization plate, and the PDMS microfluidic chip can be used as a sample container for MPM detection.

By combining the standard crystallization plate format, the crystallization drops could be pipetted in the LCP sandwich plate with a dispensing robot (or pipetted one by one manually). With the transparent thin-glass design, the plate allowed the performance of an *in situ* detection without removing samples from containers. However, the nano- or micro-sized protein crystals were found to be fragile when removing the crystal sample into the LCP sandwich plate, due to the mechanical stress on a very thin cover glass.

There were 96 protein crystal samples available for detection in the LCP sandwich plate. Lysozyme and thaumatin crystal samples were selected to perform THG/SHG imaging. Fig. 3-11 shows that the THG and SHG signals from the lysozyme and thaumatin protein crystals can be detected. However, Fig. 3-11a shows that the SHG signal of lysozyme come from the edge of the crystals, only showing some bright points.

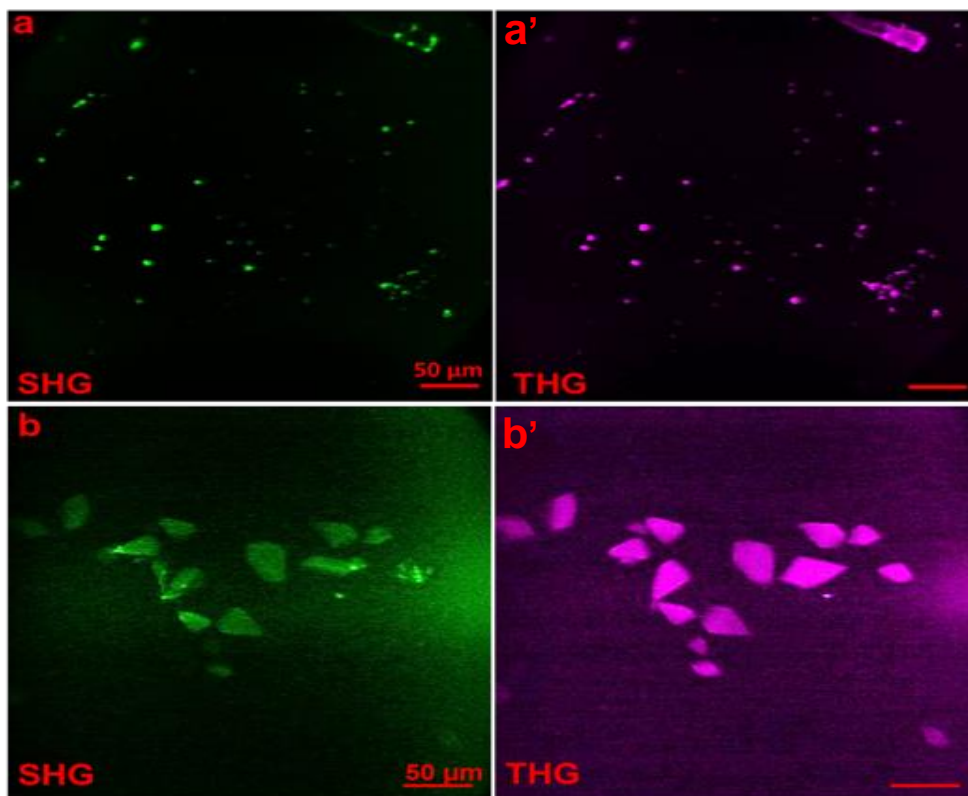


**Fig. 3-11 SHG and THG detection images from a LCP sandwich plate.** (a) SHG imaging of lysozyme crystals. (a') THG imaging of lysozyme crystals. (b) SHG imaging of thaumatin crystals. (b') THG imaging of thaumatin crystals.

There are 96 units in the MRC-2 plate, each unit of which consists of two protein wells and one reservoir well. By monitoring samples through an optic microscope, which was relatively easy to locate the sample positions according to the labeling numbers of the MRC-2 plate. According to the result in Fig. 3-12, the MPM system was allowing protein crystals to be detected in the MRC-2 crystallization plate. Similarly, the SHG signals of lysozyme and

thaumatin crystals came from the edge of the crystals. However, Fig. 3-12b shows that some SHG signals are not overlapping with the THG signals.

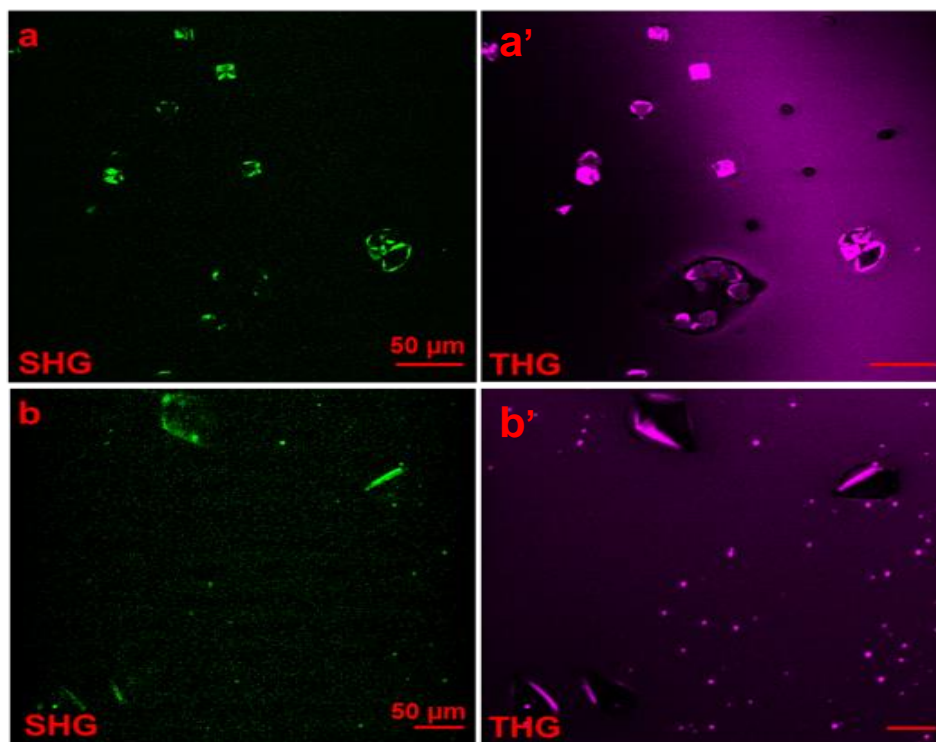


**Fig. 3-12 SHG and THG detection images from an MRC-2 crystallization plate.**

(a) SHG imaging of lysozyme crystals. (a') THG imaging of lysozyme crystals.  
(b) SHG imaging of thaumatin crystals. (b') THG imaging of thaumatin crystals.

PDMS microfluidic chips were also used to grow and store the protein crystals. The chip consists of more than 400 wells for incubation with a position label corresponding to each well. Fig. 3-13a shows the position labels (F32-F34) on the PDMS chip. THG imaging of these position labels is shown in Fig. 3-13a', and the sample in the chip is easy to locate applying the THG imaging of position labels.



**Fig. 3-13 Bright-field and THG imaging of position labels located on a PDMS microfluidic chip.**

(a) Bright-field imaging for position labels from PDMS microfluidic chip.

(a)' THG imaging for position labels from PDMS microfluidic chip.

Different from the LCP sandwich plate and MRC-2 plate, the PDMS microfluidic chip possesses 2 inlets which are connected with a wider main channel. The mixed crystallization solution could be injected through the tubing at one time. Sealing of those inlets does not need any bonding processes which are necessary required for glass slides or covers.

The result showed that the MPM system allowed protein crystals to be detected in the PDMS microfluidic chip. Moreover, Fig. 3-14b shows that the SHG signals of needle-like salt crystals are very strong, while the SHG signals of thaumatin crystals are relatively weak, but still can be detected.

Similar to the experiment results applying the LCP sandwich plate and MRC-2 plate, some SHG signals did not fully overlap with the THG signals.

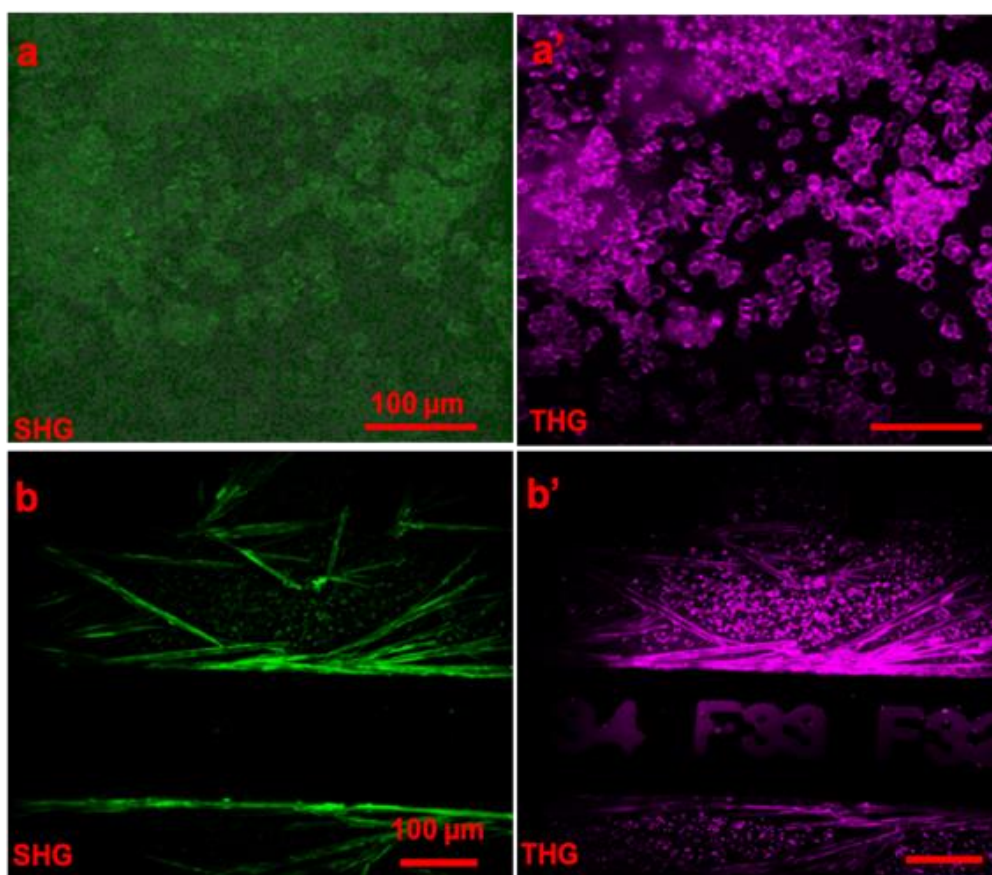


**Fig. 3-14 SHG and THG detection images from a PDMS microfluidic chip.** (a) SHG imaging of lysozyme crystals. (a') THG imaging of lysozyme crystals. (b) SHG imaging of thaumatin crystals and sodium tartrate crystals. (b') THG imaging of thaumatin crystals and sodium tartrate crystals.

### 3.4 Angular-dependent SHG polarization intensity

The results are shown in Fig. 3-11, Fig. 3-12, and Fig. 3-14, demonstrating a comparison of the THG and SHG detection from different sample containers and suggesting that the THG and SHG signals did not fully overlap with each other. The phenomenon may result in SHG polarization. Owing to its coherent nature, the emerging polarization of SHG generated from the sample highly depends on not only the polarization state of the incident light but also the symmetry and orientation of the samples. For crystals, the SHG polarization response of the crystal is highly sensitive to the lattice orientation of the crystal.

In this part of the study, the SHG intensity response was investigated using protein crystals from different space groups. As shown in Table 2-5, glucose isomerase and thaumatin with two different space groups were selected, and micro or nano-sized crystals were prepared.

The polarization dependence on glucose isomerase and thaumatin micro-sized crystals were examined from 0–90° by rotating the waveplate manually, with measurements taken at 10° intervals. A representative SHG image stack is shown in Fig. 3-15, which shows a noticeable increase or decrease in the SHG signal intensity with an increasing polarization angle. However, the SHG signal intensity did not present any linear increase or decrease when the angular degrees were increased.

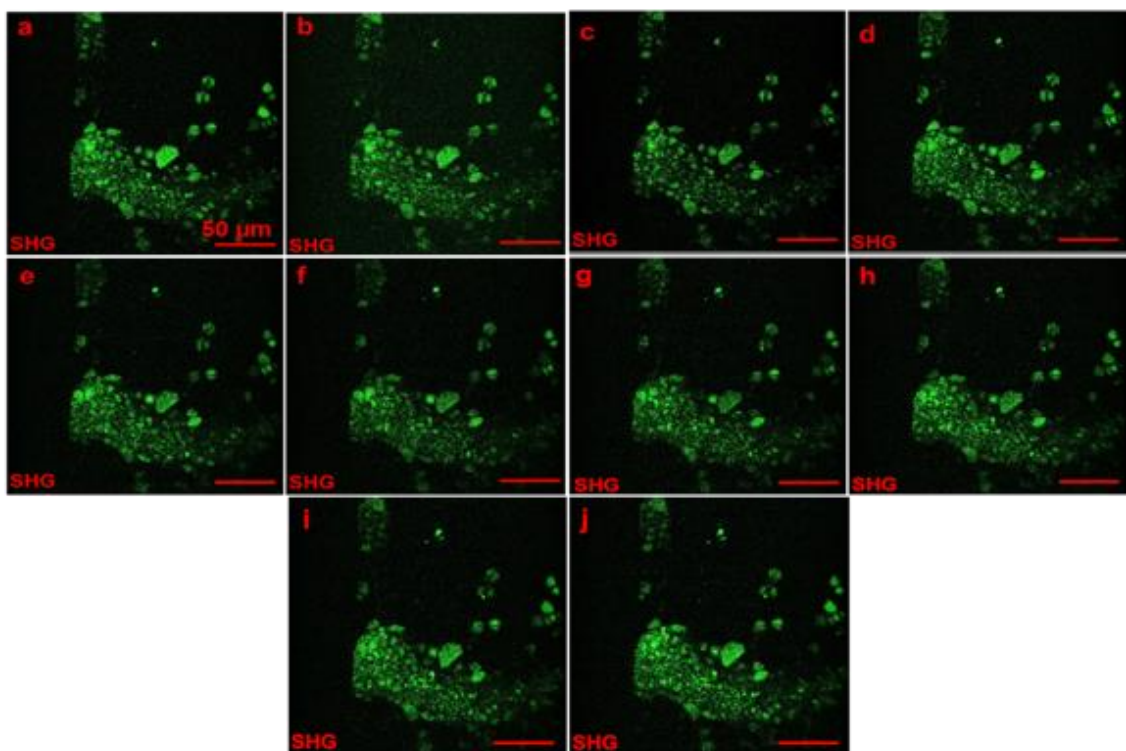


**Fig. 3-15 Polarization-dependent SHG signal intensities of images taken from glucose isomerase crystals.**

(a)-(j) Angular dependence of recorded SHG intensities applying a suspension of glucose isomerase crystals and changing the polarization plane in steps of 10° from 0-90° by rotating a half-wave plate (HWP) in the MPM system. The scale bar corresponds to 50 μm.

As for the thaumatin crystal, as shown in Fig. 3-16a, there is no signal in the red circle. Although the SHG signal at the same position in Fig. 3-16j is found to be very intense, to obtain precise information about the SHG response according to the angular change is difficult in Fig. 3-16. To further study the relationship between the SHG response and angular change, the SHG signal intensities with polarization angle changes were simply calculated. Four particles with similar dimensions were selected randomly and marked by four rings of different colors. For these calculations, a densitometric quantification was performed using the program ImageJ and particles, i.e. four in each image shown in Fig. 3-16 a-j, were analyzed individually by integrating the total grey-scale pixel intensities over the definite particle areas. The obtained mean of four intensity values for each image is plotted in the context of the polarization angle, as shown in Fig. 3-16k.

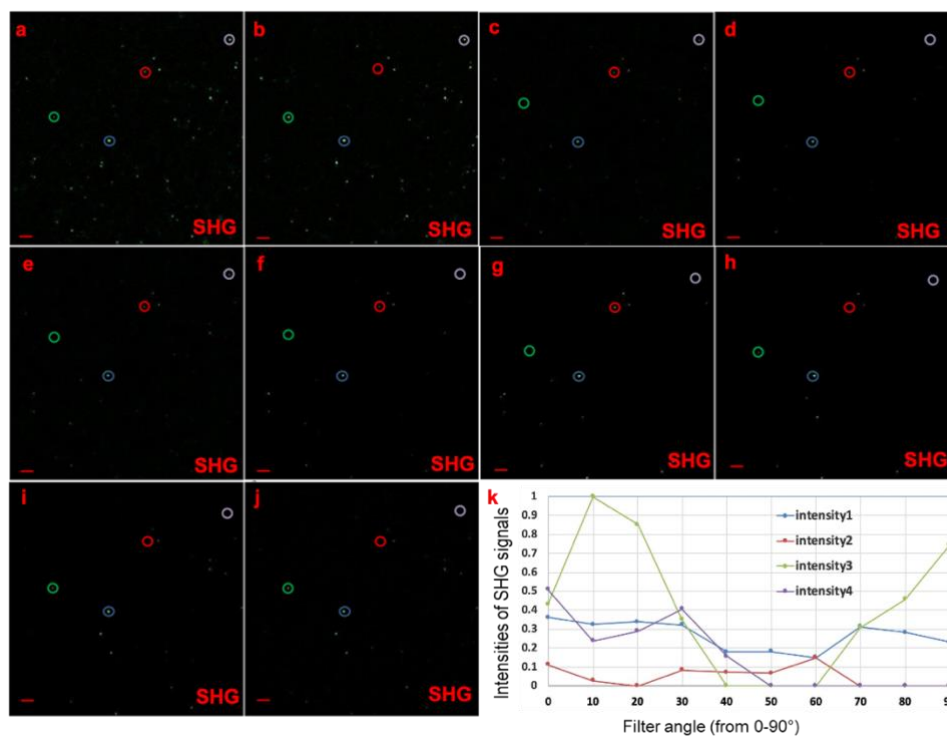


**Fig. 3-16 Polarization-dependent SHG signal intensities of images taken from thaumatin crystals.**

(a)-(j) Angular dependence of recorded SHG intensities applying a suspension of thaumatin crystals and changing the polarization plane in steps of  $10^\circ$  from  $0$ - $90^\circ$  by rotating a half-wave plate (HWP) in the MPM system. The scale bar corresponds to  $20 \mu\text{m}$ . (k) Polarization-dependent line chart of the recorded SHG signal intensities.

In Fig. 3-16 k, a line chart is used to show the variations of thaumatin crystals. Similar to the previous experimental results, the SHG intensity of the thaumatin crystal was also altered when the angle changed. The SHG intensity of the thaumatin crystal displayed a minimum near 50 ° and a maximum near 0 ° and 90 °.

### **3.5 SHG detection of salt crystals**

According to the THG/SHG testing, THG and SHG imaging methods were sufficiently sensitive to allow the detection of small-sized particles that lack centrosymmetric structures. However, the SHG response can also come from centrosymmetric materials. Therefore, investigating salt crystals from different space groups by SHG imaging is necessary, thereby providing additional information about the SHG response from centrosymmetric salt crystals and enabling researchers to determine the potential of false positives for SHG signals in advance.

In this experiment, most of the salts were regularly used as precipitants in protein crystallization. These salt crystals exhibiting centrosymmetry and non-centrosymmetry were prepared and the space groups of these selected salt crystals can be seen in Table 3-4.

A series of measurements of different salt crystals were completed using the in-house MPM instrument. Fig. 3-17 shows the SHG signals of the salt crystals, which were imaged using the MPM-instrument. As is known to all, an SHG signal can also be produced by salt crystals, some of which produce strong signals such as  $\text{Li}_2\text{SO}_4$  and  $\text{KH}_2\text{PO}_4$  while others not. Surprisingly, even some centrosymmetric space groups detected SHG signals such as NaCl and KCl (see Fig. 3-17a and 3-17d). A summary of all tested salts with their space groups and detected SHG intensities is shown in Table 3-4. Notably, the detected SHG signals for salt crystal types were reported SHG-negative. However, all crystal types that are known to produce a detectable SHG signal could also be detected using the MPM system. From the imaging results of salt crystals, it comes obvious that even some centrosymmetric salt crystals

could produce reasonable SHG and THG signals, which had not been previously reported (Closser *et al.*, 2013).

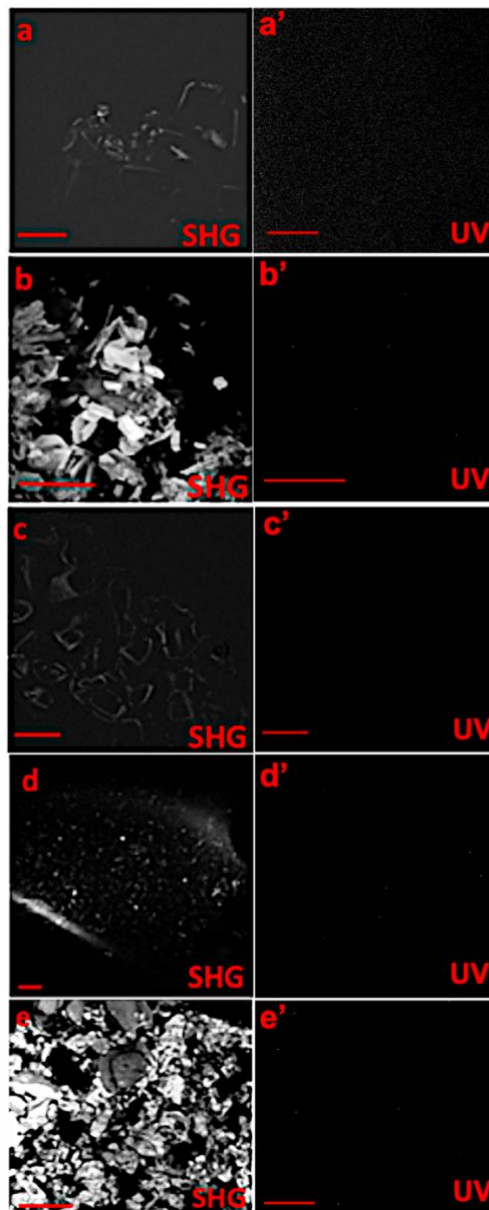


**Fig. 3-17 SHG images of salt crystals captured by the in-house MPM instrument.**

(a) SHG imaging of NaCl crystals. (a') UV imaging of NaCl crystals. (b) SHG imaging of  $\text{Li}_2\text{SO}_4 \cdot \text{H}_2\text{O}$  crystals. (b') UV imaging of  $\text{Li}_2\text{SO}_4 \cdot \text{H}_2\text{O}$  crystals. (c) SHG imaging of  $\text{Na}_2\text{SO}_4$  crystals. (c') UV imaging of  $\text{Na}_2\text{SO}_4$  crystals. (d) SHG imaging of KCl crystals. (d') SHG imaging of  $\text{Na}_2\text{SO}_4$  crystals. (e) SHG imaging of  $\text{KH}_2\text{PO}_4$  crystals. (e') UV imaging of  $\text{KH}_2\text{PO}_4$  crystals. (the scale bar corresponds to 50  $\mu\text{m}$ ).

**Table 3-4** Information of salt crystals.

Salt crystals	Space group	Centrosymmetric	MPM recorded SHG signal yes/no	MPM recorded SHG signal activity	Corresponding references about SHG signals
NaCl	F m-3m	Yes	Yes	**	No SHG (Closser <i>et al.</i> , 2013)
Ca (CH <sub>3</sub> COO) <sub>2</sub> · H <sub>2</sub> O	P-1	Yes	No		No report
NaKC <sub>4</sub> H <sub>4</sub> O <sub>6</sub> · 4H <sub>2</sub> O (Sodium Potassium Tartrate Tetrahydrate)	P 2 <sub>1</sub> 2 <sub>1</sub> 2 <sub>1</sub>	No	Yes	*	Yes (Closser <i>et al.</i> , 2013)
Li <sub>2</sub> SO <sub>4</sub> · H <sub>2</sub> O	P 2 <sub>1</sub>	No	Yes	***	Yes (Bayarjargal, 2008)
CaCl <sub>2</sub>	P n n m	Yes	No		No (Closser <i>et al.</i> , 2013)
KCl	F m-3m	Yes	Yes	**	No (Closser <i>et al.</i> , 2013)
Na <sub>3</sub> C <sub>6</sub> H <sub>5</sub> O <sub>7</sub> · 2H <sub>2</sub> O (Sodium citrate dihydrate)	C2/c	Yes	No		No (Closser <i>et al.</i> , 2013)
KH <sub>2</sub> PO <sub>4</sub>	I-42d	No	Yes	***	Yes (Closser <i>et al.</i> , 2013)
NH <sub>4</sub> Cl	P m-3m	Yes	Yes	*	No (Closser <i>et al.</i> , 2013)
MgCl <sub>2</sub>	R -3m	Yes	Yes	*	No report
NaH <sub>2</sub> PO <sub>4</sub>	P 2 <sub>1</sub> /c	Yes	No		No (Closser <i>et al.</i> , 2013)
NaNO <sub>3</sub>	R -3c	Yes	No		No report
(NH <sub>4</sub> ) <sub>2</sub> SO <sub>4</sub>	P n m a	Yes	No		No (Closser <i>et al.</i> , 2013)
NH <sub>4</sub> H <sub>2</sub> PO <sub>4</sub>	I-42d	No	Yes	*	Yes (Closser <i>et al.</i> , 2013)
Na <sub>2</sub> SO <sub>4</sub>	F ddd	Yes	Yes	**	No (Closser, <i>et al.</i> , 2013)

In Table 3-4, \* indicates weak, \*\* strong, \*\*\* very strong

### 3.6 Protein crystal detection with THG, SHG, and three-photon UV imaging

Finally, testing whether the THG, SHG, and three-photon UV can work effectively is necessary. Acquiring SHG and THG was simultaneous for 1300-nm excitation. Under 775-nm excitation, SHG and 3PEUVF were simultaneously acquired as well. Fig. 3-18 shows that the point marked by the red circle is unrecognizable using conventional optical microscopy. In addition to the THG and UV signals, however, a clear and strong SHG signal indicated that this was a protein crystal. Furthermore, the THG detection showed different layers where tiny protein crystals were located behind larger, bulk salt crystals. Fig. 3-18a shows that the point marked by the red circle in the bright-field imaging, identifying whether there is a crystal in is difficult. However, THG imaging revealed the outline/shape of the sample as THG was sensitive to optical inhomogeneity. SHG imaging demonstrated that non-centrosymmetric salt crystals and tiny protein crystals could produce SHG signals.

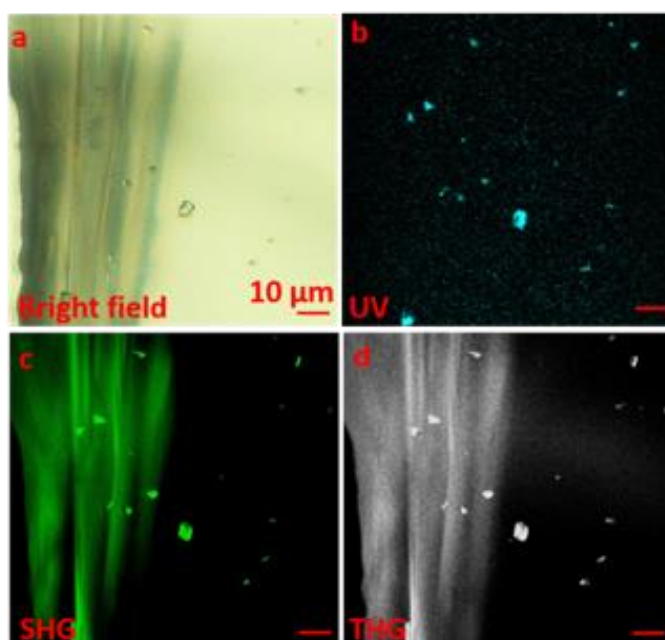


**Fig. 3-18 MPM imaging system detection for thaumatin crystals and sodium tartrate crystal.**

(a) Bright field imaging. (b) 3PEUVF imaging. (c) SHG imaging. (d) THG imaging.

### 3.7 Summary and discussions

#### 3.7.1 Poor reproducibility of *in vitro* protein crystallization

The poor reproducibility crystallization results were observed under the same crystallization conditions.

According to the nucleation theory, supersaturation is the driving force for crystal nucleation and growth. The protein crystal size and crystal number are strongly affected by the sample solution supersaturation state, which can be influenced by various kinds of parameters (Chernov, 2003; McPherson, 2004; Christopher *et al.*, 1998). The number of crystals relies on the rate of nucleation, i.e. the number of nuclei formed per unit time and per unit volume, which can be expressed by an Arrhenius-type equation:

$$J = A \exp\left(\frac{-\Delta G}{kT}\right) \quad (4-1)$$

Where  $k$  is the rate constant,  $T$  is the absolute temperature (in kelvins),  $A$  is the pre-exponential factor, a constant for each chemical reaction,  $\Delta G$  is free energy.

$A$  depends on supersaturation, which demonstrates that the nucleation rate is zero until a critical value of supersaturation is achieved, and the rate increases rapidly after reaching the critical value of the supersaturation state. In other words, the higher the supersaturation is, the higher the nucleation rate will be.

Fig. 3-19 shows a plot of free energy versus the cluster size where the value of this maximum ( $r^*$ ) is defined as the critical radius or nucleus size. It has been proven that the value of  $r^*$  decreases as the supersaturation increases. Moreover, at higher supersaturation, crystal nucleation dominates crystal growth, resulting in smaller crystals. In other words, the higher the supersaturation is, the smaller the crystal size will be.

According to the published literature, protein crystallization is very sensitive to even minute variations in the solution concentration caused by temperature during the preparation of the crystallization solution (Chen *et al.*, 2015). There are many factors that are not controlled well during the preparation of the crystallization solution. For example, temperature, humidity, air pressure, dust particles in the air, *etc.*

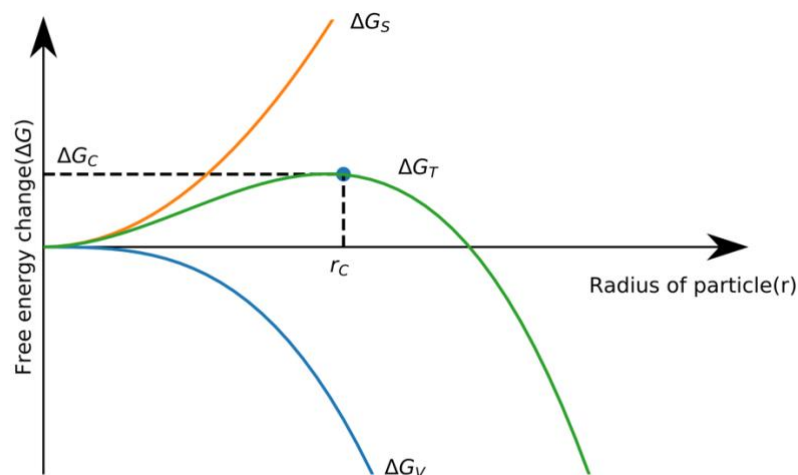


**Fig. 3-19 Total free energy versus cluster size.**

Where  $\Delta\mu$  is the solution supersaturation;  $\Delta G$  is the free energy;  $\Delta G_T$  is the difference between the free energy of the system in its final and initial states;  $r$  is the radius of the nucleus and  $\sigma$  is the surface free energy. The value of  $r$  at this maximum ( $r^*$ ) is defined as the critical radius or nucleus size (Modified from Vekilov, 2010).

The previous study has confirmed that weather parameters can affect lysozyme crystallization by influencing the supersaturation of the crystallization drop (Cheng *et al.*, 2017). As mentioned in previous reports, the protein crystals were larger and the protein crystallization success rate was lower at a higher ambient temperature, higher air humidity, and lower air pressure. Among these parameters, the air humidity during the sample solution preparation process contributed the most (Cheng *et al.*, 2017).

In the case of poor reproducibility of crystallization results, the air particles can also be involved in the crystallization experiment during the sample solution preparation process. These particles in the crystallization solution can act as heterogeneous nucleants for protein crystallization and influence the

nucleation rate, thereby resulting in different crystallization behaviors. Hence, crystallization results may vary with weather parameters in the lab.

Notably, if a crystallization recipe has the potential to yield nano- or micro-sized protein crystals, but would be ignored owing to poor reproducibility in the subsequent studies. Hence, improving crystallization reproducibility in order to increase the chance of obtaining nano- or micro-sized crystals is essential.

### **3.7.2 Sample container selection**

When assessing the compatibility of the MPM system with the different sample containers, practical considerations include the THG/SHG testing experiment and the sample preparation process should be considered.

After the THG/SHG testing experiment, the in-house MPM instrument exhibits a particularly high sensitivity for the SHG detection of micro-sized protein crystals. The system shows its versatility with respect to changes in the optical design and the used sample container, allowing crystal identification with a smaller risk of false-negative results. However, there are still some limitations during the sample preparation.

When pipetting samples into the LCP sandwich plate and MRC-2 crystallization plate, the long-time evaporation of the sample and human errors resulting from repetitive work may affect the crystal nucleation and growth if there is no crystallization robot to pipette samples automatically. According to the previous study, protein crystallization is very sensitive to even minute variations in the solution concentration, numerous crystal preparation process may affect the crystallization results (Chen *et al.*, 2012). The selection of PDMS microfluidic chips aims to minimize the preparation steps of crystals, and the manual, short (2-5 s), one-time sample pipetting method avoids human errors and minute variations in the solution concentration. Microfluidic scales can also limit convective phenomena, which is necessary for the growth of uniformly sized crystals (Shim *et al.*, 2007).

As the leading platform for microfluidic technology implementation, the microfluidic chip is characterized primarily by its effective structure (channels,

reaction chambers, and other functional components) that can accommodate fluids on a micron-scale at least at one latitude (Guha *et al.*, 2012; Sui & Perry, 2017). This kind of chip is also widely applied in the protein crystallization field (Li *et al.*, 2006; Du *et al.*, 2009; Sui & Perry, 2017).

In contrast to the other two sample containers, the PDMS microfluidic chip has several advantages. Firstly, the PDMS microfluidic chip can reduce the production and time-consuming purification of proteins and enable high-throughput screening as a few nL– $\mu$ L of protein samples are required in microfluidic devices. Secondly, the PDMS microfluidic chip is suitable for performing high-throughput screening of crystallization conditions. In this work, 10–20  $\mu$ L of protein samples are sufficient for one PDMS microfluidic chip. The PDMS microfluidic chip consists of ten main channels marked by A–J, and each row of crystallization wells is labelled by the numbers 0–41. Thus, 100  $\mu$ L of protein samples in this PDMS microfluidic chip can provide 410 sample selections.

### **3.7.3 Angular dependence of SHG intensity from the protein crystal**

To test the feasibility of the imaging system, higher-symmetric lysozyme and thaumatin crystals were tested in different containers with THG and SHG techniques. The results showed that the THG and SHG signals could be detected from higher symmetry and micro-sized protein crystals. However, the SHG and THG signals did not fully overlap with each other, which was presumably caused by the SHG polarization.

As is known, SHG shows selectivity for ordered systems, which is invisible in centrosymmetric media and amorphous materials. The same selective detection is applicable to the polarization-dependence of SHG (Chu *et al.*, 2007). Information on the orientation of collagen fibers, cells, and protein crystals can be found from a series of polarization-dependent SHG measurements (Petzold *et al.*, 2012). Hauptert and other researchers have found that the polarization of SHG intensity is dependent on the polarization state of the incident light, symmetry of crystals, and angular orientation of crystals (Hauptert & Simpson 2011).

Since the incident light was fixed in this experiment, the symmetry and angular orientation of the protein crystals were studied to test whether the SHG polarization response of the crystal depends on the angular change. According to the results shown in Fig. 3-14 and Fig. 3-15, these two protein crystals were angular-dependent of the SHG response. To further study the relationship between SHG signal intensities and polarization light angles, a line chart was used to show the variation. Different SHG signals (marked with circles in different colors in Fig. 3-18) were selected from the thaumatin crystal samples with each of them recorded and their intensities calculated at intervals of 10 degrees. Similarly, the SHG intensity of the thaumatin crystal changed with the variation in the angle, as mentioned in the previous experimental results. The SHG intensity of the thaumatin crystal displayed a minimum near 50 degrees, as well as a maximum near 0 degrees and 90 degrees. The SHG signal intensity varied from the maximum to the minimum with a rotation range of roughly 45°, which is in good agreement with crystals of the space group (422) (Xiao *et al.*, 2015).

Previous studies have shown that the angular dependence of the SHG response can be analyzed from the symmetry properties of the second-order susceptibilities for the given crystal. Each crystal class has its angular dependence on the SHG response (Dähn *et al.*, 1996). In this study, observing the angular dependence of the SHG signal with the change in the incident light angle could increase the possibility of identifying more nano- or micro-sized protein crystals. For crystallization screening experiment, scientists would like to ignore the existence of the nano- or micro-sized protein crystals and corresponding crystallization recipe owing to low-sensitive detecting ability. Thus, the incorporation of the angular dependence of SHG measurements into protein crystal detection can extend the potential of protein crystal detection and characterization.

#### **3.7.4 SHG signals from centrosymmetric crystals**

In theory, centrosymmetric crystals show no SHG effect, due to a lack of an independent irreducible component of tensors. However, Terhune observed

the SHG response from the calcite crystal, which is a centrosymmetric crystal. During the 1960s, SHG was observed for many other centrosymmetric crystals. Several studies have already reported SHG signals from centrosymmetric crystals, including centrosymmetric supermolecular crystals, C1v cubic centrosymmetric crystals with vicinal faces (Guo *et al.*, 2002), and crystals that belong to the space group P21/c, which is a combination of two non-centrosymmetric space groups (P21 and Pc) (Nalla *et al.*, 2015). Among these examples, the majority results from the surface SHG, which is a special case of SHG generated from the breaking surface. Since the centrosymmetric structure in centrosymmetric media is only broken in the first, second, or third atomic or molecular layer of a system, properties of the SHG signal then provide information about the surface atomic or molecular layers only. Detecting the surface SHG even for media that do not generate SHG signals in bulk is possible.

In this experiment, not all selected salts crystals are centrosymmetric. For example,  $\text{Li}_2\text{SO}_4$  and  $\text{KH}_2\text{PO}_4$  are non-centrosymmetric. Therefore, the strong SHG signal originated mainly from the bulk of the crystal. In contrast, the weak SHG signal of NaCl and KCl originated from the surfaces of the centrosymmetric crystal rather than from the bulk. In view of the bulk electric quadrupole and magnetic dipole effects, the existing SHG signal from these samples can be explained by the breaking of the crystal symmetry at the surface, which gives rise to a nonlinear signal even in centrosymmetric crystals (Wang *et al.*, 2018).

In similar researches on the SHG response of salt crystals, the MPM system identity SHG signals from NaCl and KCl were not reported before (Cossler *et al.*, 2012). The results show that the MPM system exhibits a highly-sensitive detection ability.

## **4. *In vitro* and *in vivo* protein crystal detection**

### **4.1 Complementary methods for detecting protein crystal**

In the past two decades, there have been comprehensive studies about how different methods are used for detecting protein crystals. The aim of the MPM system is to distinguish protein nanocrystals from salt crystals as well as amorphous substances. In order to compare different commercially available methods for identifying nano- or micro-sized protein crystals, four methods (DLS, DDLS, TEM imaging, X-ray powder diffraction) were performed in this study to detect the presence of nano- or micro-sized protein crystals.

Compared with *in vitro* protein crystals, *in vivo* protein crystals occur naturally in cells and are wrapped by the cell membrane. Therefore, the nucleation and growth of *in vivo* crystals are influenced by intercellular matrices. In this case, the ideal result from the MPM system is not only the detection of *in vivo* protein crystals but also the avoidance of the interference from the cell membrane, materials in cells.

This chapter discusses the detection results of *in vitro* and *in vivo* protein crystals applying different imaging methods.

#### **4.1.1 DLS and DDLS experiments**

As a non-invasive, fast method of detecting early stage of crystal nucleation, DLS can be used to investigate the homogeneity and size distributions of particles from 1nm to about 10  $\mu\text{m}$  via the analysis of scattering intensity. DLS results showed that the radius distribution of three samples increased over time, demonstrating that the DLS can detect the early-stage nucleation. As time went by, the increased DLS intensities of three samples were detected with the appearance of the second radial fraction around 100 nm. However, the formation of the second radial fraction didn't mean the first crystalline particles were formed.

In contrast to the DLS method, DDLS can identify nanocrystals by detecting the depolarized signal, which is a combination of form and intrinsic birefringence. The form birefringence results from the anisotropy of individual

protein molecules in the crystal lattice, being very sensitive to the direction in a geometrically ordered material such as crystal. Thus, the DDLS method allows identifying the presence of ordered crystals because of the birefringent properties. DDLS measurements have been conducted with lysozyme, thaumatin, and proteinase K nano- or micro-sized crystals. Similar to the results of DLS measurements, the radius distribution of the three samples changed over time. Notably, the DDLS intensity of proteinase K and thaumatin did not increase with the occurrence of the second radius fraction around 100 nm, indicating that the detected particles around 100 nm are disordered particles instead of nano- or micro-sized crystals.

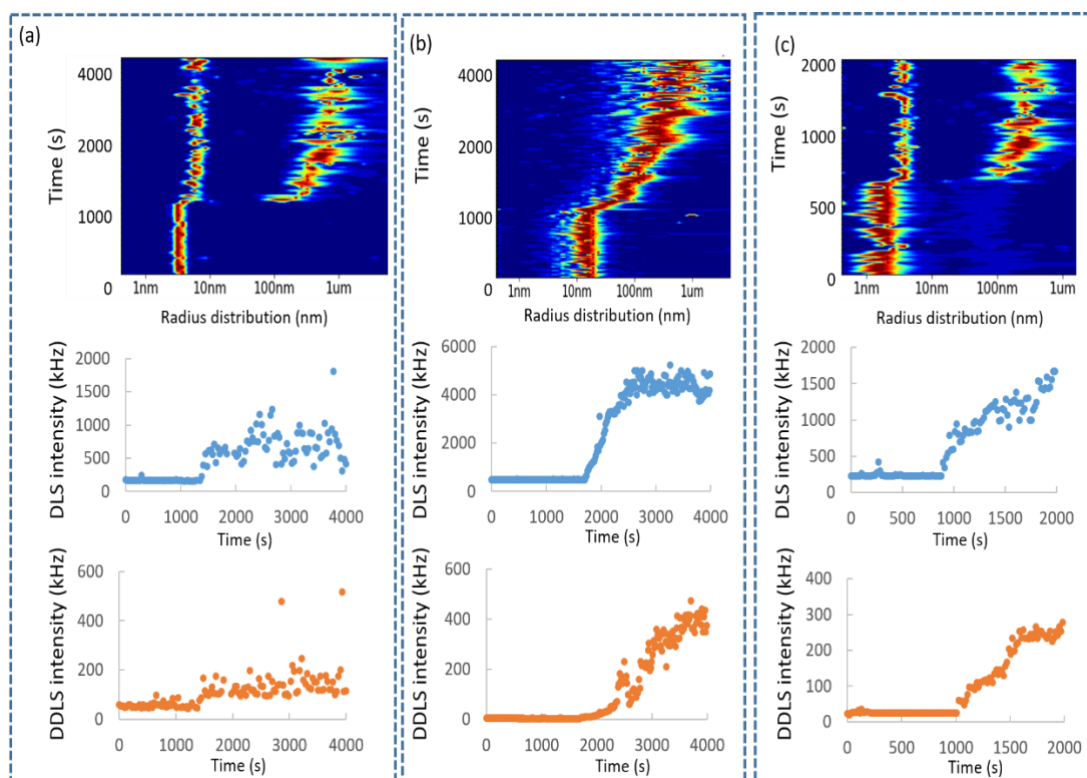


**Fig. 4-1 Particle radius distribution, DLS and DDLS signal intensities of three protein crystallization experiments.** The upper graphs show the radius distribution of the three proteins: lysozyme, thaumatin, and proteinase K. The increasing radius fraction with a size of around 100 nm occurred after the precipitant was added. The corresponding signal intensities for the polarized (blue) and depolarized (orange) signals are shown in the middle and lower graphs, respectively. An increase in the DDLS signal intensity can be detected for lysozyme, thaumatin, and proteinase K.

#### 4.1.2 TEM imaging experiments

The basic principle of TEM is the electron scattering process in the media. When a beam of electrons is incident on the surface of a thin crystalline specimen, the beam of electrons will be scattered by the crystal, and a series of electron beam wavelets will be obtained on the back focal plane of the objective lens. An image of the crystal lattice can be generated when transmitted beams and diffracted beams interfere and overlap again in the subsequent propagation process.

The TEM investigations found that protein samples contained nano- or micro-sized protein crystals with different shapes, sizes, and thicknesses, and the size of these protein crystals ranges from 80 nm to 5  $\mu\text{m}$ . Thaumatin formed bipyramidal crystals, while the other two proteins formed tetragonal crystals. After zooming in, the dark lines and bright fringes were observed, representing atoms, and lattice fringes, respectively, and these fringes could be interpreted as the projection of tunnels between columns of atoms (Fraundorf *et al.*, 2005). As shown in the three samples, the atoms and the lattice fringes could appear in one or more directions. Most of the fringes were straight, but some of them bent inside. However, the TEM images demonstrated that not all lattice fringes could be observed clearly. As shown in Fig. 4-3, only lattice fringes at the edge of the area can be visualized more clearly. This is because the thickness of the crystal sample is uneven and electrons cannot penetrate the thicker parts. Normally, the user can determine the lattice spacing between pixels fringes in TEM images. The simplest and most direct method to measure the lattice spacing values is to directly measure the distance between atomic layers (between two lattice fringes) of the crystal from the high-resolution image. However, the major flaw of this method is the inaccuracy due to the image quality and the user's errors. Another direct method is to draw a selection line through the 10 or 20 atomic layers of interest, and then to measure the length of the selection line and obtain the average lattice spacing value. In three crystal samples, the distance between ten lattice fringes was measured, being around 3-5 nm, which accords with the results of the previous study (Stevenson *et al.*, 2014a).

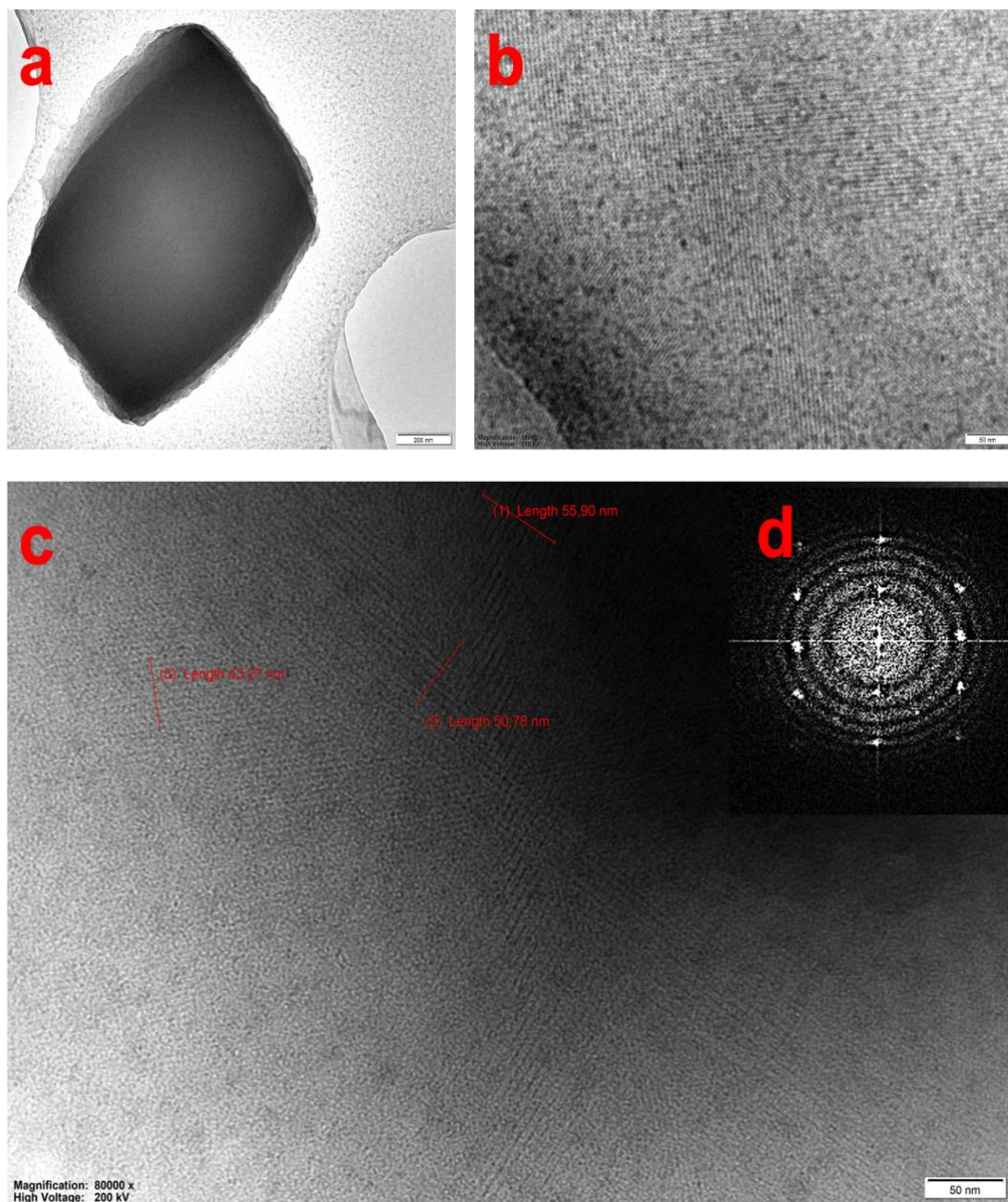


**Fig. 4-2 TEM imaging of nano- or micro-sized lysozyme crystals.** (a) Selected lysozyme crystal. (b) Lattices of nano- or micro-sized lysozyme crystals. (c) High-quality lattices of nano- or micro-sized lysozyme crystals visualized by TEM. (d) Fast Fourier from the (c) (Scale bar: a, 200 nm; b, 50 nm; c, 50 nm).

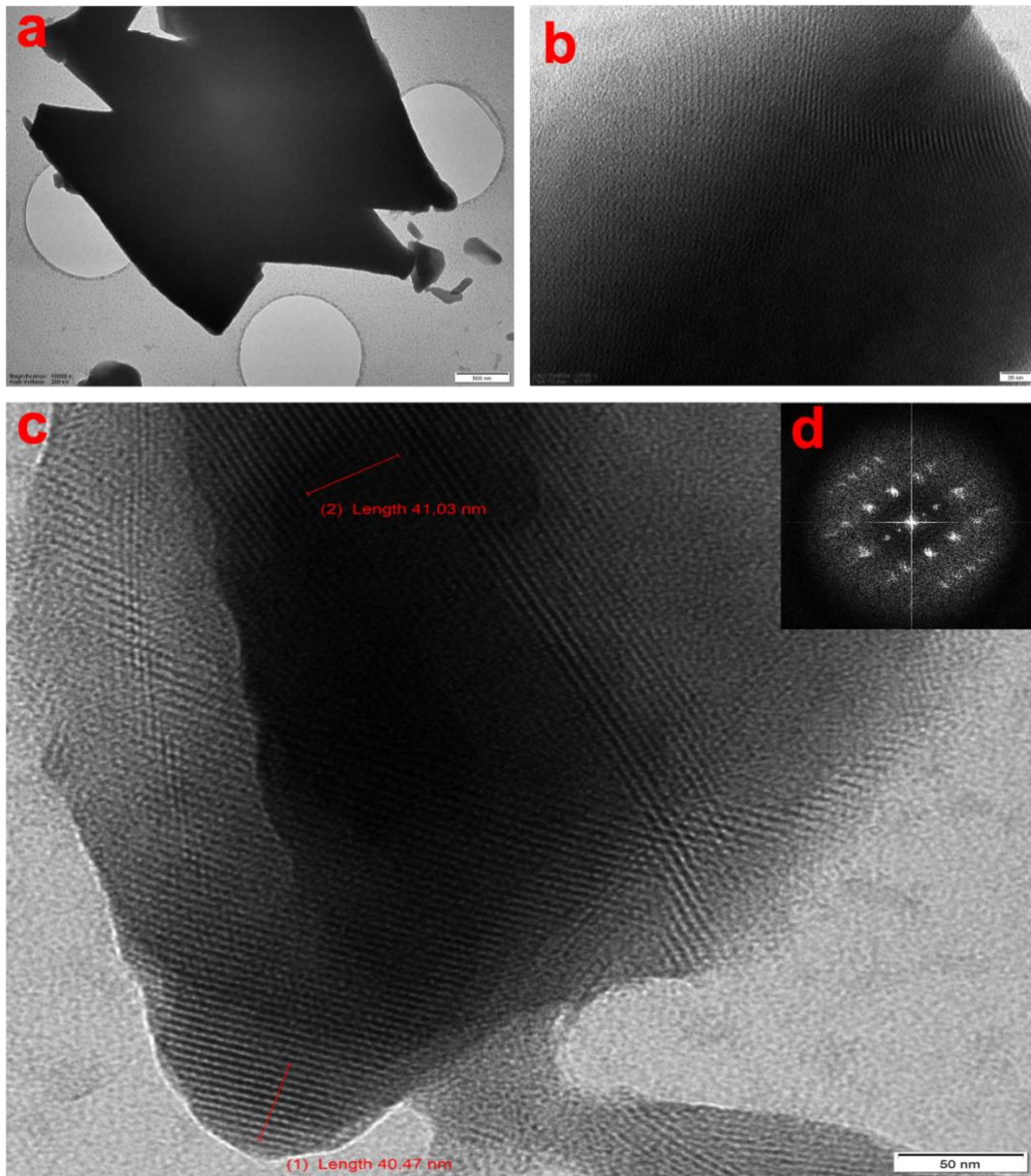


**Fig. 4-3 TEM imaging of nano- or micro-sized thaumatin crystals.** (a) Selected thaumatin crystal. (b) Lattices of nano- or micro-sized thaumatin crystals. (c) High-quality lattices of nano- or micro-sized thaumatin crystals visualized by TEM. (d) Fast Fourier from the (c) (Scale bar: a, 500 nm; b, 20 nm; c, 50 nm)

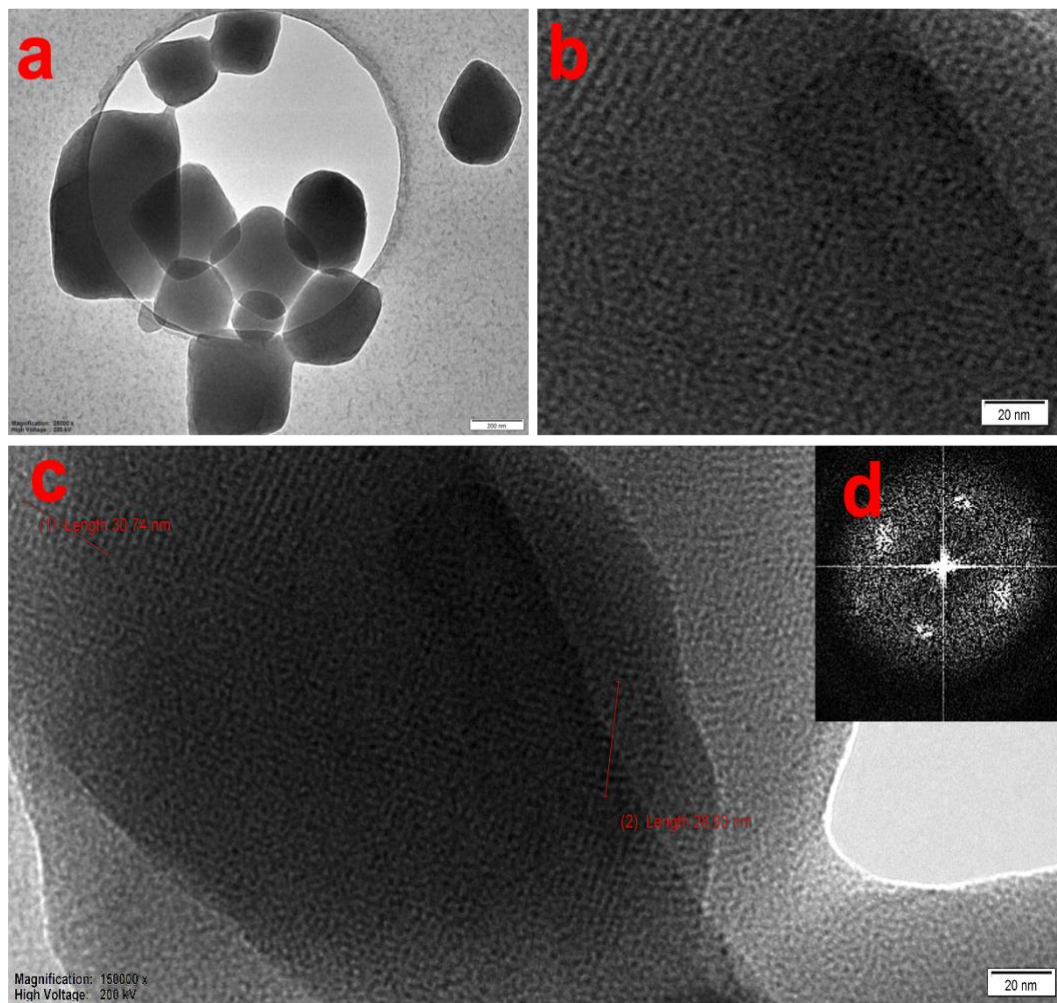


**Fig. 4-4 TEM imaging of nano- or micro-sized proteinase K crystals.** (a) Selected proteinase K crystal. (b) Lattices of nano- or micro-sized proteinase K crystals. (c) High-quality lattices of nano- or micro-sized proteinase K crystals visualized by TEM (d) Fast Fourier from the (c) (Scale bar: a, 200 nm; b, 20 nm; c, 20 nm).

However, the measurements of lattice spacing by calculating the distance between 10 or 20 lattice fringes are not so precise, as the accuracy of this method depends on the contrast between the fringes' spacing and how to set the selection line. Another approach is to employ the fast Fourier transform analysis to calculate lattice spacing. Since the TEM imaging of a crystal can be represented as the process of a series of Fourier transformations and inverse Fourier transformations from scattered waves from a crystal to a

diffraction pattern, the diffraction patterns can be visualized from the FFT image.

After obtaining the diffraction patterns from the FFT image, measuring the crystal lattice using FFT can be done as follows:

Input the FFT images into the ImageJ software, and determine the double lattice spacings values by measuring the distance between two symmetric diffraction points in the FFT image. In the meantime, lattice spacing will show up based on the scalebar. From Fig. 4-5, the lattice spacing values of three protein crystals can be seen, which are consistent with the results of measuring the distance between atomic layers.

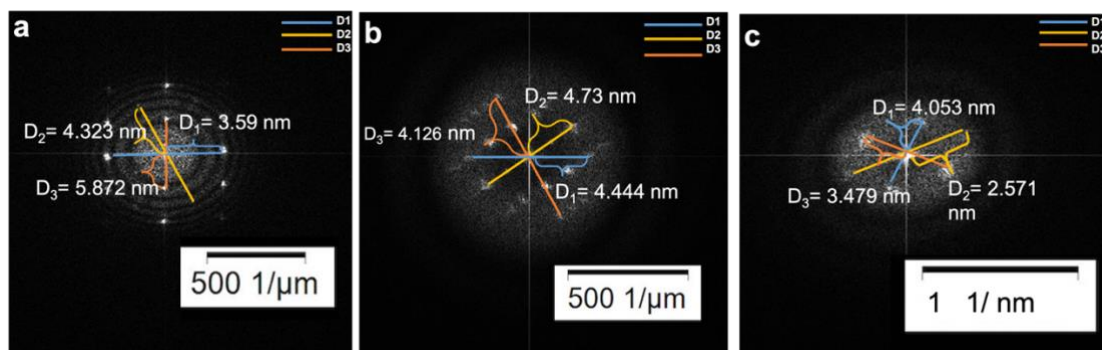


**Fig. 4-5 Determination of lattice spacing values (three protein crystals) through analyzing FFT images.**

(a) Lysozyme. (b) Thaumatin. (c) Proteinase K. The length covered by the brackets is the distance between the crystal lattice spacing.

However, salt crystals (inorganic crystals) possess much smaller unit cells than protein crystals, exhibiting much smaller lattice spacing (such as sodium chloride: approx. 0.22 nm, sodium nitrate: approx. 0.27 nm) (Zhou *et al.*, 2015; Fisher *et al.*, 2016). Therefore, TEM visualization and calculation of crystal lattice spacing allow researchers to determine whether the crystal is protein or salt.

### 4.1.3 X-ray protein powder diffraction experiments

The most direct and reliable method of distinguishing protein crystals from salt crystals is to perform X-ray diffraction. Protein crystals exhibit many closely spaced diffraction spots because protein crystals possess larger unit cells than salt crystals, which show few scattering spots.

In this study, suitable-sized crystals were not available for the single-crystal X-ray diffraction, while the X-ray powder diffraction could give basic information about the phase purity. Similar to the results of X-ray single-crystal diffraction, a beam of X-ray passing through a powder sample contains a large number of randomly-oriented crystallites and produces a pattern of rings.

Furthermore, the beam was focused on the sample with a spot size of 330  $\mu\text{m}$  and the data were accumulated for 30 mins in a single frame covering  $\Delta\phi$  of 90° in this experiment. Although the cryo-protection was not used for the nano- or micro-sized crystals protection, the strong intensive signals from the samples can also be obtained.

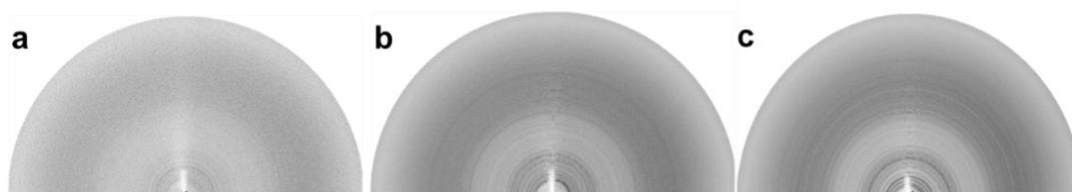


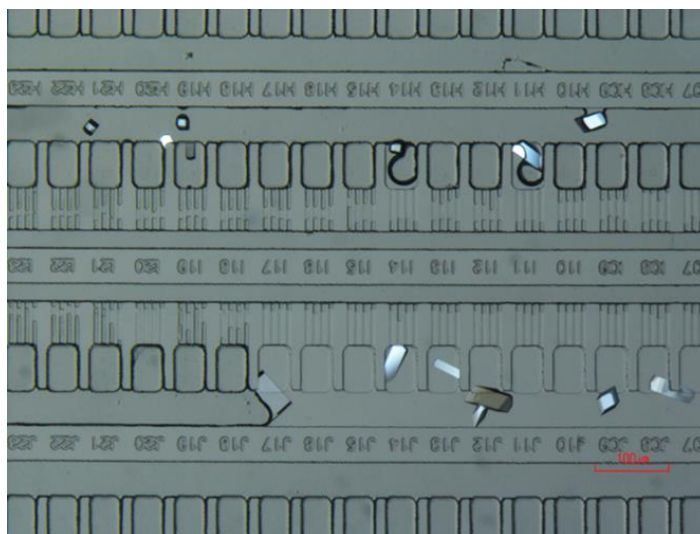
**Fig. 4-6 X-ray powder diffraction rings for lysozyme, thaumatin, and proteinase K powder.** Data were collected in 30 minutes on the 20  $\mu\text{l}$  sample mounted in a capillary.

(a) Lysozyme. (b) Thaumatin. (c) Proteinase K.

## 4.2 Imaging the *in vitro* protein crystals applying the Formulatrix SONICC and the MPM imaging systems

In this study, the PDMS microfluidic chip was chosen as the container for protein crystals. Fig. 4-7 shows lysozyme crystals with different sizes in the PDMS microfluidic chip, captured by bright-field imaging. Among these crystals, some were large, while others were in punctate shapes naked to the

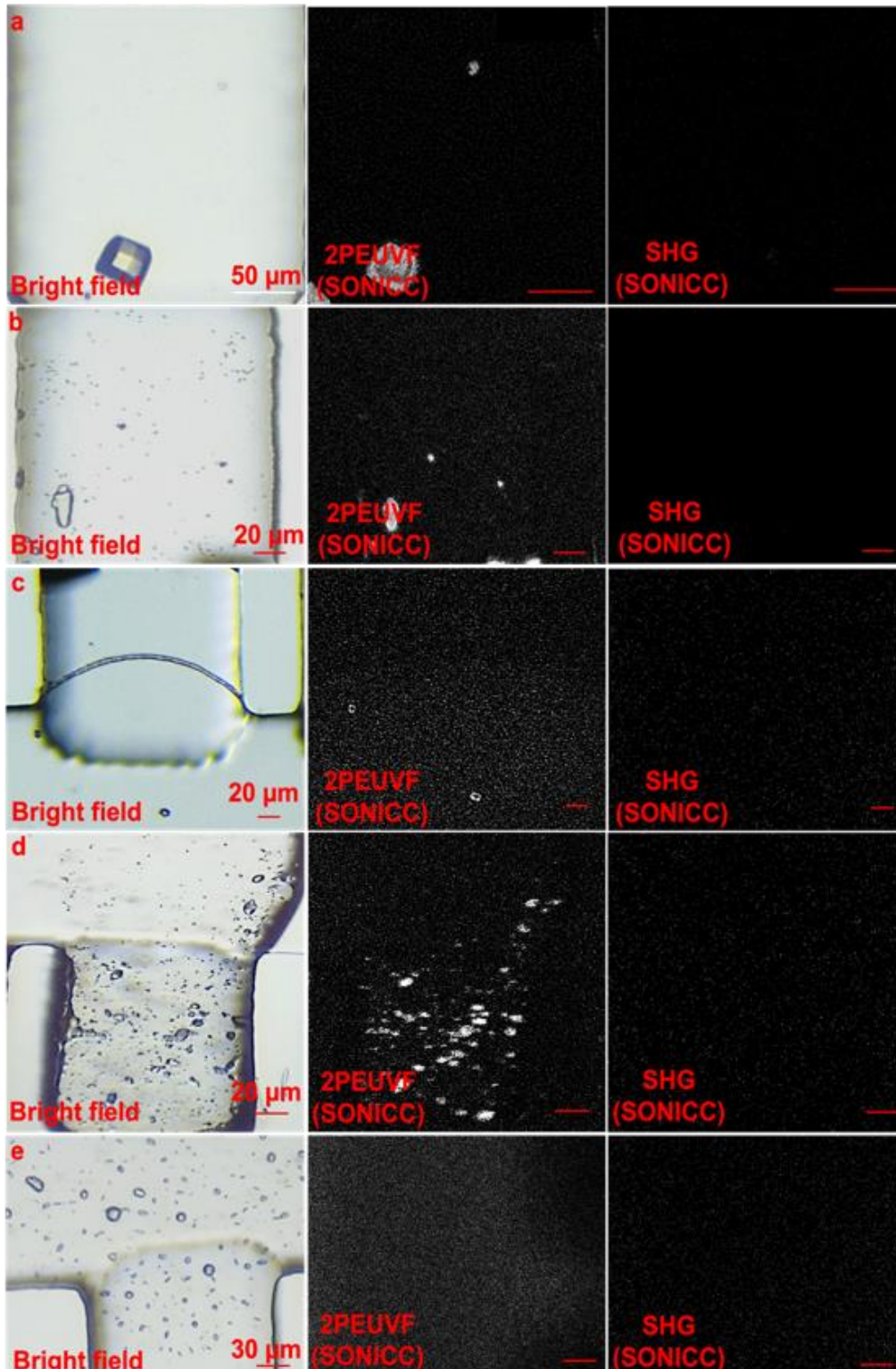
eyes. Thus, the poor reproducibility crystallization results are in accordance with the previous results.



**Fig. 4-7 Lysozyme crystals in the PDMS microfluidic chip.**

After obtaining crystals from the PDMS chip, a variety of protein crystal samples with different space groups were measured by different imaging systems. In Fig 4-8 (a-e), no SHG signals of lysozyme crystals (space group:  $P4_32_12$ ), thaumatin crystals (space group:  $P4_12_12$ ), and thermolysin crystals (space group:  $P6_122$ ) are identified, which demonstrates that nano- or micro-sized protein crystals in higher symmetry cannot be detected when applying SONICC and MPM systems. Moreover, the 2PEUVF signal of smaller lysozyme crystals was very weak, and only bigger crystals could produce relatively stronger signals. As shown in Figs. 4-8 (f-j), the SHG signals of those crystals can be detected when applying the MPM system. Smaller protein crystals were visible using 3PEUVF and SHG modalities of the in-house MPM instrument. Besides the measurement of protein crystals with higher space groups, a variety of different protein crystals with lower space groups were selected for the imaging experiments, as listed in Figs. 4-9 (a-d), which shows the results of SHG and UV imaging experiments for glucose isomerase, bovine serum albumin, insulin, and lactamase applying the in-house developed MPM imaging system. Moreover, as shown in Fig. 4-9a and 4-9b, the SHG and THG signals for bovine serum albumin and insulin crystals don't

fully overlay with each other, whereas SHG signals overlap with 3PEUVF signals. This indicates that the samples contained protein crystals (SHG and 3PEUVF are positive), as well as amorphous particles (THG is positive and SHG is negative).



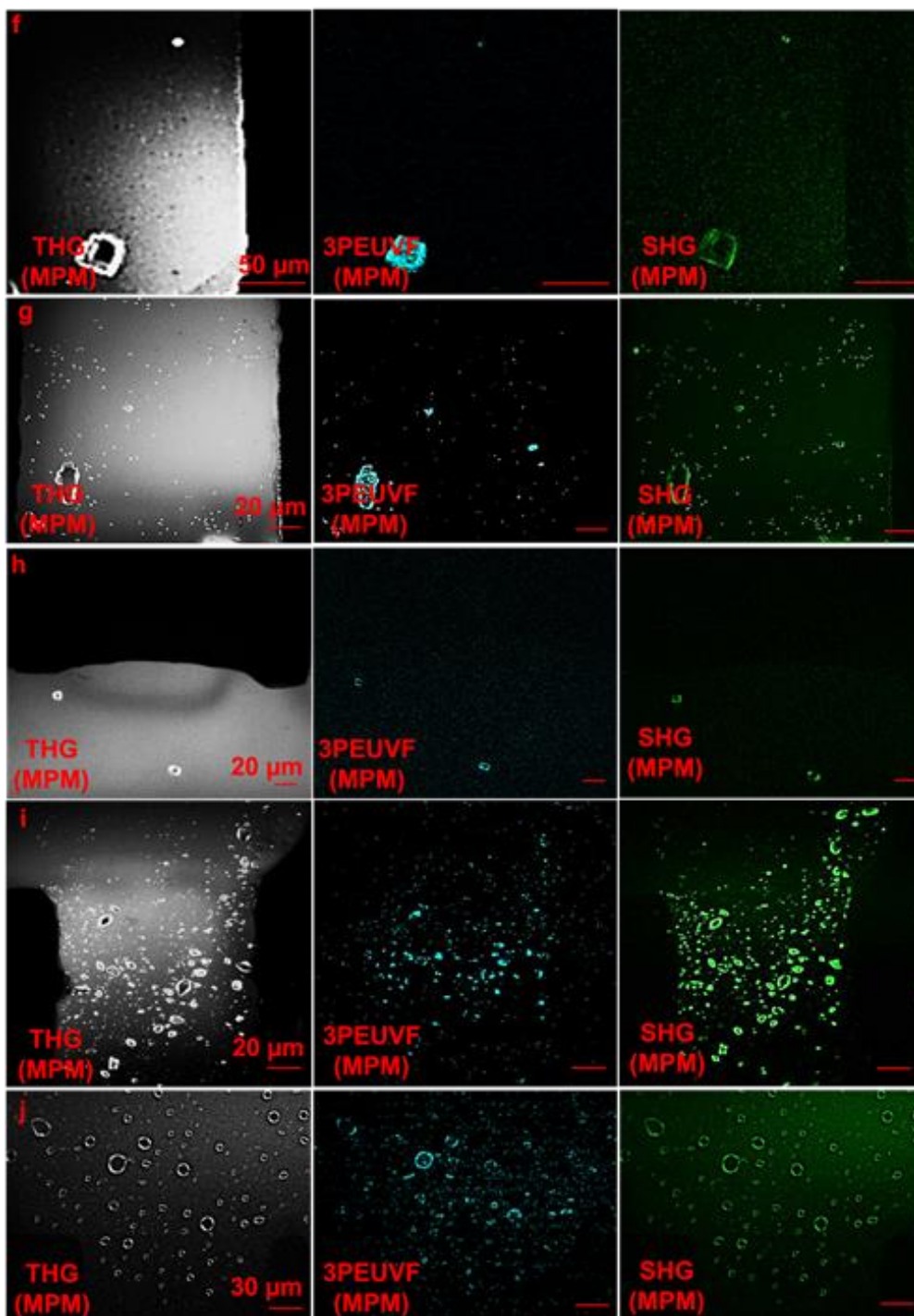


**Fig. 4-8 Images of different protein crystals.**

(a)–(e) SONICC imaging of a large lysozyme crystal, micro-sized lysozyme crystals, micro-sized proteinase K crystals, micro-sized thaumatin crystals and micro-sized thermolysin crystals. (f)–(j) MPM imaging methods for lysozyme crystals, micro-sized lysozyme crystals, micro-sized proteinase K crystals, micro-sized thaumatin crystals and micro-sized thermolysin crystals.

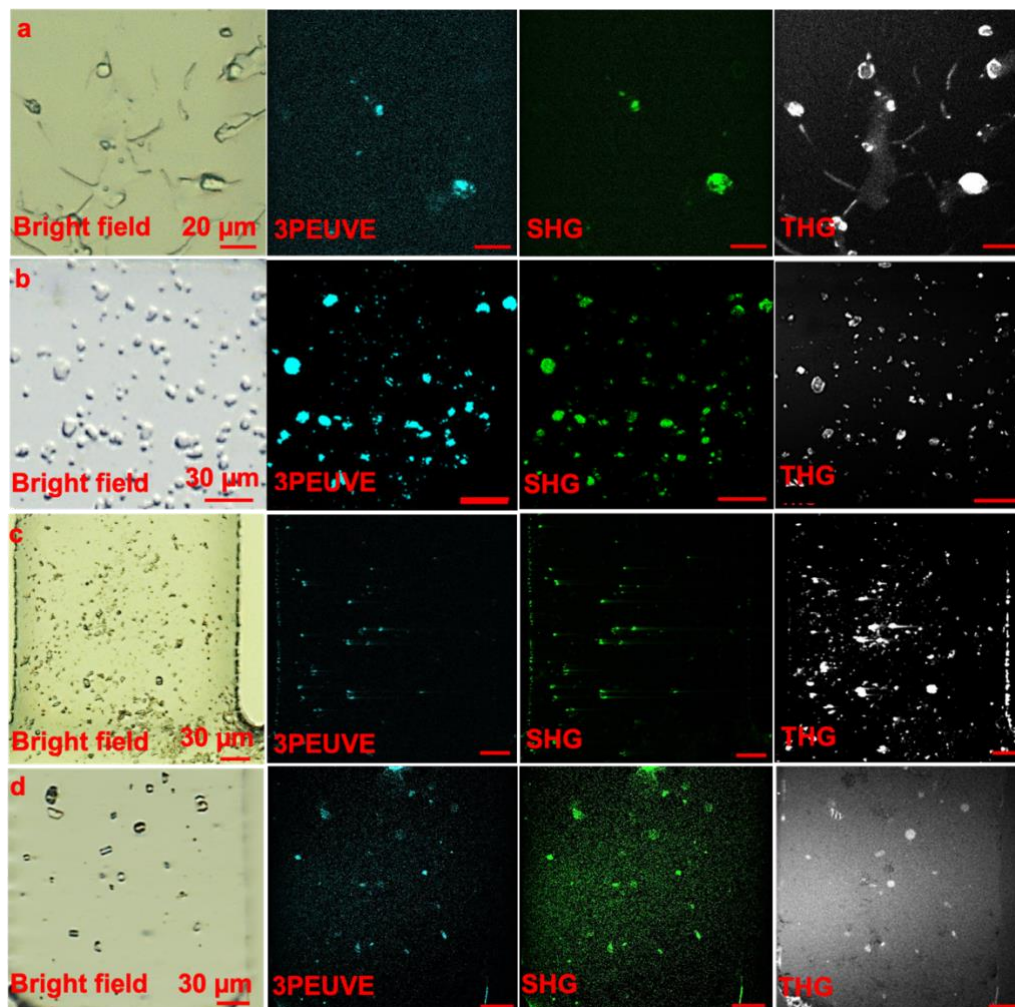


**Fig. 4-9 Images recorded for different protein crystals applying the MPM system.**

The method of detection and imaging is indicated in the lower left of each image. (a)-(d) MPM imaging of glucose isomerase, bovine serum albumin, insulin and lactamase. THG imaging is not tied to the condition of high symmetry, thus, the THG imaging can be considered as an excellent complementary method to bright-field, SHG and UV imaging. The overlapping parts of SHG and UV imaging can reveal the protein crystals.

### **4.3 Imaging the *in vivo* protein crystals applying the MPM imaging system**

In this part of the study, two different cells, along with protein crystals of different sizes, were selected for the MPM imaging. Under an ordinary optic microscope, some larger-sized protein crystals were easily observed. From Fig. 4-10, needle-like protein crystals can be easily observed. Many of the

crystals pierced through the cell membranes, altering the shape of the cells. The reason for choosing this type of crystal sample was to test whether the MPM could detect these crystals under the cell membrane. The light microscopic image shows that *Sf9* insect cells contain *in vivo* crystals, most of which protrude from cells.

However, in Fig. 4-11 where the standard optical microscopy was used, confirming whether there are crystals in the cells only by analyzing the unsmooth cell surface is difficult. Thus, these samples were selected to test the availability of MPM.

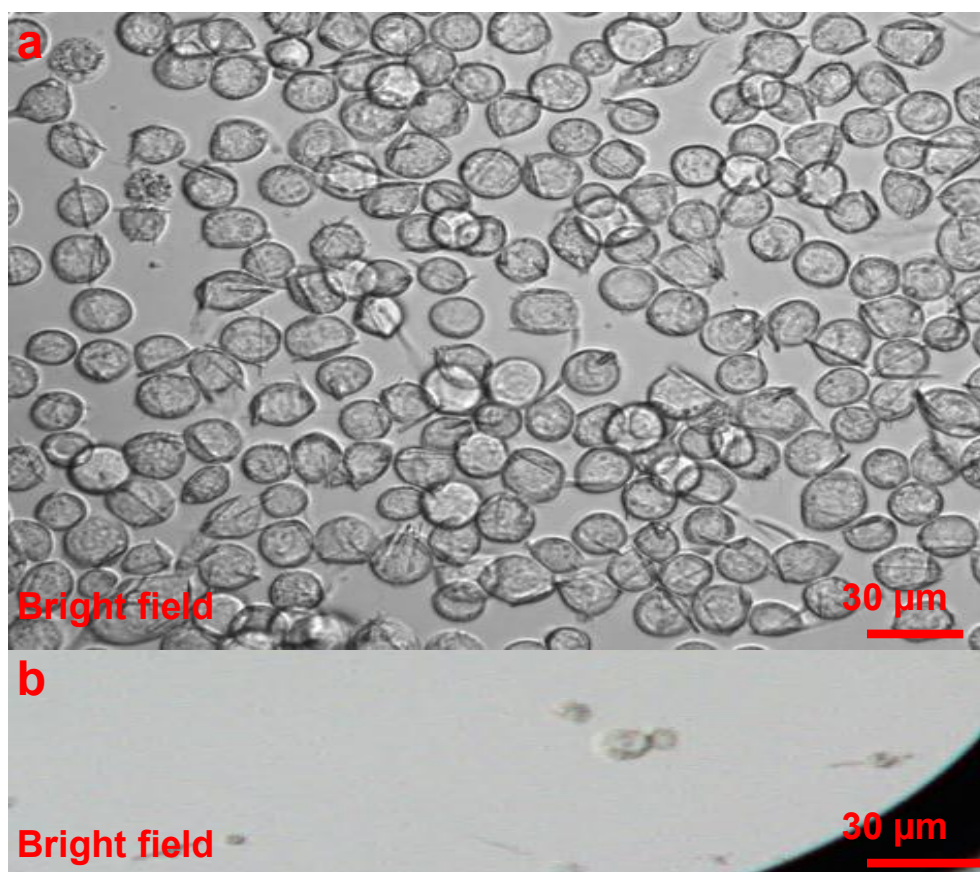


**Fig. 4-10 Images of *in vivo* protein crystals.**

(a) *In vivo* grown protein crystals of IMPDH (insect cells). (b) *In vivo* grown protein crystals of PAK4-inka (insect cells). Light microscopic image showing *Sf9* insect cells containing *in vivo* crystals. Most of them protrude from cells.

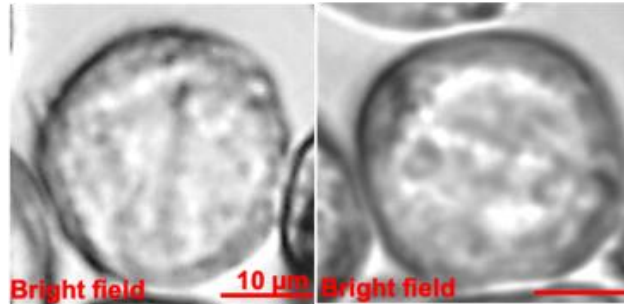


**Fig. 4-11 *In vivo* crystals of PAK4 (insect cells).** Bright-field images showing that *Sf9* cell membrane outlining the need-like objects. The scale bar corresponds to 10  $\mu\text{m}$ .

Fig. 4-12 shows *in vivo* protein crystals of different sizes. Specifically, some larger crystals were approximately 50  $\mu\text{m}$  in size and would penetrate the cell membrane surface if they continued to grow. They could also be easily identified under a high-resolution optical microscope and distinguished after being separated from the cells, directly used as a diffraction sample. As shown in Fig. 4-12, the needle-like crystals with a much larger size than that of the cells reflected perfect imaging results in the MPM system.

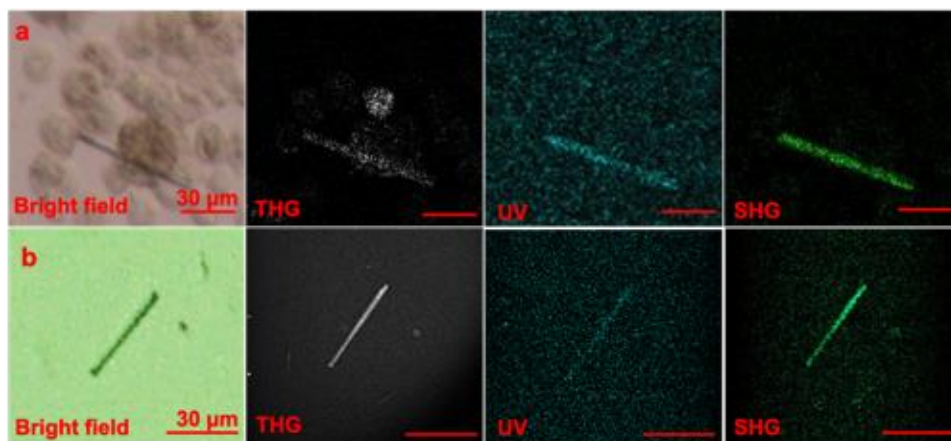


**Fig. 4-12 Images of *in vivo* protein crystals selected for the imaging experiments (mammalian cells).**

(a) *In vivo* grown protein crystals of PAK4. (b) Isolated crystals of PAK4. In Fig. 4-12a, THG imaging reveals the outline of needle-like crystals, as well as the weak signal from the cell membrane, SHG and UV imaging also confirm the presence of the needle-like protein crystals. In addition, neither SHG nor UV signals from the cell membrane.

Moreover, THG imaging results clearly presented the contours of cells and needle-like crystals. For example, as shown in Fig. 4-13, smaller crystals might exist in the cell. However, in bright-field images, determining the presence of protein crystals by just observing the surface morphology of the cell membrane would be difficult. By contrast, the position and morphology of the potential protein crystal could be detected from the THG imaging results, as shown in Fig. 4-13a, Fig. 4-13b, and Fig. 4-13c. The signals of SHG and UV also confirmed the existence of protein crystals, and no cell membrane interference was observed in the SHG signals. Notably, these three samples in were easy to find as no SHG signal from the cell membrane was found, but a weak UV signal from the cell membrane was identified.

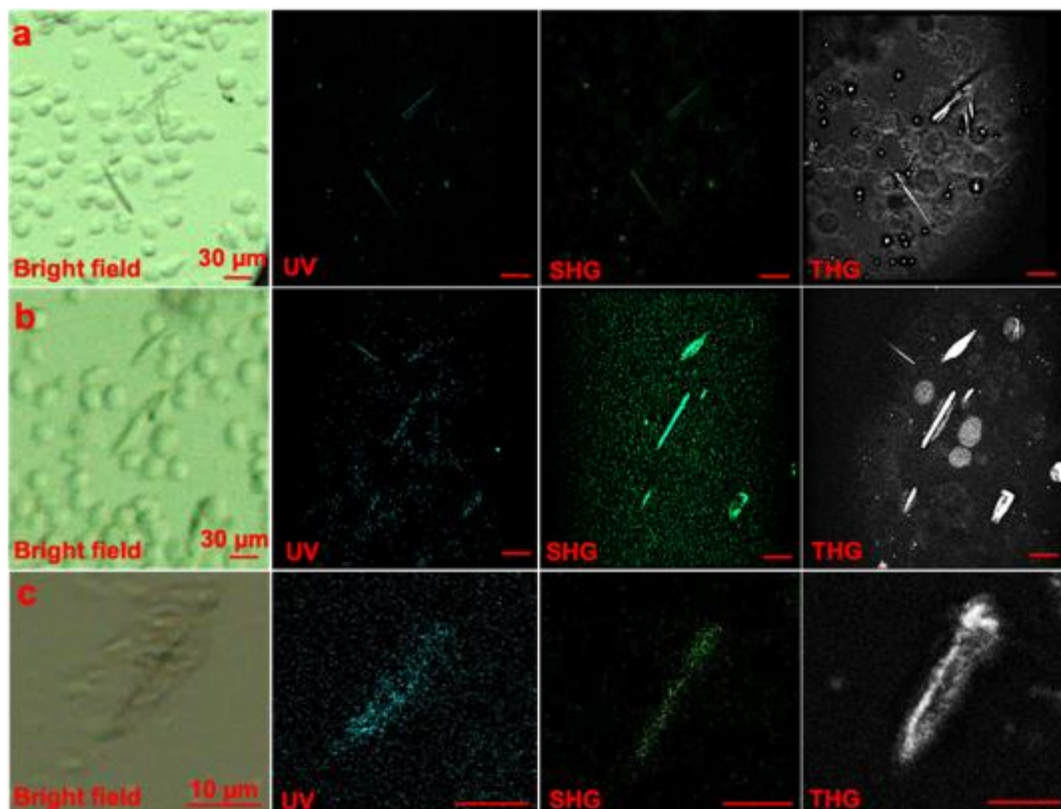


**Fig. 4-13 Images of *in vivo* protein crystals for the imaging experiments (insect cells).**

(a) *In vivo* grown protein crystal of PAK4. (b) *In vivo* grown protein crystal of PAK4-GFP. (c) *In vivo* grown protein crystal of IMPDH.

From Fig. 4-13a and Fig. 4-13b, nano-sized crystalline particles can be detected but cannot be observed from bright-field imaging. The high contrast

background contributed to the visualization of the sample that could be ignored by bright-field imaging. However, in Fig. 4-13b and Fig. 4-13c, UV images show weak signals from the cell membrane.

Despite those positive results in Fig. 4-13, not all of the experimental results reflected good outcomes. In Fig. 4-14, a weak SHG signal can be observed. However, whether this originated from the early stage of protein crystal growth or other substances with non-centrosymmetric structures cannot be judged from the morphology. Furthermore, in Fig. 4-15, the bright-field imaging shows that the cell lost its original morphology. Unlike normal cells, these cells were likely to enter a dead state. The visibility of crystals was seriously affected by the SHG signal generated from the cell membrane as the SHG signal from the cell membrane might cover the SHG signal of the crystals in the cell. The strong SHG signal indicates that the detected substance is different from the normal cell state. Therefore, from these results, changes in cells affect the stability of the internal structure of the cells.

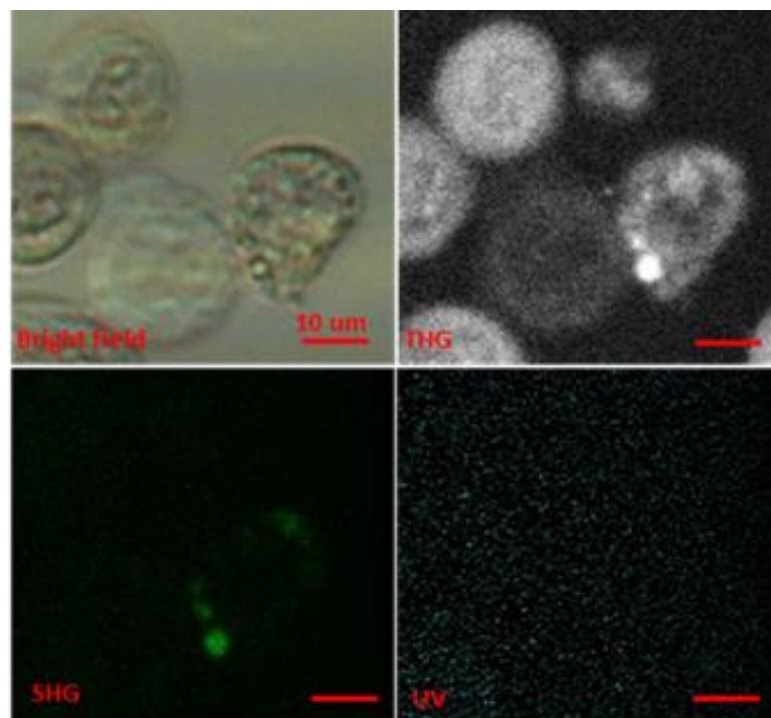


**Fig. 4-14 Images of *in vivo* crystals of PAK4-inca (insect cells).** In Fig. 4-14, THG imaging shows that the strong signals from both the cell membrane and some particles, but weak SHG signals UV signals from particles.

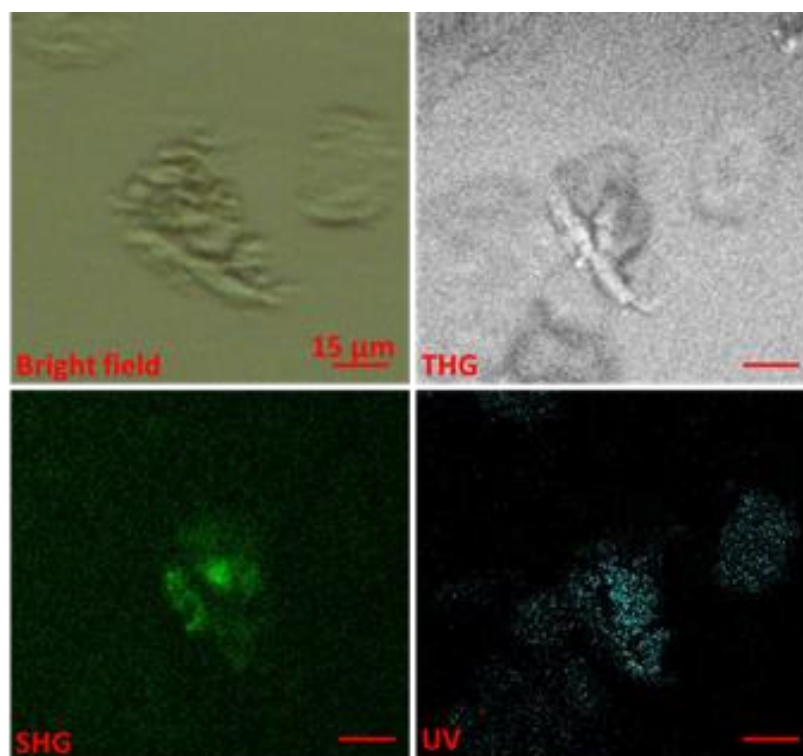


**Fig. 4-15 Images of *in vivo* crystals of PAK4-inca (mammalian cells).**

The cell lost its normal morphology, and the only needle-shaped object can be observed from the bright-field imaging and THG imaging. SHG and UV images show a obscure outline and thus it is difficult to identify whether it is a crystal.

#### 4.4 Summary and discussions

In summary, the in-house MPM instrument exhibited a particularly high detection sensitivity, allowing SHG detection of micro-sized protein crystals. The system was very versatile with respect to the changes in the optical design and the used sample container, allowing nano- or micro-sized protein crystal identification. Notably, using the in-house MPM imaging system for the detection of lysozyme, thaumatin, proteinase K, thermolysin, glucose isomerase, bovine serum albumin, insulin and lactamase crystals was profound. The imaging results of thaumatin, proteinase K, and thermolysin crystals, growing in a higher symmetry space group ( $P4_32_12$ ,  $P4_12_12$ ,  $P6_122$ ),

demonstrated a high detection sensitivity of the MPM instrument for micro-sized crystals of these space groups. As shown in the detection results of bovine serum albumin and insulin crystals, the SHG and THG signals did not fully overlay with each other, whereas SHG signals overlaid with 3PEUVF signals. That is to say, the samples contain protein crystals (SHG und 3PEUVF positive) as well as amorphous particles (THG positive, SHG negative). Furthermore, it could be easier to detect nano- or micro-sized lysozyme, thaumatin, proteinase K, and thermolysin crystals through the newly developed MPM instrument as the MPM imaging system reduced the risk of false-negative results in crystal detection by providing a higher signal and a tunable polarization of the excitation.

In addition to the detection of protein crystals outside the cell, the MPM imaging system could also be applied to the detection of protein crystals in the cells. The experimental results showed that different types of cell membranes did not generate SHG signals but significantly reduced the interference caused by false-positive SHG signals. However, there were still some limitations caused by complicated intracellular situations. In Fig. 4-13 and Fig. 4-14, the SHG signals appeared but whether they are protein crystals cannot be confirmed. The SHG signals might come from the non-centrosymmetric substances in the cells. The details are discussed in section 4.4.4.

#### **4.4.1 Complementary methods**

Following the MPM measurement, three samples were investigated by using DLS, DDLS, TEM imaging, and X-ray powder diffraction. According to DLS measurements, granular particles with a size of a few micrometers were found in the samples of lysozyme, thaumatin, and proteinase K (Fig. 4-2). However, each method has its own advantages and disadvantages. The fact that DLS data cannot be used to visualize and identify protein crystals because the DLS method cannot distinguish crystals from amorphous demonstrates the necessity of additional complementary methods (such as DDLS, TEM). Nevertheless, DDLS can distinguish crystals but cannot distinguish the protein crystal from the salt crystal. Thus, two more reliable methods were applied by TEM imaging and X-ray powder diffraction. The TEM images of lysozyme,

thaumatin, and proteinase K crystals provided evidence that crystals of a nano- or micro-size have grown during the DLS and DDLS experiments. Since TEM imaging allows the visualization of lattices and the calculation of lattice spacing, the protein crystal can be identified after comparing its lattice spacing with that of the salt crystal (the lattice spacing of salt crystal is much smaller). Although TEM can detect protein crystals of a smaller size than MPM imaging systems and can obtain more specific crystal information (such as lattice spacing, crystal defects), high-resolution TEM images require ultra-thin crystal samples, which are not easy to prepare. Besides, researchers often spend a lot of time on TEM observations to identify and detect a large number of protein crystal samples. Consequently, compared to the MPM imaging system, the TEM cannot perform high-throughput protein crystals detection as quickly as MPM imaging systems.

As for the X-ray powder diffraction results, the strong powder diffraction pattern recorded from three samples confirmed that these three samples contained nano- or micro-sized protein crystals, which is in accordance with the results of the DLS, DDLS, and TEM imaging experiments.

In a word, although the DLS and DDLS methods can provide valuable information in the early stage of nucleation to help optimize the crystallization condition, they cannot distinguish protein crystals from salt crystals. TEM is a more powerful imaging tool for identifying nano- or micro-sized protein crystals than the MPM system and can evaluate the diffraction quality. However, the detection performance of TEM depends on the sample preparation, as the thick crystal sample could restrict the observation and visualization of lattice fringes to a low resolution. As for the X-ray powder diffraction, since the diffraction measurement relies on the sample size, a small crystal sample could limit the number of crystallites that contribute to the measurement.

#### **4.4.2 Imaging methods of the SONICC and MPM systems**

The characteristics of various imaging methods of identifying protein crystals, as well as their applications, were introduced (in the introduction part). THG, SHG, and three-photon UV-fluorescence imaging methods were selected based on the requirements for protein crystal detection. The detection process

of the MPM system for protein crystals is similar to the detection process of the SONICC system, as is presented in Fig. 4-15, which shows that these two imaging systems possess SHG imaging and UV imaging. The only difference is that the MPM system adopts THG imaging instead of bright-field imaging.

Then the assessment of these two imaging systems' imaging methods is presented. Two-photon UV imaging is similar to three-photon UV imaging, and both methods were used to identify protein crystals.

THG imaging of the MPM system and Bright-field imaging of the SONICC system

Firstly, the function of THG imaging in the MPM system is similar to that of bright-field imaging in the SONICC system. Originating from optical inhomogeneity, THG signal can be found at the interface between solvent and protein aggregates, as well as protein crystals. By contrast, bright-field imaging relies on the light absorption of different structures and, therefore, cannot effectively identify the colorless protein crystal due to the low contrast of most protein crystals. Taking the detection of *in vitro* protein crystals as an example, as shown in Fig. 3-18, the identification of the tiny crystal covered by salt crystals is difficult for bright-field imaging, whereas THG imaging can easily observe the tiny crystal. Also, images in Fig. 4-7 and Fig. 4-8 reveal that THG imaging can be used as an excellent method complementary to bright-field imaging in the detection of *in vitro* protein crystals. Even in *in vivo* protein crystal detection, THG imaging can discover the micro-sized protein crystals covered by the cell membrane.

Three-photon UV imaging of the MPM system and two-photon UV imaging of the SONICC system

Secondly, UV-light signals are applicable to the detection of the presence of protein samples. The MPM system performs three-photon UV imaging, while the SONICC performs two-photon UV imaging. Compared with one-photon (1P) or 2P excitation, 3P excitation has several advantages such as a decrease in the light scattering effect due to the use of longer wavelengths and an increase in the penetration depth of the illumination beam into the

sample. Moreover, the nonlinear nature of the process confines the excitation to a smaller volume, reducing photo-bleaching on the biological sample.

#### SHG imaging of the MPM and SONICC systems

Finally, both of these two imaging systems perform SHG imaging to detect non-centrosymmetric crystals. The protein crystal is detected through the overlapping part of the UV signal and the SHG signal. Unlike THG imaging, which is not limited when detecting crystals in higher symmetries, SHG is rather weak in crystals with high centrosymmetric structures (Lüpke *et al.*, 1994). In contrast to the commercial SONICC system, the MPM system adopting the SHG imaging exhibits a higher signal sensitivity when detecting nano- or micro-sized protein crystals (in Fig. 3-18).

However, one central question remains to be addressed: what causes higher signal sensitivity when detecting nano- or micro-sized protein crystals?

Different parameters of the MPM and SONICC systems are discussed in section 4.4.3.

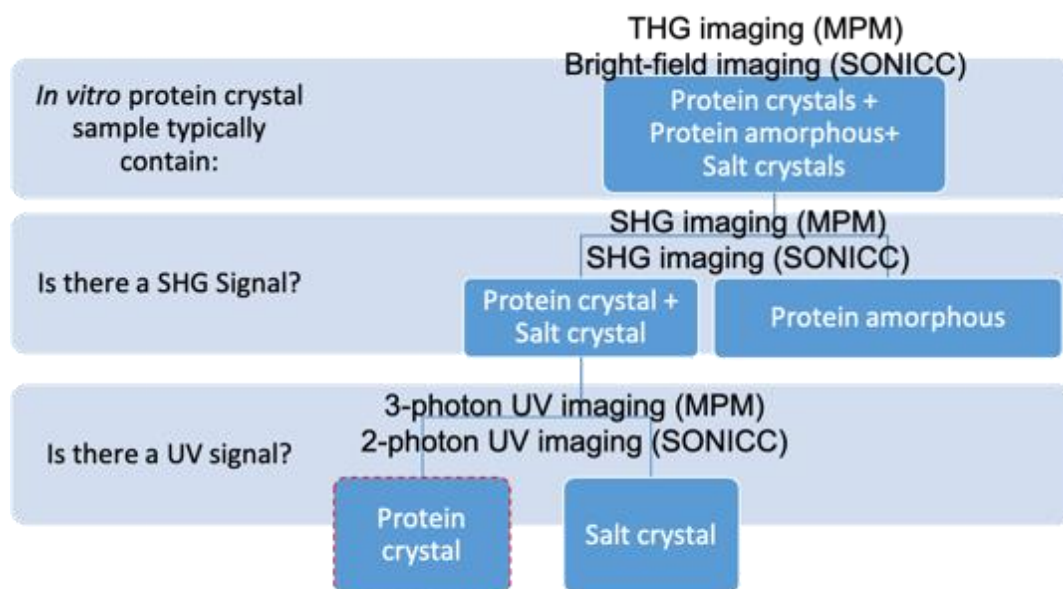


**Fig. 4-16 Detection process for protein crystal applying the MPM system and the SONICC system.**

#### 4.4.3 Parameters of the SONICC and MPM systems

The parameters of the commercial SONICC system and the MPM system are provided below in Table 4-1. The laser of the SONICC system operated at a repetition rate of 80 MHz with a pulse duration of 200 fs and the average power ranged from 100 mW to 1 W after the objective lens. The frequency of the laser wavelength was doubled from near-infrared (near-IR) at 1064nm with a nonlinear optical (NLO) crystal to green at 532 nm, which is the sample imaging light source. The equivalent two-photon absorption wavelength of the green was 266 nm, which can excite tryptophan amino acids. The two-photon excited fluorescence (350 – 400 nm) was collected and then applied to display the fluorescence image. In addition, the NA of the optical system was 0.51.

Compared with the laser of the SONICC system, the laser of the MPM operated at a repetition rate of 31 MHz and generated 290 fs pulses centered with a pulse energy of up to 160 nJ, which corresponds to an output power of 5 W, after dechirping. The pulse energies for 1300 nm and 775 nm are approximately 10 nJ, which corresponds to 300-mW average power, after the wavelength conversion. The excitation power after the objective reached up to 60 mW for both wavelengths (corresponding to ~2-nJ pulse energy). The pulse duration for 1300-nm pulses was ~95 fs after the objective. For 775 nm, the pulse duration before the microscope was 190 fs and estimated to be >200 fs after the objective. In addition, the NA of the optical system was 1.05.

The performance of the MPM and SONICC systems is determined by six parameters of the ultrafast light source: pulse energy  $E_p$ , pulse duration  $\tau$ , repetition rate  $f$ , average power  $P_0$ , peak power  $P_p$ , and excitation wavelength  $\lambda$ . The laser pulse parameters (pulse energy  $E_p$ , pulse duration  $\tau$ , repetition rate  $f$ ) are shown in Fig. 4-17.

The relationship between the three laser pulse parameters (pulse energy  $E_p$ , pulse duration  $\tau$ , repetition rate  $f$ ) is illustrated in the following equations:

Pulse energy depends on the average power (4-1):

$$E_p = P_0 / f \quad (4-1)$$

Peak power  $P_p$  in a laser pulse is limited by the pulse energy  $E_p$  and the pulse duration  $\tau$ , which can be defined as the Equation (4-2):

$$P_p = E_p / \tau \quad (4-2)$$

This can also be defined as the Equation (4-3):

$$P_p = \frac{P_0}{\tau \times f} \quad (4-3)$$

From the Equations (4-1) and (4-2), the pulse duration determines both the pulse energy and the average energy, which increase or decrease as the pulse duration increases or decreases. From the Equations (4-2) and (4-3), at the same excitation power, the peak power is higher due to a lower laser repetition rate and a lower pulse duration. Since the intensity of the emitted nonlinear signal highly relies on the peak power of the pulse energy, a higher pulse energy and a lower repetition rate are necessary. However, due to the risk of photodamage or photobleaching in the biological sample, the laser power/pulse energy should be controlled within a moderate value. To achieve a fine imaging contrast, the pulse energy required at the objective focus is at nJ, a low repetition rate ( $\sim 1$  MHz) operated is needed, and the pulse duration after the objective should be  $\sim 100$  fs (Chung *et al.*, 2019b).

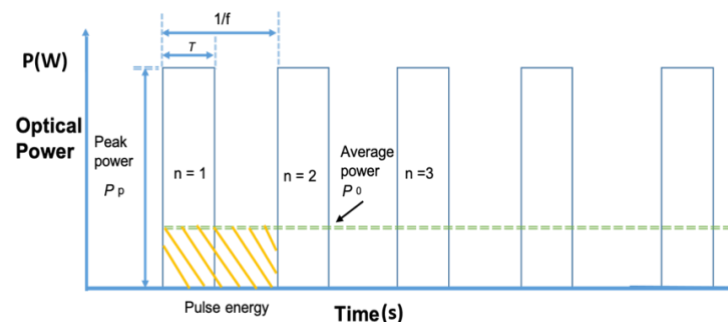


**Fig. 4-17 Parameters of the laser pulse.** Pulse energy refers to a measure of the emission over one period as shown in the shaded regions. Repetition rate is the frequency with which pulses are emitted, being equal to the reciprocal of the period. Pulse duration represents a measure of the time from the beginning to the end of the pulse. Average power means the average power output by the pulsed laser, being equivalent to the area covered by diagonal hash marks. Peak power is the maximum instantaneous optical power output by the laser.

Additionally, the selection of the excitation wavelength is vitally important for the performance of the SONICC and MPM systems as the loss of nonlinear signals is highly wavelength dependent.

The amount of the nonlinear signal loss between the input and the output is known as attenuation, which contains the scattering effect and the absorption effect during transmissions. In general, the scattering effect of samples decreases as the wavelength increases, while the absorption effect can differ from sample to sample.

Despite the fact that the excitation of higher generation (HG) exhibits no such wavelength selectivity, the application of a longer wavelength (i.e., >1200 nm for THG, and >800 nm for SHG) is still required. This is because the resulting HG falling within the range of visible light can be efficiently detected and suffers less optical attenuation.

After selecting the relatively longer wavelength region for HG imaging (wavelength >1200 nm), the absorption effect of the different sample must be taken into consideration. As for the absorption effect, due to the existence of water and protein, biological sample (protein crystal) absorption reduces signal intensity. Notably, the main absorption effects of the biological sample arise from water, which accounts for 50-80% of a biological sample (Kou *et al.*, 1993). Therefore, to decrease the loss of signals through biological samples, using a long wavelength is necessary.

In Fig. 4-18, for example, all samples (including water and protein) reach the minimum value in the region of 1300 nm (between 1200 nm-1500 nm). Hence, THG and SHG imaging (1300nm) can exhibit a high-sensitivity and high-contrast imaging feature.

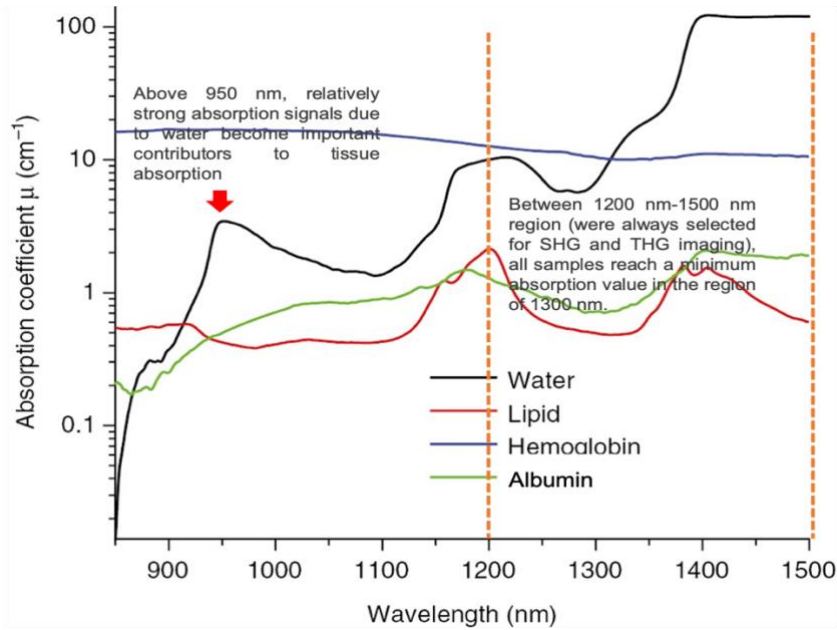


**Fig. 4-18.** Different absorption spectra of water, lipids, hemoglobin, and albumin. The red arrow indicates the maximum absorption value from water between 850 nm-1200 nm. Orange dash lines indicate the wavelength region between 1200 nm-1500 nm, which is suitable for high generation imaging (Modified from Cao *et al.*, 2013).

**Table 4-1** Parameters of the SONICC and the MPM system.

	SONICC	MPM System
Laser repetition rate	80 MHz	31 MHz
Objective NA	0.51	1.05
Pulse duration	200 fs	100-200 fs
Maximum FOV	0.65 x 0.65 mm <sup>2</sup>	0.8x 0.8 mm <sup>2</sup>
Excitation wavelength	1064 nm	1550 nm and 1300 nm

As discussed above, the in-house developed MPM system has the following advantages over the commercial SONICC system:

1. Reducing the pulse duration while maintaining the same average power can improve nonlinear optical imaging signals.

2. The pulse energy and peak power are higher while keeping the same excitation power due to a lower laser repetition rate.
3. A higher NA of the objective lens allows a smaller focus with a higher laser beam intensity, thus enabling the improvement of the nonlinear intensity.
4. In addition, using objectives with a higher NA improves the optical resolution.
5. The attenuation rate of the nonlinear signal is associated with the excitation wavelength – the longer the wavelength is, the less the attenuation and the higher the intensity signal will be.

Notably, for nano- or micro-sized crystal imaging, the SHG intensity scale with the square of the peak intensity, or equivalently with the fourth power of the NA (Hauptert *et al.*, 2012). Those advantages (the short pulse duration, the higher peak power based on the lower laser repetition rate, the higher NA, and the longer wavelength) mentioned in Table 4-1 prove that the MPM system improves the SHG detection sensitivity.

#### **4.4.4 *In vitro* protein crystal and *in vivo* protein crystal detection**

The different detection results of *in vitro* protein crystals in the MPM system and SONICC systems were discussed in the last section.

In addition to the detection of *in vitro* protein crystals, MPM-imaging can also be applied to the detection of protein crystals within the cell to some extent. In this work, two different types of cells were used: insect cells and mammalian cells. The experimental results demonstrate that these two types of cell membrane will not generate SHG signals and thus significantly reduce the interference caused by false-positive SHG signals (As shown in Fig. 4-11 and Fig. 4-12). From Fig. 4-11, these three imaging methods are able to identify protein crystals that can even be easily ignored by bright-field imaging. Notably, the UV imaging not only showed the outlines of protein crystals but also presented the obscure outlines of the cell membrane. However, not all the results of *in vivo* protein crystal detection are perfect, as shown in Fig. 4-15 and Fig. 4-14.

Based on those imperfect results, this section draws upon the composition of *in vivo* protein crystals and the cell death to conduct the analysis.

The composition of protein crystal samples in cells is more complex than *in vitro* protein crystallization because of different growth methods and conditions. As shown in Table 4-2, compared with *in vitro* protein crystal samples, *in vivo* protein crystal samples contain not only protein crystals covered by the cell membrane but also cytoskeleton, genetic material, and organelles. As a result, SHG and UV signals may originate from protein crystals or other substances in the cell (Campagnola *et al.*, 1999).

Previous studies have shown that SHG signals can hardly be detected from cell membranes even when they are non-centrosymmetric (SHG-active). Besides, SHG imaging can be used to visualize collagen fibers, membranes, and cytoskeleton microtubules in cells. In this work, abnormal cell morphology was caused by membrane rupture as shown in Fig. 4-14. The strong SHG signals may originate from the non-centrosymmetric materials in the cells, such as collagen fibers, membranes, and cytoskeleton microtubules. In addition, SHG is also used as a tool for assessing membrane damage with the aid of dye (Brown *et al.*, 2003; Van Steenberg *et al.*, 2019; Kyrychenko, 2015).

The experimental results show that this abnormal cell state leads to the membrane breakdown, the main reason for which is cell death, a biological process of cells resulting from the natural aging process of old cells or the death of the organism. One of the main functions of a normal cell membrane is preventing injury from the extracellular matrix, thus maintaining the original state of the cell. Cell death leads to characteristic cell changes (morphology), which include cell shrinkage, membrane rupture, and blebbing, and is now known to be classified into main two types: apoptosis and necrosis, which can be identified according to morphological characteristics. Apoptosis occurs in multicellular organisms with morphological changes in different phases, including cell blebbing (Ziegler & Groscurth 2004; Coleman *et al.*, 2001; Sebbagh *et al.*, 2001), the formation of membrane protrusions, and

fragmentation (Moss *et al.* 2006; Poon *et al.*, 2014; Atkin-Smith *et al.*, 2015; Tixeira *et al.*, 2017). Finally, cells break into several apoptotic bodies.

Similar to apoptosis, necrosis leads to structural changes in cells, including the formation of small blebs, disruption of genetic material, and disruption to the membranes of cells. In the end, the cell membrane ruptures and releases the cell's contents. Furthermore, decomposed substances, such as chromatin fibers, DNA fragments, and cytoskeleton are exposed to the external cellular environment. These non-centrosymmetric substances may generate SHG signals, as well as cytoskeleton on damaged cell membranes.

**Table 4-2** Differences between *in vitro* and *in vivo* protein crystal.

	<i>In vitro</i> protein crystals	<i>In vivo</i> protein crystals (Eukaryotic)
Growth methods	Microbatch, hanging drop, sitting drop, microdialysis, free-interface diffusion, containerless.	Incubate in cells
Sample contains	Protein crystals, salt crystals, and amorphous	Protein crystals, cell membrane, cytoskeleton, genetic material, and organelles.

## 5 Conclusion and outlook

In this work, the design and selected applications of a novel MPM instrument are described. The in-house MPM designed and conducted in collaboration with the group of Prof. Kärtner contains various modalities, e.g., MPEF and HGM, which are available for protein nano- and micro-crystals imaging and characterization. The instrument allows for the differentiation between amorphous and crystalline particles and extends the application of the SHG technique to even smaller particles than those which could be identified previously. By combining SHG, THG, and three-photon excited UV-fluorescence in one system, the system provides complementary information about crystalline sample suspension to be used for future diffraction.

This system is the first to combine THG, SHG, and three-photon UV imaging methods to detect the presence of nano- or micro-sized protein crystals.

This study is also the first comparative analysis of nano- or micro-sized protein and salt crystals with different space groups, and the first investigation of *in vivo* crystals applying three different imaging methods.

With the measurements of *in vitro* and *in vivo* grown protein crystals, the results demonstrated that the in-house MPM system exhibits a particularly high sensitivity for SHG detection of nano and micro-sized protein crystals with high symmetries. The system is very versatile with respect to changes to different sample containers, and the system allows crystal identification with less risk of false-negative results. As for the *in vivo* protein crystal detection, MPM-imaging can also be applied to detect protein crystals in cells. With regard to salt crystals, most of the salt crystals are centrosymmetric, and no SHG signals can be observed. In this study, the weak SHG signals from centrosymmetric crystals (such as NaCl and KCl crystals) originated from the surfaces. In general, the MPM system works better for the investigation of *in vitro* protein crystals. Although preliminary studies of *in vivo* protein crystal detection by the MPM system are encouraging, the technique is still in its infancy. Thus, a series of *in vivo* protein crystal imaging experiments should proceed with the following perspectives.

To better understand the advantages and limitations of the MPM system for *in vivo* protein crystal detection, additional testing and measurement should be implemented. The first step is to prepare cells in various phases since each phase of the cell reflects internal changes in cells. These specific changes in the cells may exert an influence on the performance of nonlinear optical imaging. Next, it is also necessary to observe and record the THG, SHG and three-photon UV imaging response from them for the purpose of determining whether the changes of cells in different states will influence the response of these imaging methods.

Besides, an experimental search for *in vivo* protein crystals optimum wavelength should be performed. It is necessary to measure and select which excitation wavelength is suitable to detect the target sample.

Biological samples have a very complex and dynamic structure. When studying dynamic activities, researchers often hope to maintain the integrity of the structure and function of biological samples as much as possible, so non-invasive live imaging has become a hot spot. For biological sample port imaging, a serve challenge facing people is sample scattering. However, multiphoton imaging has good deep tissue penetration due to its longer wavelength. Moreover, due to its nonlinear optical properties, the multiphoton imaging has less phototoxicity and photobleaching. These advantages make it an optical non-invasive microscopic imaging of biological samples.

Thus, the MPM system can be regarded as a good choice for imaging living biological tissues on different scales. As a result, vast quantities of data and images are becoming available to further enhance the understanding of various aspects of complex biological interactions.

### **Experimental studies**

Protein liquid-liquid phase separation (LLPS) appeared within the cell is a biochemical phenomenon of organising clusters to affect cellular functions. For instance, ageing and neurodegenerative diseases are related to LLPS-driven processes (Alberti *et al.*, 2018; Li *et al.*, 2012). Thus, the observation of the dynamic of LLPS can help to understand cell biology. For observation

and analysis of LLPS, there are several methods which can be employed to determine whether the proteins undergo LLPS (such as microscopic detection of liquid droplets, assessing the turbidity of the solution, monitoring the fusion and fission of liquid droplets).

According to the characteristics of the MPM imaging system, THG originates from optical inhomogeneity and requires no specific symmetry, which can be used for locating LLPS samples. UV imaging of this system can detect proteins, which can detect protein LLPS droplets and mobility of LLPS. Consequently, the combination of THG and UV imaging methods of the MPM system may be a potential imaging tool applied to the detection and study of protein LLPS dynamics.

### **Medical diagnosis**

In principle, the MPM imaging system allows visualization of suspicious or abnormal tissues at cellular and subcellular levels, thereby reducing sampling error. There have been many previous studies using THG, SHG and UV to observe pathological tissues to help doctors diagnose diseases. Different published studies have already tested the MPM as a potential “optical biopsy” tool for real-time evaluation of diseases (Lee *et al.*, 2004).

For instance, SHG imaging can detect the changes in the structure or content of collagen in tissues, those in diseased tissues are different from those in normal tissues (Cicchi *et al.*, 2013). TPEF images can easily observe the morphology of single nuclei in the cell and thereby distinguish between normal cells and cancer cells (Jung *et al.*, 2004). Moreover, for unstained tissue samples, the TPEF/SHG microscope can scan the tissue with low invasiveness, and thus it is a good substitute for conventional imaging. Notably, THG imaging technology (provide detailed information about biochemical composition of the sample) can be also employed as a new tool for evaluating fibrotic diseases such as brain, kidney, heart, *etc.* (Lee *et al.*, 2004; Kuzmin *et al.*, 2016; Li *et al.*, 2016).

All in all, the discovery and development of biological sciences are inseparable from the development of imaging technology. Every major breakthrough in the

field of biological sciences is reliant on the development of imaging technologies. With the continuous development of optical imaging technology, peculiar phenomena in biological sciences have been continuously discovered and studied on this basis. Even though not every new imaging technology is perfect, every new imaging technology still has its own strengths. Hence, performing various sorts of measurements and improve optical imaging methods based on the measurement results are necessary.

## 6 References

- Alberti, S., Saha, S., Woodruff, J. B., Franzmann, T. M., Wang, J. *et al.* (2018). A user's guide for phase separation assays with purified proteins. *Journal of Molecular Biology*. **430**, 4806-4820, doi:10.1016/j.jmb.2018.06.038.
- Albota, M. A., Xu, C. & Webb, W. W. (1998). Two-photon fluorescence excitation cross sections of biomolecular probes from 690 to 960 nm. *Applied Optics*. **37**, 7352-7356, doi:10.1364/ao.37.007352.
- Allen, J. E., Sutherland, T. E. & Becker, L. (2019). Crystal-clear treatment for allergic disease. *Science* **364**, 738-739, doi: 10.1126/science. aax6175.
- Arndt, U. W. (2003). Personal X-ray reflections. *Methods in Enzymology*. **368**, 21-42, doi:10.1016/S0076-6879(03)68003-1.
- Arndt, U. W. (1990). Focusing optics for laboratory sources in X-ray crystallography. *Journal of Applied Crystallography*. **23**, 161–168, doi:10.1107/s0021889890000334.
- Atkin-Smith, G. K., Tixeira, R., Paone, S., Mathivanan, S., Collins, C. *et al.* (2015). A novel mechanism of generating extracellular vesicles during apoptosis via a beads-on-a-string membrane structure. *Nature Communications*. **6**, 7439, doi:10.1038/ncomms8439.
- Baitan, D., Schubert, R., Meyer, A., Dierks, K., Perbandt, M. *et al.* (2018). Growing protein crystals with distinct dimensions using automated crystallization coupled with in situ dynamic light scattering. *Journal of Visualized Experiments*. **138**, e57070, doi:10.3791/57070.
- Baldwin, E. T., Crumley, K. V. & Carter, C. W. (1986). Practical, rapid screening of protein crystallization conditions by dynamic light scattering. *Biophysical Journal*. **49**, 47–48, doi:10.1016/s0006-3495(86)83587-1.
- Banerjee, S., Nathan, P. C., François-Xavier, G., Nitish, S., Jandhyam, S. *et al.* (2016). Structure of a heterogeneous, glycosylated, lipid-bound, *in vivo*-grown protein crystal at atomic resolution from the viviparous cockroach *diploptera punctate*. *IUCRJ*. **3**, 282-293, doi:10.1107/S2052252516008903.

- Barad Y., Eisenberg, H., Horowitz, M. & Silberberg, Y. (1997). Nonlinear scanning laser microscopy by third harmonic generation. *Applied Physics Letters*. **70**, 922-924, doi:10.1063/1.118442.
- Basu, S., Kaminski, J. W., Panepucci, E., Huang, C. Y., Warshamanage, R. *et al.* (2019). Automated data collection and real-time data analysis suite for serial synchrotron crystallography. *Journal of Synchrotron Radiation*. **26**, 244-252, doi:10.1107/S1600577518016570.
- Batyuk, A., Galli, L., Ishchenko, A., Han, G. W., Gati, C. *et al.* (2016). Native phasing of X-ray free-electron laser data for a G protein-coupled receptor. *Science Advances*. **2**, e1600292, doi:10.1126/sciadv.1600292.
- Bayarjargal, L. (2008). Nonlinear optical properties of lithium sulfate monohydrate. *Crystal Research and Technology*. **43**, 1138-1142, doi:10.1002/crat.200800311.
- Benninger, R. K. P. & Piston, D. W. (2013). Two-photon excitation microscopy for the study of living cells and tissues. *Current Protocols in Cell Biology*. **59**, 4.11.1-4.11.24, doi:10.1002/0471143030.cb0411s59.
- Bittrich, S., Schroeder, M. & Labudde, D. (2018). Characterizing the relation of functional and early folding residues in protein structures using the example of aminoacyl-tRNA synthetases. *PLoS ONE* **13**, e0206369, doi:10.1371/journal.pone.0206369.
- Bloomfield, V. A. (1981). Quasi-elastic light scattering applications in biochemistry and biology. *Annual Review of Biophysics and Bioengineering*, **10**, 421–450, doi:10.1146/annurev.bb.10.060181.002225.
- Bogan, M. J., Boutet, S., Barty, A., Benner, W. H., Frank, M. *et al.* (2010). Single-shot femtosecond x-ray diffraction from randomly oriented ellipsoidal nanoparticles. *Physical Review Special Topics - Accelerators and Beams*. **13**, 094701, doi:10.1103/physrevstab.13.094701.
- Borland, M., Decker, G., Emery, L., Sajaev, V., Sun, Y. P. *et al.* (2014). Lattice design challenges for fourth-generation storage-ring light sources. *Journal of Synchrotron Radiation*. **21**, 912-936, doi:10.1107/s1600577514015203.

- Boudes, M., Garriga, D., Fryga, A., Caradoc-Davies, T. & Coulibaly, F. (2016). A pipeline for structure determination of *in vivo*-grown crystals using in cellulose diffraction. *Acta Crystallographica Section D - Biological Crystallography*. **72**, 576-585, doi:10.1107/S2059798316002369.
- Boutet, S., Lomb, L., Williams, Barends, T. R., Aquila, A. *et al.* (2012). High-resolution protein structure determination by serial femtosecond crystallography. *Science*. **337**, 362-364, doi:10.1126/science.1217737.
- Bragg, W. H. (1913). The reflection of X-rays by crystals (II). *Proceedings of the Royal Society A: Mathematical, Physical and Engineering Sciences*. **89**, 246–248, doi:10.1098/rspa.1913.0082.
- Bragg, W. H. & Bragg, W. L. (1913). The reflection of X-rays by crystals. *Proceedings of the Royal Society A: Mathematical, Physical and Engineering Sciences*. **88**, 428–438, doi:10.1098/rspa.1913.0040.
- Bragg, W. L. & Pippard, A. B. (1953). The form birefringence of macromolecules. *Acta Crystallographica*. **6**, 865–867, doi:10.1107/S0365110X53002519.
- Bragg, W. L. (1913). The structure of some crystals as indicated by their diffraction of X-rays. *Proceedings of the Royal Society A: Mathematical, Physical and Engineering Sciences*. **89**, 248–277, doi:10.1098/rspa.1913.0083.
- Brown, E., McKee, T., diTomaso, E., Pluen, A., Seed, B. *et al.* (2003). Dynamic imaging of collagen and its modulation in tumors *in vivo* using second-harmonic generation. *Nature Medicine*. **9**, 796-800, doi:10.1038/nm879.
- Campagnola, P. J. & Loew, L. M. (2003). Second-harmonic imaging microscopy for visualizing biomolecular arrays in cells, tissues and organisms. *Nature Biotechnology*. **21**, 1356-1360, doi:10.1038/nbt894.
- Campagnola, P. J., Wei, M., Lewis, A. & Loew, L. M. (1999). High-resolution nonlinear optical imaging of live cells by second harmonic generation. *Biophysical Journal*. **77**, 3341–3349, doi:10.1016/S0006-3495(99)77165-1.
- Cao, Q., Zhegalova, N. G., Wang, S. T., Akers, W. J. & Berezin, M. Y. (2013). Multispectral imaging in the extended near-infrared window based on

endogenous chromophores. *Journal of Biomedical Optics*. **18**, 101318, doi:10.1117/1.JBO.18.10.101318.

Chapman, H. N., Caleman, C. & Timneanu, N. (2014). Diffraction before destruction. *Philosophical Transactions of the Royal Society of London. Series B, Biological sciences*. **369**, 20130313, doi:10.1098/rstb.2013.0313.

Chapman, H. N., Fromme, P., Barty, A., Whita, T. A., Kirian, R. A. *et al.* (2011). Femtosecond X-ray protein nanocrystallography. *Nature*. **470**, 73-77, doi:10.1038/nature09750.

Chen, R. Q., Yin, D. C., Lu, Q. Q., Shi, j. Y. & Ma, X. L. (2012). Sensitivity of lysozyme crystallization to minute variations in concentration. *Acta Crystallographica Section D - Biological Crystallography*. **68**, 584-591, doi:10.1107/s0907444912006427.

Chen, S.-Y., Hsu, C.-Y. & Sun, C.-K. (2008). Epi-third and second harmonic generation microscopic imaging of abnormal enamel. *Optics Express*. **16**, 11670-11679, doi.org/10.1364/OE.16.011670.

Cheng, L. C., Horton, N. G., Wang, K., Chen, S. J. & Xu, C. (2014). Measurements of multiphoton action cross sections for multiphoton microscopy. *Biomedical Optics Express*. **5**, 3427–3433, doi:10.1364/BOE.5.003427.

Cheng, Q. D., Chen, R. Q., He, J., Li, D. W., Yang, F. *et al.* (2017). Effect of the weather conditions during solution preparation on lysozyme crystallization. *Journal of Applied Crystallography*. **50**, 1341-1351, doi:10.1107/s1600576717011086.

Cheng, R. K. Y. (2020). Towards an optimal sample delivery method for serial crystallography at XFEL. *Crystals*. **10**, 215, doi:10.3390/cryst10030215.

Chernov, A. A. (2003). Protein crystals and their growth. *Journal of Structural Biology*. **142**, 3–21, doi:10.1016/s1047-8477(03)00034-0.

Christopher G. K., Phipps A. G. & Gray R. J. (1998). Temperature-dependent solubility of selected proteins. *Journal of Crystal Growth*. **191**, 820–826, doi:10.1016/s0022-0248(98)00355-8.

- Chu, S. W., Tai, S. P., Sun, C. K. & Lin, C. H. (2007). Selective imaging in second-harmonic-generation microscopy by polarization manipulation. *Applied Physics Letters*. **91**, 103903, doi:10.1063/1.2783207.
- Chung, H. -Y., Liu, W., Cao, Q., Song, L., Kärtner, F. X. & Chang, G. Q. (2018). Megawatt peak power tunable femtosecond source based on self-phase modulation enabled spectral selection. *Optics Express*. **26**, 3684-3695, doi:10.1364/oe.26.003684.
- Chung, H.-Y., Greinert, R., Kärtner, F. X. & Chang, G. Q. (2019a). Multimodal imaging platform for optical virtual skin biopsy enabled by a fiber-based two-color ultrafast laser source. *Biomedical Optics Express*. **10**, 514-525, doi:10.1364/boe.10.000514.
- Chung, H.-Y., Liu, W., Cao, Q., Greinert, R., Kartner, F. X. *et al.* (2019b). Tunable, ultrafast fiber-laser between 1.15 and 1.35 $\mu$ m for harmonic generation microscopy in human Skin. *IEEE Journal of Selected Topics in Quantum Electronics*. **25**, 6800708, doi:10.1109/jstqe.2018.2864193.
- Cicchi, R., Vogler, N., Kapsokalyvas, D., Dietzek, B., Popp, J. *et al.* (2013). From molecular structure to tissue architecture: collagen organization probed by SHG microscopy. *Journal of Biophotonics*. **6**, 129-142, doi:10.1002/jbio.201200092.
- Closser, R. G., Gualtieri, E. J., Newman, J. A. & Simpson, G. J. (2013). Characterization of salt interferences in second-harmonic generation detection of protein crystals. *Journal of Applied Crystallography*. **46**, 1903-1906, doi:10.1107/s0021889813027581.
- Coleman, M. L., Sahai, E. A., Yeo, M., Bosch, M., Dewar, A. *et al.* (2001). Membrane blebbing during apoptosis results from caspase-mediated activation of ROCK I. *Nature Cell Biology*. **3** 339-345, doi:10.1038/35070009.
- Coolidge, U. S. Patent US1,203,495 (1913).
- Coulibaly, F. E., Chiu, E., Ikeda, K., Gutmann, S., Haebel, P. W. *et al.* (2007). The molecular organization of cypovirus polyhedra. *Nature*. **446**, 97-101, doi:10.1038/nature05628.

- Dähn, A., Hübner, W & Bennemann, K. H. (1996). Symmetry analysis of the nonlinear optical response: second harmonic generation at surfaces of antiferromagnets. *Physical Review Letters*. **77**, 3929-3932, doi:10.1103/physrevlett.77.3929.
- Debarre, D., Supatto, W., Pena, A. M., Fabre, A., Tordjmann, T. *et al.* (2006). Imaging lipid bodies in cells and tissues using third-harmonic generation microscopy. *Nature Methods*. **3**, 47-53, doi:10.1038/nmeth813.
- Denk, W., Strickler, J. H. & Webb, W. W. (1990). Two-photon laser scanning fluorescence microscopy. *Science*. **248**, 73-76, doi:10.1126/science.2321027.
- Determann, S., Lobbes, J. M., Reuter, R. & Rullkötter, J. (1998). Ultraviolet fluorescence excitation and emission spectroscopy of marine algae and bacteria. *Marine Chemistry*. **62**, 137-156, doi:10.1016/s0304-4203(98)00026-7.
- Devaud, G., Furcinitti, P. S., Fleming, J. C., Lyon, M. K. & Douglas, K. (1992). Direct observation of defect structure in protein crystals by atomic force and transmission electron microscopy. *Biophysical Journal*. **63**, 630-638, doi:10.1016/s0006-3495(92)81651-x.
- Dierks, K., Meyer, A., Einspahr, H., & Betzel, C. (2008). Dynamic light scattering in protein crystallization droplets: adaptations for analysis and optimization of crystallization processes. *Crystal Growth & Design*. **8**, 1628–1634, doi:10.1021/cg701067r.
- Dierks, K., Meyer, A., Oberthür, D., Rapp, G., Einspahr, H. *et al.* (2010). Efficient UV detection of protein crystals enabled by fluorescence excitation at wavelengths longer than 300 nm. *Acta Crystallographica Section F Structural Biology and Crystallization Communications*. **66**, 478-484, doi:10.1107/s1744309110007153.
- Doye, J. P. K. & Poon, W. C. K. (2006). Protein crystallization *in vivo*. *Current Opinion in Colloid & Interface Science*. **11**, 40-46, doi:10.1016/j.cocis.2005.10.002.
- Drobizhev, M., Makarov, N. S., Tillo, S. E., Hughes, T. E. & Rebane, A. (2011). Two-photon absorption properties of fluorescent proteins. *Nature Methods*. **8**, 393–399, doi:10.1038/nmeth.1596.

- Du, W., Li, L., Nichols, K. P. & Ismagilov, R. F. (2009). Slipchip. *Lab on a Chip*. **9**, 2286-2292, doi:10.1039/b908978k.
- Erny, C. & Hauri, C. P. (2013). Design of efficient single stage chirped pulse difference frequency generation at 7  $\mu\text{m}$  driven by a dual wavelength Ti:sapphire laser. *Applied Physics B*. **117**, 379–387, doi:10.1007/s00340-014-5846-6.
- Falke, S., Dierks, K., Blanchet, C., Graewert, M., Cipriani, F. *et al.* (2018). Multi-channel *in situ* dynamic light scattering instrumentation enhancing biological small-angle X-ray scattering experiments at the PETRA III beamline P12. *Journal of Synchrotron Radiation*. **25**, 361–372, doi:10.1107/s1600-577517017568.
- Fine, S. & Hansen, W. P. (1971). Optical second harmonic generation in biological systems. *Applied Optics*. **10**, 2350-2353, doi:10.1364/ao.10.002350.
- Fisher, T. J., Wang, M., Ibrahim, Y., Steffensmeier, B. & Cheung, C. L. (2016). Effect of sodium nitrate on microwave-assisted synthesis of ceria nanocubes. *Materials Letters* **178**, 71–74, doi:10.1016/j.matlet.2016.04.186.
- Franken, P. A., Hill, A. E., Peters, C. W. & Weinreich, G. (1961). Generation of Optical Harmonics. *Physical Review Letters*. **7**, 118-119, doi:10.1103/physrevlett.7.118.
- Fraundorf, P., Qin, W., Moeck, P. & Mandell, E. (2005). Making sense of nanocrystal lattice fringes. *Journal of Applied Physics*. **98**, 114308, doi:10.1063/1.2135414.
- Freund, I., Deutsch. M. & Sprecher. A. Connective tissue polarity. (1986). Optical second-harmonic microscopy, crossed-beam summation, and small-angle scattering in rat-tail tendon. *Biophysical Journal*. **50**, 693-712, doi:10.1016/S0006-3495(86)83510-X.
- Friedrich, W., Knipping, P. & von Laue, M. (1913). Interferenzerscheinungen bei Röntgenstrahlen. *Annalen Der Physik*. **346**, 971-988, doi:10.1002/andp.19133461004.

- Gannaway, J. N. & Sheppard, C. J. R. (1978). Second-harmonic imaging in the scanning optical microscope. *Optical and Quantum Electronics*. **10**, 435–439, doi:10.1007/bf00620308.
- Gill, H. S. (2010). Evaluating the efficacy of tryptophan fluorescence and absorbance as a selection tool for identifying protein crystals. *Acta Crystallographica Section F Structural Biology and Crystallization Communications*. **66**, 364-372, doi:10.1107/s1744309110002022.
- Green, D. W., Ingram, V. M. & Perutz, M. F. (1954). The structure of haemoglobin. IV. Sign determination by the isomorphous replacement method. *Proceedings of the Royal Society A: Mathematical, Physical and Engineering Sciences*. **225**, 287–307, doi:10.1098/rspa.1954.0203.
- Guesmi, K., Abdeladim, L., Tozer, S., Mahou, P., Kumamoto, T. *et al.* (2018). Dual-color deep-tissue three-photon microscopy with a multiband infrared laser. *Light: Science & Applications*. **7**, 12, doi:10.1038/s41377-018-0012-2.
- Guha, S., Perry, S. L., Pawate, A. S. & Kenis, P. J. A. (2012). Fabrication of X-ray compatible microfluidic platforms for protein crystallization. *Sensors and Actuators B: Chemical*. **174**, 1-9, doi:10.1016/j.snb.2012.08.048.
- Guo, W. S., Guo, F., Wei, C. S., Liu, Q., Zhou, G. *et al.* (2002). SHG from centrosymmetric supermolecular crystal. *Science in China Series B*. **45**, 267-274, doi:10.1360/02yb9035.
- Hauptert, L. M. & Simpson, G. J. (2011). Screening of protein crystallization trials by second order nonlinear optical imaging of chiral crystals (SONICC). *Methods*. **55**, 379-386, doi:10.1016/j.ymeth.2011.11.003.
- Hauptert, L. M., DeWalt, E. L. & Simpson, G. J. (2012). Modeling the SHG activities of diverse protein crystals. *Acta Crystallographica Section D Biological Crystallography*. **68**, 1513-1521, doi:10.1107/s0907444912037638.
- He, T. C., Zhou, S., da Costa, L. T., Kinzler, K. W. & Vogelstien, B. (1998). A simplified system for generating recombinant adenoviruses. *Proceedings of the National Academy of Sciences of the United States of America*. **95**, 2509-2514, doi:10.1073/pnas.95.5.2509.

- Hejtmancik, J. F. (2008). Congenital cataracts and their molecular genetics. *Seminars in Cell & Developmental Biology*. **19**, 134-139, doi:10.1016/j.semcdb.2007.10.003.
- Hell, S. W., Malak, H. M., Gryczynski, I., Lakowicz, J. R., Bahlmann, K. *et al.* (1996). Three-photon excitation in fluorescence microscopy. *Journal of Biomedical Optics* **1**, 71-74, doi:10.1117/12.229062.
- Helliwell, J. R. (2017). New developments in crystallography: exploring its technology, methods and scope in the molecular biosciences. *Bioscience Reports*. **37**, BSR20170204, doi:10.1042/BSR20170204.
- Holton, J. M. & Frankel, K. A. (2010). The minimum crystal size needed for a complete diffraction data set. *Acta Crystallographica Section D Biological Crystallography*. **66**, 393-408, doi:10.1107/s0907444910007262.
- Horton, N. G., Wang, K., Kobat, D., Clark, C. G., Wise, F. W. *et al.* (2013). *In vivo* three-photon microscopy of subcortical structures within an intact mouse brain. *Nature Photonics*. **7**, 205-209, doi:10.1038/nphoton.2012.336.
- Hunter, M. S., DePonte, D. P., Shapiro, D. A., Kirian, R. A., Wang, X. *et al.* (2011). X-ray diffraction from membrane protein nanocrystals. *Biophysical Journal*. **100**, 198-206, doi: 10.1016/j.bpj.2010.10.049.
- Imasaka, T., Tashiro, K. & Ishibashi, N. (1990). Analytical instrumentation based on optical harmonic generation. *Analytical Sciences*. **6**, 301-302, doi:10.2116/analsci.6.301.
- Judge, R. A., Swift, K. & González, C. (2005). An ultraviolet fluorescence-based method for identifying and distinguishing protein crystals. *Acta Crystallographica Section D Biological Crystallography*. **61**, 60-66, doi:10.1107/s0907444904026538.
- Jung, J. C., Mehta, A. D., Aksay, E., Stepanoski, R. & Schnitzer, M. J. (2004). *In vivo* mammalian brain imaging using one- and two-photon fluorescence microendoscopy. *Journal of Neurophysiology*. **92**, 3121-3133, doi:10.1152/jn.00234.2004.

Kadima, W., McPherson, A., Dunn, M. F. & Journak, F. A. (1990). Characterization of precrystallization aggregation of canavalin by dynamic light scattering. *Biophysical Journal*. **57**, 125-132, doi:10.1016/s0006-3495(90)82513-3.

Kendrew, J. C., Bodo, G., Dintzis, H. M., Prerrish, R. G. & Wyckoff, H. (1958). A three-dimensional model of the myoglobin molecule obtained by X-ray analysis. *Nature*. **181**, 662-666, doi:10.1038/181662a0.

Kissick, D. J., Wanapun, D. & Simpson, G. (2011). Second-Order Nonlinear Optical Imaging of Chiral Crystals. *Annual Review of Analytical Chemistry*. **4**, 419-437, doi:10.1146/annurev.anchem.111808.073722.

Koopmann, R., Cupelli, K., Redecke, L., Nass, K., DePonte, D. P. *et al.* (2012). *In vivo* protein crystallization opens new routes in structural biology. *Nature Methods*. **9**, 259-262, doi:10.1038/nmeth.1859.

Kou, L., Labrie, D. & and Chylek, P. (1993). Refractive indices of water and ice in the 0.65- to 25- $\mu\text{m}$  spectral range. *Applied Optics*. **32**, 3531–3540, doi:10.1364/ao.32.003531.

Kupitz, C., Grotjohann, I., Conrad, C. E., Roy-Chowdhury, S., Fromme, R. *et al.* (2014). Microcrystallization techniques for serial femtosecond crystallography using photosystem II from *Thermosynechococcus elongatus* as a model system. *Philosophical Transactions of the Royal Society B: Biological Sciences*. **369**, 20130316, doi:10.1098/rstb.2013.0316.

Kuzmin, N. V., Wesseling, P., deWitt Hamer, C., Noske, D. P., Galgano, G. D. *et al.* (2016). Third harmonic generation imaging for fast, label-free pathology of human brain tumors. *Biomedical Optics Express*. **7**, 1889–1904, doi:10.1364/boe.7.001889.

Kyrychenko, A. (2015). Using fluorescence for studies of biological membranes: a review. *Methods and Applications in Fluorescence*. **3**, 042003, doi:10.1088/2050-6120/3/4/042003.

Lakowicz, J. R. (2006). Principles of Fluorescence Spectroscopy. 3rd edition. *Springer, Boston, MA*. doi:10.1007/978-0-387-46312-4.

- Lee, H. S., Liu, Y., Chen, H. C., Chiou, L. L., Huang, G. T. *et al.* (2004). Optical biopsy of liver fibrosis by use of multiphoton microscopy. *Optics Letters*. **15**, 2614-2616, doi:10.1364/ol.29.002614.
- Levantino, M., Yorke, B. A., Monteiro, D. C. F., Cammarata, M. & Pearson, A. R. (2015). Using synchrotrons and XFEL for time-resolved X-ray crystallography and solution scattering experiments on biomolecules. *Current Opinion in Structural Biology*. **35**, 41-48, doi:10.1016/j.sbi.2015.07.017.
- Li, L. H. Chen, Z. F., Wang, X. F., Jiang, W. Z., Zhuo, S. M. *et al.* (2016). Visualization of tumor response to neoadjuvant therapy for rectal carcinoma by nonlinear optical imaging. *IEEE Journal of Selected Topics in Quantum Electronics*. **22**, 158-163, doi:10.1109/jstqe.2015.2456108.
- Li, L., Mustafi, D., Fu, Q., Tereshko, V. Chen, D. L. *et al.* (2006). Nanoliter microfluidic hybrid method for simultaneous screening and optimization validated with crystallization of membrane proteins. *Proceedings of the National Academy of Sciences*. **103**, 19243-19248, doi:10.1073/pnas.0607502103.
- Li, P., Banjadw, S., Cheng, H. -C., Kim, S., Chen, B. *et al.* (2012). Phase transitions in the assembly of multivalent signalling proteins. *Nature*. **483**, 336-340, doi:10.1038/nature10879.
- Lisinski, S., Ratke, L., Schaniel, D., Jungk, T., Soergel, E. *et al.* (2010). Second-harmonic generation in nano-structured LiTaO<sub>3</sub> and LiNbO<sub>3</sub> - xerogels with randomly oriented ferroelectric grains. *Optical Materials*. **32**, 504-509, doi:10.1016/j.optmat.2009.11.003.
- Liu, H. G. & Lee, W. (2019). The XFEL protein crystallography: developments and perspectives. *International Journal of Molecular Sciences*. **20**, 3421, doi:10.3390/ijms20143421.
- Liu, W., Chia, S. H., Chung, H. -Y., Greinert, R., Kärtner, F. X. *et al.* (2017). Energetic ultrafast fiber laser sources tunable in 1030–1215 nm for deep tissue multi-photon microscopy. *Optics Express*. **25**, 6822-6831, doi:10.1364/oe.25.006822.

- Liu, W., Li, C., Zhang, Z., Kärtner, F. X. & Chang, G. Q. (2016). Self-phase modulation enabled, wavelength-tunable ultrafast fiber laser sources: an energy scalable approach. *Optics Express*. **24**, 15328-15340, doi:10.1364/oe.24.015328.
- Liu, Y., Hou, H., Li, J., Cheng, Q. D., Zhang, X., Zeng, X. B. *et al.* (2020). Direct crystallization of proteins from impure sources. *Crystal Growth & Design*. **20**, 1694-1705, doi:10.1021/acs.cgd.9b01446.
- Lomelino, C. L., Kim, J. K., Lee, C., Lim, S. W., Andring, J. T. *et al.* (2018). Carbonic anhydrase II microcrystals suitable for XFEL studies. *Acta Crystallographica Section F Structural Biology Communications*. **74**, 327-330, doi:10.1107/s2053230x18006118.
- Lukina, M. M., Dudenkova, V. V., Shimolina, L. E., Snopova, L. B., Zagaynova, E. V. *et al.* (2019). *In vivo* metabolic and SHG imaging for monitoring of tumor response to chemotherapy. *Cytometry Part A*. **95A**, 47-55, doi:10.1002/cyto.a.23607.
- Lüpke, G., Bottomley, D. J. & Vandriel, H. M. (1994). Second- and third-harmonic generation from cubic centrosymmetric crystals with vicinal faces: phenomenological theory and experiment. *Journal of the Optical Society of America B*. **11**, 33-44, doi:10.1364/josab.11.000033.
- Madden, J. T., DeWalt, E. L. & Simpson, G. (2011). Two-photon excited UV fluorescence for protein crystal detection. *Acta Crystallographica Section D Biological Crystallography*. **67**, 839-846, doi:10.1107/s0907444911028253.
- Martin-Garcia, J. M., Zhu, L., Mendez, D., Lee, M., Chun, Y. E. *et al.* (2019). High-viscosity injector-based pink-beam serial crystallography of microcrystals at a synchrotron radiation source. *IUCrJ*. **6**, 412-425, doi:10.1107/S205225251900263X.
- Marx, V. (2014). Structural biology: 'seeing' crystals the XFEL way. *Nature Methods*. **11**, 903-908, doi:10.1038/nmeth.3070.

- Masters, B. R., So, P. T. C. & Gratton, E. (1997). Multiphoton excitation fluorescence microscopy and spectroscopy of *in vivo* human skin. *Biophysical Journal*. **72**, 2405-2412, doi:10.1016/s0006-3495(97)78886-6.
- McPherson, A. (2004). Introduction to protein crystallization. *Methods*. **34**, 254–265, doi:10.1016/j.ymeth.2004.03.019.
- McPherson, A. (1991). A brief history of protein crystal growth. *Journal of Crystal Growth*. **110**, 1-10, doi:10.1016/0022-0248(91)90859-4.
- Meents, A., Wiedorn, M. O., Srajer, V., Henning, R. Sarrou, I. *et al.* (2017). Pink-beam serial crystallography. *Nature Communications*. **8**, 1281, doi:10.1038/s41467-017-01417-3.
- Monteiro, D. C. F., Vakili, M., Harich, J., Sztucki, M., Meier, S. M. *et al.* (2019). A microfluidic flow-focusing device for low sample consumption serial synchrotron crystallography experiments in liquid flow. *Journal of Synchrotron Radiation*. **26**, 406-412, doi:10.1107/s1600577519000304.
- Monteiro, D. C. F., von Stetten, D., Stohrer, C., Sans, M., Pearson, A. R. *et al.* (2020). 3D-MiXD: 3D-printed X-ray compatible microfluidic devices for rapid, low-consumption serial synchrotron crystallography data collection in flow. *IUCrJ*. **7**, 207-219, doi:10.1107/S2052252519016865.
- Moraes, I., Evans, G., Sanchez-Weatherby, J., Newstead, S. & Stewart, P. D. (2014). Membrane protein structure determination - the next generation. *Biochimica et Biophysica Acta (BBA) - Biomembranes*. **1838**, 78-87, doi:10.1016/j.bbamem.2013.07.010.
- Moss, D. K., Betin, V. M., Malesinski, S. D. & Lane J. D. (2006). A novel role for microtubules in apoptotic chromatin dynamics and cellular fragmentation. *Journal of Cell Science*. **119**, 2362-2374, doi:10.1242/jcs.02959.
- Moulton, P. F. (1986). Spectroscopic and laser characteristics of Ti:Al<sub>2</sub>O<sub>3</sub>. *Journal of the Optical Society of America. B, Optical physics*. **3**, 125–133, doi:10.1364/josab.3.000125.
- Mueller-Dieckmann, C., Panjikar, S., Tucker, P. A. & Weiss, M. S. (2005). On the routine use of soft X-rays in macromolecular crystallography. Part III. The

- optimal data-collection wavelength. *Acta Crystallographica Section D Biological Crystallography*. **61**, 1263-1272, doi:10.1107/s0907444905021475.
- Müller, M., Squier, J., Wilson, K. R. & Brakenhoff. J. (1998). 3D-microscopy of transparent objects using third-harmonic generation. *Journal of Microscopy*. **191**, 266–274, doi:10.1046/j.1365-2818.1998.00399.x.
- Müntz, V. K. (1998). Deposition of storage proteins. *Plant Molecular Biology*. **38**, 77-99, doi.org/10.1023/A:1006020208380.
- Nalla, V., Medishetty, R., Wang, Y., Bai, Z., Sun, H. *et al.* (2015). Second harmonic generation from the 'centrosymmetric' crystals. *IUCrJ*. **2**, 317-321, doi:10.1107/s2052252515002183.
- Nannenga, B. L., Shi, D., Leslie, A. G. W. & Gonen, T. (2014). High-resolution structure determination by continuous-rotation data collection in MicroED. *Nature Methods*. **11**, 927–930, doi:10.1038/nmeth.3043.
- Neutze, R. (2014). Opportunities and challenges for time-resolved studies of protein structural dynamics at X-ray free-electron lasers. *Philosophical Transactions of the Royal Society B: Biological Sciences*. **369**, 20130318, doi:10.1098/rstb.2013.0318.
- Neutze, R., Wouts, R., van der Spoel, D., Weckert, E. & Hajdu, J. (2000). Potential for biomolecular imaging with femtosecond X-ray pulses. *Nature*. **406**, 752-757, doi:10.1038/35021099.
- Newman, J. A. & Simpson. G. J. (2016). Nonlinear optical characterization of membrane protein microcrystals and nanocrystals. *Advances in Experimental Medicine and Biology*. **922**, 91-103, doi:10.1007/978-3-319-35072-1\_7.
- Newman, J. A., Scarborough, N. M., Pogranichniy, N. R., Shrestha, R. K., Closser, R. G. *et al.* (2015). Intercalating dyes for enhanced contrast in second-harmonic generation imaging of protein crystals. *Acta Crystallographica Section D Biological Crystallography*. **71**, 1471-1477, doi:10.1107/S1399004715008287.
- Newman, J. A., Zhang, S. J., Sullivan, S. Z., Dow, X. Y., Becker, M. *et al.* (2016). Guiding synchrotron X-ray diffraction by multimodal video-rate protein

crystal imaging. *Journal of Synchrotron Radiation*. **23**, 959-965, doi:10.1107/s1600577516005919.

Norrman, M., Stahl, K., Schluckebier, G. & Al-Karadaghi, S. (2006). Characterization of insulin microcrystals using powder diffraction and multivariate data analysis. *Journal of Applied Crystallography*. **39**, 391-400, doi:10.1107/s0021889806011058.

Oberthür, D., Melero-García, E., Dierks, K., Meyer, A., Betzel, C. *et al.* (2012). Monitoring and Scoring Counter-Diffusion Protein crystallization experiments in capillaries by *in situ* dynamic light scattering. *PLoS One*, **7**, e33545. doi:10.1371/journal.pone.0033545.

Oberthür, D. (2018). Biological single-particle imaging using XFELs – towards the next resolution revolution. *IUCRJ*. **5**, 663-666, doi:10.1107/S2052252518015129.

Oldenbourg, R. & Ruiz, T. (1989). Birefringence of macromolecules. Wiener's theory revisited, with applications to DNA and tobacco mosaic virus. *Biophysical Journal*. **56**, 195-205, doi:10.1016/s0006-3495(89)82664-5.

Oron, D., Yelin, D., Tal, E., Raz, S., Fachima, R. & Silberberg, Y. (2004). Depth-resolved structural imaging by third-harmonic generation microscopy. *Journal of Structural Biology*. **147**, 3-11, doi:10.1016/s1047-8477(03)00125-4.

Orville, A. M. (2018). Entering an era of dynamic structural biology. *BMC Biology*. **16**, 55, doi:10.1186/s12915-018-0533-4.

Owen, R. L. & Garman, E. (2005). A new method for predetermining the diffraction quality of protein crystals: using SOAP as a selection tool. *Acta Crystallographica Section D Biological Crystallography*. **61**, 130–140, doi:10.1107/s0907444904029567.

Pande, A., Pande, J., Asherie, N., Lomakin, A., Ogun, O. *et al.* (2001). Crystal cataracts: Human genetic cataract caused by protein crystallization. *Proceedings of the National Academy of Sciences of the United States of America*. **98**, 6116-6120, doi:10.1073/pnas.101124798.

- Pandey, S., Bean, R., Sato, T., Poudyal, I., Bielecki, J. *et al.* (2019). Time-resolved serial femtosecond crystallography at the European XFEL. *Nature Methods*. **17**, 73-78, doi:10.1038/s41592-019-0628-z.
- Persson, E. K., Verstraete, K., Heyndrickx, I., Gevaert, E., Aegerter, H. *et al.* (2019). Protein crystallization promotes type 2 immunity and is reversible by antibody treatment. *Science*. **364**, eaaw4295, doi:10.1126/science.aaw4295.
- Perutz, M. F., Rossmann, M. G., Cullis, A. F., Muirhead, H., Will, G. & North, A. C. T. (1960). Structure of haemoglobin. A three-dimensional Fourier synthesis at 5.5Å resolution obtained by x-ray analysis. *Nature*. **185**, 416–422, doi:10.1038/185416a0.
- Petzold, U., Buchel, A. & Halfmann, T. (2012). Effects of laser polarization and interface orientation in harmonic generation microscopy. *Optics Express*. **20**, 3654-3662, doi:10.1364/OE.20.003654.
- Poon, I. K., Chiu, Y. H., Armstrong, A. J., Kinchen, J. M. & Juncadella, I. J. *et al.* (2014). Unexpected link between an antibiotic, pannexin channels and apoptosis. *Nature*. **7**, 329-334, doi:10.1038/nature13147.
- Redecke, L., Nass, K., DePonte, D. P., White, T. A., Rehders, D. *et al.* (2013). Natively inhibited Trypanosoma brucei cathepsin B structure determined by using an X-ray laser. *Science*. **339**, 227-230, doi:10.1126/science.1229663.
- Rehberg, M., Krombach, F., Pohl, U. & Dietzel, S. (2011). Label-free 3D visualization of cellular and tissue structures in intact muscle with second and third harmonic generation microscopy. *PLoS one*. **6**, e28237, doi:10.1371/journal.pone.0028237.
- Röntgen, W. K. (1896). A new form of radiation. *Science*. **3**, 726-729, doi:10.1126/science.3.72.726.
- Rowe, E. M & Mills, F. E. (1973). Tantalus I: A dedicated storage ring synchrotron radiation source. *Particle Accelerators*. **4**, 211-227.
- Rowlands, C. J., Park, D., Bruns, O. T., Piatkevich, K. D., Fukumura, D. *et al.* (2017). Wide-field three-photon excitation in biological samples. *Light: Science & Applications*. **6**, e16255, doi:10.1038/lsa.2016.255.

- Schmidt, M. (2019). Time-resolved macromolecular crystallography at pulsed X-ray sources. *International Journal of Molecular Sciences*. **20**, 1401, doi:10.3390/ijms20061401.
- Schotte, F., Lim, M., Jackson, T. A., Smirnov, A. V., Soman, J. *et al.* (2003). Watching a protein as it functions with 150-ps time-resolved X-ray crystallography. *Science*. **300**, 1944-1947, doi:10.1126/science.1078797.
- Schubert, R., Meyer, Arne., Dierks, K., Kapis, S., Reimer, R. *et al.* (2015). Reliably distinguishing protein nanocrystals from amorphous precipitate by means of depolarized dynamic light scattering. *Journal of Applied Crystallography*. **48**, 1476-1484, doi:10.1107/s1600576715014740.
- Sebbagh, M., Renvoizé, C., Hamelin, J., Riché, N., Bertoglio, J. *et al.* (2001). Caspase-3-mediated cleavage of ROCK I induces MLC phosphorylation and apoptotic membrane blebbing. *Nature Cell Biology*. **3**, 346-352, doi:10.1038/35070019.
- Shi, D., Nannenga, B. L., Iadanza, M. G. & Gonen, T. (2013). Three-dimensional electron crystallography of protein microcrystals. *eLife*. **2**, e01345, doi:10.7554/eLife.01345.
- Shim, J. U., Cristobal, G., Link, D. R., Thorsen, T. & Fraden, S. (2007). Using microfluidics to decouple nucleation and growth of protein crystals. *Crystal Growth Design*. **7**, 2192-2194, doi:10.1021/cg700688f.
- Smith, J. L., Fischetti, R. F. & Yamamoto, M. (2012). Micro-crystallography comes of age. *Current Opinion in Structural Biology*. **22**, 602-612, doi:10.1016/j.sbi.2012.09.001.
- Smyth, M. S. & Martin, J. H. J. (2000). X-ray crystallography. *Molecular Pathology*. **53**, 8–14, doi: 10.1136/mp.53.1.8.
- Spence, J. C. H. & Chapman, H. N. (2014). The birth of a new field. *Philosophical Transactions of the Royal Society B: Biological Sciences*. **369**, 20130309, doi:10.1098/rstb.2013.0309.
- Spence, J. C. H. (2017). XFELs for structure and dynamics in biology. *IUCRJ*. **4**, 322-339, doi:10.1107/S2052252517005760.

- Spence, J. C. H., Weierstall, U. & Chapman, H. N. (2012). X-ray lasers for structure and dynamics biology. *Reports on Progress in Physics*. **75**, 102601, doi:10.1088/0034-4885/75/10/102601.
- Spiliopoulou, M., Valmas, A., Triandafillidis, D. -P., Kosinas, C., Fitch, A. *et al.* (2020). Applications of X-ray powder diffraction in protein crystallography and drug screening. *Crystals*. **10**, 54, doi:10.3390/cryst10020054.
- Stagno, J. R. Liu, Y., Bhandari, Y. R., Conrad, C. E., Panja, S. *et al.* (2017). Structures of riboswitch RNA reaction states by mix-and-inject XFEL serial crystallography. *Nature*. **541**, 242-246, doi:10.1038/nature20599.
- Stahl, K., Frankaer, C. G., Petersen, J. & Harris, P. (2013). Monitoring protein precipitates by in-house X-ray powder diffraction. *Powder Diffraction*. **28**, 458-469, doi:10.1017/s0885715613000833.
- Stetefeld, J., McKenna, S. A. & Patel, T. R. (2016). Dynamic light scattering: a practical guide and applications in biomedical sciences. *Biophysical Reviews*. **8**, 409-427, doi:10.1007/s12551-016-0218-6.
- Stevenson, H. P., DePonte, D. P., Makhov, A. M., Conway, J. F., Zeldin, O. B. *et al.* (2014a). Transmission electron microscopy as a tool for nanocrystal characterization pre- and post-injector. *Philosophical Transactions of the Royal Society B: Biological Sciences*. **369**, 20130322, doi:10.1098/rstb.2013.0322.
- Stevenson, H. P., Makhov, A. M., Calero, M., Edwards, A. L., Zeldin, O. B. *et al.* (2014b). Use of transmission electron microscopy to identify nanocrystals of challenging protein targets. *Proceedings of the National Academy of Sciences of the United States of America*. **111**, 8470–8475, doi:10.1073/pnas.1400240111.
- Su, J. Y. (2018). A brief history of charcot-leyden crystal protein/galectin-10 Research. *Molecules*. **23**, 2931, doi:10.3390/molecules23112931.
- Su, X. D., Zhang, H., Terwilliger, T. C., Liljas, A., Xiao, J. *et al.* (2015). Protein crystallography from the perspective of technology developments. *Crystallography Reviews*. **21**, 122–153, doi:10.1080/0889311x.2014.973868

- Sui, S. & Perry, S. L. (2017). Microfluidics: From crystallization to serial time-resolved crystallography. *Structural Dynamics*. **4**, 032202, doi:10.1063/1.4979640.
- Sun, C.-K. (2005). Higher harmonic generation microscopy. *Advances in Biochemical Engineering/Biotechnology*. **95**, 17-56, doi:10.1007/b102209.
- Tavella, F., Stojanovic, N., Geloni, G. & Gensch, M. (2011). Few-femtosecond timing at fourth-generation X-ray light sources. *Nature Photonics*. **5**, 162-165, doi:10.1038/nphoton.2010.311.
- Tixeira, R., Caruso, S., Paone, S., Baxter, A. A., Atkin-Smith, G. K, *et al.* (2017). Defining the morphologic features and products of cell disassembly during apoptosis. *Apoptosis*. **22**, 475-477, doi:10.1007/s10495-017-1345-7.
- Tolstikova, A., Levantino, M., Yefanov, O., Hennicke, V., Fischer, P. *et al.* (2019). 1 kHz fixed-target serial crystallography using a multi-layer monochromator and an integrating pixel detector. *IUCrJ*. **6**, 927-937, doi:10.1107/S205225251900914X.
- Toraya, H. J. (2016). A new method for quantitative phase analysis using X-ray powder diffraction: direct derivation of weight fractions from observed integrated intensities and chemical compositions of individual phases. *Journal of Applied Crystallography*. **49**, 1508-1516, doi:10.1107/s16005767 16010451.
- Tsang, T. Y. F. (1995). Optical third-harmonic generation at interfaces. *Physical Review A*. **52**, 4116-4125, doi:10.1103/physreva.52.4116.
- Van Steenberghe, V., Boesmans, W., Li, Z., de Coene, Y., Vints, K. *et al.* (2019). Molecular understanding of label-free second harmonic imaging of microtubules. *Nature Communications*. **10**, 3530, doi:10.1038/s41467-019-11463-8.
- Vekilov, P. G. (2010). The two-step mechanism of nucleation of crystals in solution. *Nanoscale*. **2**, 2346-2357, doi:10.1039/c0nr00628a.
- Vernede, X., Lavault, B., Ohana, J., Nurizzo, D., Joly, J. *et al.* (2006). UV laser-excited fluorescence as a tool for the visualization of protein crystals mounted in loops. *Acta Crystallographica Section D Biological Crystallography*. **62**, 253-261, doi: 10.1107/S0907444905041429.

- Wampler, R. D., Kissick, D. J., Dehen, C. J., Gualtieri, E. J., Grey, J. L. *et al.* (2008). Selective detection of protein crystals by second harmonic microscopy. *Journal of the American Chemical Society*. **130**, 14076-14077, doi:10.1021/ja805983b.
- Wang, S. S., Chen, X. X., Huang, B., Su, Y. J., Zhang, W. X. *et al.* (2018). Bromocholine bromide is a molecular ferroelectric with moderate phase transition temperature. *Journal of Materials Chemistry C*. **6**, 2221-2224, doi:10.1039/c8tc00419f.
- Watts, D., Müller-Dieckmann, J., Tsakanova, G., Lamzin, V. S. & Groves, M. R. (2010). Quantitative evaluation of macromolecular crystallization experiments using 1,8-ANS fluorescence. *Acta Crystallographica Section D Biological Crystallography*. **66**, 901–908, doi:10.1107/s0907444910020664.
- Weigelin, B., Bakker, G. -J. & Friedl, P. (2012). Intravital third harmonic generation microscopy of collective melanoma cell invasion. *IntraVital*. **1**, 32-43, doi:10.4161/intv.21223.
- Wiedorn, M. O., Oberthur, D., Bean, R., Schubert, R., Werner, N. *et al.* (2018). Megahertz serial crystallography. *Nature Communications*. **9**, 4025, doi: 10.1038/s41467-018-06156-7.
- Wilkosz, P. A., Chandrasekhar, K. & Rosenberg, J. M. (1995). Preliminary characterization of EcoRI-DNA co-crystals: incomplete factorial design of oligonucleotide sequences. *Acta Crystallographica Section D - Biological Crystallography*. **51**, 938-945, doi: 10.1107/S0907444994005251.
- Xiao, Q., Lin, W., Chen, G. X., Ding, C. J., Dong, G. P. *et al.* (2015). Morphology and polarization-dependent second harmonic generation in single hexagonal sodium niobate micro/nano-crystals. *Journal of Materials Chemistry C*. **3**, 4070-4076, doi:10.1039/c5tc00226e.
- Yamamoto, M., Hirata, K., Yamashita, K., Hasegawa, K., Ueno, G. *et al.* (2017). Protein microcrystallography using synchrotron radiation. *IUCRJ*. **4**, 529-539, doi: 10.1107/S2052252517008193.

Yorke, B. A., Beddard, G. S., Owen, R. L. & Pearson, A. R. (2014). Time-resolved crystallography using the Hadamard transform. *Nature Methods*. **11**, 1131-1134, doi: 10.1038/nmeth.3139.

Zhao, F. Z., Zhang, B., Yan, E. K., Sun, B. B., Wang, Z. J. *et al.* (2019). A guide to sample delivery systems for serial crystallography. *The FEBS Journal*. **286**, 4402-4417, doi: 10.1111/febs.15099.

Zhou, W., Yin, K., Wang, C., Zhang, Y., Xu, T. *et al.* (2015). The observation of square ice in graphene questioned. *Nature*. **528**, E1–E2, doi:10.1038/nature16145.

Ziegler, U. & Groscurth, P. (2004). Morphological features of cell death. *News in physiological sciences: an international journal of physiology produced jointly by the International Union of Physiological Sciences and the American Physiological Society*. **19**, 124-128, doi:10.1152/nips.01519.2004.



## Appendix

### List of chemicals

Chemical (listed alphabetically)	Supplier	Hazard Statements	Precautionary Statements
Acetic acid	Chem-solute	H226, H314	P280, P305+351+338, P310
NH <sub>4</sub> Cl	Sigma Aldrich	H302	P270, P301+312, P330, P501
(NH <sub>4</sub> ) <sub>2</sub> SO <sub>4</sub>	Carl Roth	-	-
Bis-tris methane	Sigma Aldrich	-	-
CsCl	Carl Roth	H361fd	P280, P308+P313
CaCl <sub>2</sub>	Sigma Aldrich	H319	P305+351+338
Ca(CH <sub>3</sub> COO) <sub>2</sub>	Sigma Aldrich	H315, H319, H335	P261, P305+351+338
Dulbecco's modified eagle medium (DMEM)	Sigma Aldrich	-	-
DMSO	Sigma Aldrich	-	-
EDTA	Sigma Aldrich	H319	P305+351+338
Fetal bovine serum (FBS)	Sigma Aldrich	-	-
HEPES	Sigma Aldrich	-	-
KCl	Carl Roth	-	-
Li <sub>2</sub> SO <sub>4</sub>	Applichem	H302	-
MgCl <sub>2</sub>	Carl Roth	-	-
Na(CH <sub>3</sub> COO) <sub>2</sub>	Applichem	-	-
NaCl	Carl Roth	-	-
NaH <sub>2</sub> PO <sub>4</sub>	Applichem	-	-

Na <sub>2</sub> HPO <sub>4</sub>	Applichem	-	-
NaOH	Sigma Aldrich	H314	P280, P310, P305+351+338
NaKcitrate	Sigma Aldrich	-	-
Na <sub>3</sub> citrate	Sigma Aldrich	-	-
NaNO <sub>3</sub>	Sigma Aldrich	H272, H315, H319, H335, H373	P220, P221, P260, P264, P280, P302+352, P305+351+338, P312, P332+313, P337+313, P362, P370+378, P403+233, P405, P501
Na <sub>2</sub> SO <sub>4</sub>	Sigma Aldrich	-	-
Photophate- buffered saline	Sigma Aldrich	H319	P280, P264, P305+351+338, P337+313
PDMS	Dow corning	H413	-
PEG 3350	Sigma Aldrich	-	-
PEG 8000	Sigma Aldrich	-	-
Polyethyleneimine	Sigma Aldrich	H411	P273, P501, P391
Paraformaldehyde	Sigma Aldrich	H228, H302+H332, H315, H317, H318, H335, H341, H350	P202, P210, P270, P280, P305+351+338, P308+313
Penicillin- Streptomycin	Sigma Aldrich	H302, H317, H361fd	P302+352, P308+313
Serum-free medium (EX Cell® 420)	Sigma Aldrich	-	-
Tris	Fluka	H315, H319, H335	P261, P305+351+338

## GHS Hazard Statements

---

<b>H226</b>	Flammable liquid and vapor
<b>H228</b>	Flammable solid
<b>H272</b>	May intensify fire; oxidizer
<b>H302</b>	Harmful if swallowed
<b>H311</b>	Toxic in contact with skin
<b>H314</b>	Causes severe skin burns and eye damage
<b>H315</b>	Causes skin irritation
<b>H317</b>	May cause an allergic skin reaction
<b>H318</b>	Causes serious eye damage
<b>H319</b>	Causes serious eye irritation
<b>H332</b>	Harmful if inhaled
<b>H335</b>	May cause respiratory irritation
<b>H341</b>	Suspected of causing genetic defects
<b>H350</b>	May cause cancer
<b>H361</b>	Suspected of damaging fertility or the unborn child
<b>H361d</b>	Suspected of damaging the unborn child
<b>H361f</b>	Suspected of damaging fertility

---

---

**H373** May cause damage to organs through prolonged or repeated exposure

**H411** Toxic to aquatic life with long lasting effects

---

## GHS Precautionary Statements

---

<b>P210</b>	Keep away from heat/sparks/open flames/hot surfaces – No smoking
<b>P260</b>	Do not breathe dust/fume/gas/mist/vapors/spray
<b>P261</b>	Avoid breathing dust/fume/gas/mist/vapors/spray
<b>P264</b>	Wash thoroughly after handling
<b>P270</b>	Do not eat, drink or smoke when using this product
<b>P273</b>	Avoid release to the environment
<b>P280</b>	Wear protective gloves/protective clothing/eye protection/face protection
<b>P310</b>	Immediately call a poison center or doctor/physician
<b>P312</b>	Call a poison center or doctor/physician if you feel unwell
<b>P330</b>	Rinse mouth
<b>P362</b>	Take off contaminated clothing and wash before reuse P391 Collect spillage
<b>P405</b>	Store locked up
<b>P501</b>	Dispose of contents/container in accordance with local/regional/national/international regulations

---

---

<b>P301+312</b>	If swallowed: call a poison center or doctor/physician if you feel unwell
<b>P302+352</b>	IF ON SKIN: Wash with soap and water
<b>P305+351+338</b>	If in eyes: rinse cautiously with water for several minutes. Remove contact lenses if present and easy to do - continue rinsing
<b>P308+313</b>	If exposed or concerned: Get medical advice/attention
<b>P332+313</b>	If skin irritation occurs: Get medical advice/attention
<b>P337+313</b>	If eye irritation persists: Get medical advice/attention
<b>P370+378</b>	In case of fire: Use for extinction: Alcohol resistant foam
<b>P403+233</b>	Store in a well-ventilated place. Keep container tightly closed

---

## List of figures

Fig. 1-1 Schematic representation of Bragg's law conditions. ....	11
Fig. 1-2 Early history of protein crystallography.....	12
Fig. 1-3 The process of single-crystal X-ray diffraction. ....	14
Fig. 1-4 The process of synchrotron radiation single-crystal X-ray diffraction. .....	16
Fig. 1-5 Schematic of XFEL crystallography and crystallography experimental set-up.....	18
Fig. 1-6 Schematic representation of sample delivery methods for serial synchrotron and femtosecond crystallography.....	19
Fig. 1-7 Examples of various protein crystals detection applying the conventional optical microscopy. ....	21
Fig. 1-8 Unstained protein crystals and stained protein crystals. ....	22
Fig. 1-9 Schematic diagram of TEM system. ....	23
Fig. 1-10 Schematic graph of DLS and DLS instruments.....	25
Fig. 1-11 Schematic and photographic presentation of DDLS set-up.	26
Fig. 1-12 Schematic representation of X-ray powder diffraction. ....	27
Fig. 1-13 Multiphoton fluorescence diagram .....	29
Fig. 1-14 Absorption and emission spectra of tryptophan, tyrosine, phenylalanine.....	30
Fig. 1-15 Schematic set-up of UV instrument applied to protein crystal detection experiment. ....	31
Fig. 1-16 Energy band diagram of second-harmonic generation. ....	32
Fig. 1-17 Energy band diagram of third-harmonic generation.....	33
Fig. 1-18 Strategy of combining UV and SHG image methods.....	35

Fig. 1-19 External and internal views of the Formulatrix SONICC. ....	36
Fig. 1-20 Schematic representation of SONICC imaging.....	37
Fig. 1- 21 Flow chart of the experimental work carried out in this thesis. .....	40
Fig. 2-1 Sample preparation applying the LCP sandwich plate. ....	51
Fig. 2-2 Schematic of the PDMS chip fabrication. ....	52
Fig. 2-3 PDMS microfluidic chip preparation.....	54
Fig. 2-4 Schematic of the PDMS microfluidic chip .....	55
Fig. 2-5 Sample preparation in the PDMS microfluidic chip.....	56
Fig. 2-6 Sample preparation in the MRC-2 crystallization plate. ....	57
Fig. 3-1 Detection workflow using the multiphoton imaging system. ..	62
Fig. 3-2 Optical wavelength coverage of common ultrafast lasers. ....	65
Fig. 3-3 Scheme of the MPM system (laser part and scanning microscope). ....	66
Fig. 3-4 Photographic image of the MPM instrument. ....	67
Fig. 3-5 SESS source with peak power at 1300 nm. ....	68
Fig. 3-6 Simulation result of a 290-fs pulse propagating in an optical fiber. .....	69
Fig. 3-7 Simulation of frequency-doubling.....	70
Fig. 3-8 THG signal selection by setting DM (dichroic mirror) and BPF (bandpass filter) under 1300 nm excitation. ....	71
Fig. 3-9 SHG/UV fluorescence signal selection by setting DM2 and BPFs under 775 nm excitation.....	72
Fig. 3-10 Protein crystallization results under some conditions. ....	73

Fig. 3-11 SHG and THG detection images from a LCP sandwich plate. .....	75
Fig. 3-12 SHG and THG detection images from an MRC-2 crystallization plate. ....	76
Fig. 3-13 Bright-field and THG imaging of labelled numbers located on a PDMS microfluidic chip. ....	77
Fig. 3-14 SHG and THG detection images from a PDMS microfluidic chip.....	78
Fig. 3-15 Polarization-dependent SHG signal intensities of images taken from glucose isomerase crystals. ....	79
Fig. 3-16 Polarization-dependent SHG signal intensities of images taken from thaumatin crystals. ....	80
Fig. 3-17 SHG images of salt crystals captured by the in-house MPM instrument. ....	82
Fig. 3-18 MPM imaging system detection for thaumatin crystals and sodium tartrate crystal.....	84
Fig. 3-19 Total free energy versus cluster size. ....	86
Fig. 4-1 Particle radius distribution, DLS and DDLS signal intensities of three protein crystallization experiments.....	92
Fig. 4-2 TEM imaging of nano- or micro-sized lysozyme crystals.....	94
Fig. 4-3 TEM imaging of nano- or micro-sized thaumatin crystals.....	95
Fig. 4-4 TEM imaging of nano- or micro-sized proteinase K crystals .	96
Fig. 4-5 Determination of lattice spacing values (three protein crystals) through analyzing fast Fourier transform (FFT) images.....	97
Fig. 4-6 X-ray powder diffraction rings for lysozyme, thaumatin, and proteinase K powder .....	98

Fig. 4-7 Lysozyme crystals in the PDMS microfluidic chip. ....	99
Fig. 4-8 Images of different protein crystals. ....	101
Fig. 4-9 Images recorded for different protein crystals applying the MPM system. ....	102
Fig. 4-10 Images of <i>in vivo</i> protein crystals. ....	103
Fig. 4-11 <i>In vivo</i> crystals of PAK4. ....	104
Fig. 4-12 Images of <i>in vivo</i> protein crystals selected for the imaging experiments .....	104
Fig. 4-13 Images of <i>in vivo</i> protein crystals for the imaging experiments .....	105
Fig. 4-14 Images of <i>in vivo</i> crystals of PAK4-inca (insect cells) .....	106
Fig. 4-15 Images of <i>in vivo</i> crystals of PAK4-inca (mammalian cells) .....	107
Fig. 4-16 Detection process for protein crystal applying the MPM system and the SONICC system. ....	111
Fig. 4-17 Parameters of the laser pulse. ....	113
Fig. 4-18 Absorption spectra of major biological tissues. ....	115

## List of tables

Table 2-1 List of proteins used for crystallization.....	41
Table 2-2 List of chemicals and reagents used in this work.....	42
Table 2-3 Overview of consumables. ....	44
Table 2-4 List of instruments used in this work.....	44
Table 2-5 Batch crystallization conditions of all investigated proteins with space groups of the resulting crystals. ....	46
Table 3-1 Comparison of different imaging methods.....	63
Table 3-2 Optical parameters for different nonlinear optical imaging modalities.....	64
Table 3-3 Specification for sample containers and imaging conditions. .....	74
Table 3-4 Information of salt crystals. ....	83
Table 4-1 Parameters of the SONICC and the MPM system.....	115
Table 4-2 Differences between <i>in vitro</i> and <i>in vivo</i> protein crystal....	118



# Acknowledgement

I would like to thank my supervisor Prof. Christian Betzel for giving me the opportunity to work in his group at Deutsches Elektronen-Synchrotron (DESY) and pursue PhD at the University of Hamburg. Prof. Christian Betzel provided me with abundant resources and much freedom; thus I could concentrate on my project. The results presented in this thesis schedule could not be achieved without his full support. In this work, to enrich the *in vivo* bioimaging studies, he introduced the *in vivo* protein crystals detection experiment. Also, I would like to thank my second supervisor PD. Perbandt Markus for his scientific support in our group. During the past four years, I was fortunate to work with many outstanding colleagues in the group and learn from them. In our group, Dr. Robin Schubert taught me protein nanocrystals preparation and fabrication of Polydimethylsiloxan (PDMS) microfluidic chips, Dr. Nadine Werner, and Dr. Célestin Nzanu Mudogo provided me with the lactamase crystals and *in vivo* protein crystal samples.

The MPM construction and application are very complementary and interdisciplinary between our collaborators and us. Therefore, I would like to especially thank Prof. Franz X. Kärtner and Prof. Guoqing Chang in Center for Free-Electron Laser Science (CEFL). They support my project by providing useful information and advice for MPM system construction and my manuscript. In addition, I would like to thank Dr. Hsiang-Yu Chung and Dr. Shih-Hsuan Chia. They built the MPM imaging system and conduct testing experiments with me. I learned a lot of knowledge of bio-imaging while working with them.

Besides, I would like to thank Dr. Sven Falke and Najeeb Ullah to review my manuscript and thesis; thank Dr. Michael Heymann for making and designing silicon wafer and thank Dr. Astrid Sydow for preparing *in vivo* protein crystals.

Finally, I would like to thank my parents and my friends for supporting my decision to pursue PhD in Germany.

This work would not have been possible without the financial support of the China Scholarship Council and Doctorate Scholarship from the University of Hamburg.

## **Eidesstattliche Versicherung:**

Hiermit versichere ich an Eides statt, die vorliegende Dissertation selbst verfasst und keine anderen als die ange- gebenen Hilfsmittel benutzt zu haben. Die eingereichte schriftliche Fassung entspricht der auf dem elektronischen Speichermedium. Ich versichere, dass diese Dissertation nicht in einem früheren Promotionsverfahren eingereicht wurde.

Hamburg 2021. 05. 26

Unterschrift